A METHOD OF ANALYSIS FOR THREE-DIMENSIONAL VISCOUS FLOW IN CENTRIFUGAL IMPELLERS

By

FRANK WARREN LINCOLN

A DISSERTATION PRESENTED TO THE GRADUATE COUNCIL OF
THE UNIVERSITY OF FLORIDA
IN PARTIAL FULFILLMENT OF THE REQUIREMENTS FOR THE
DEGREE OF DOCTOR OF PHILOSOPHY

UNIVERSITY OF FLORIDA

1975

ACKNOWLEDGEMENTS

The author wishes to extend his thanks to the members of his supervisory committee: Dr. R.B. Gaither, Dr. C.C. Oliver, Dr. R.A. Gater, Dr. J.F. Mahoney, and Dr. C.K. Hsieh. Special appreciation is due his major advisor, Dr. V.P. Roan, for his valuable assistance and encouragement.

Also, the financial support of the Mechanical Engineering Department, in the form of a graduate assistantship, is gratefully acknowledged.

Finally, the author would like to express his thanks to Ann for her patience and understanding throughout this research program.

TABLE OF CONTENTS

	Page
ACKNOWLEDGEMENTS	ii
NOMENCLATURE	vi
ABSTRACT	x
CHAPTERS:	
I INTRODUCTION	1
II REVIEW OF THE LITERATURE	5
Inviscid Flow Analyses	5
Three-Dimensional Boundary Layers	9
Experimental Investigations	14
Closing Remarks	21
III INVISCID FLOW ANALYSIS	22
Governing Equations	22
Boundary Conditions	26
Coordinate System and Geometry	30
Method of Analysis	35
Problem Formulation	37
Numerical Solution	52
Closing Remarks	72
IV BOUNDARY LAYER ANALYSIS	74
Governing Equations	75
Streamline Coordinates	78
Inviscid Flow Relations	83

Page

Hub and Shroud Boundary Layers 85
Momentum Integral Equations 87
Crossflow Relations 93
Streamwise Formulation 98
Crosswise Formulation 100
Calculation Procedure 102
Blade Surface Boundary Layers 107
Simplifying Assumptions 109
Momentum Integral Formulation 112
Corner Flow 117
Wake Flow 121
Curvature and Rotation Effects on Turbulence 123
Calculation Procedure 125

V COMBINED FLOW ANALYSIS 132
Introduction 132
Upstream Flow 134
Laminar Boundary Layer Calculation 134
Inlet Region 137
Initial Conditions 138
Impeller Discharge Matching Condition 139
Flow in the Vaneless Diffuser 142
Viscous/Inviscid Flow Interaction 148
Inviscid Flow Input for Boundary Layer Analysis 148
Corrections for Boundary Layer Displacement Thickness 150
Convergence Problems 154
Matching of Inviscid and Boundary Layer Velocity Profiles 155
Overall Calculation Procedure 161

VI RESULTS AND DISCUSSION

Inviscid Flow Calculations 164

Page

Comparison with Measured Data 171
Rotating Rectangular Diffuser 171
Radial-Flow Impeller with Swept-Back Blades 175
Analysis of a Radial-Bladed Centrifugal Pump Impeller 181

VII CONCLUSIONS 192

APPENDICES

A. CUBIC SPLINE CURVES 194

B. THE MOSES METHOD FOR TWO-DIMENSIONAL TURBULENT BOUNDARY LAYERS 198

C. GEODESIC CURVATURES FOR A SURFACE OF REVOLUTION 201

BIBLIOGRAPHY 208

BIOGRAPHICAL SKETCH 215

NOMENCLATURE

A	cross-sectional area, skin friction parameter
b	blade height or diffuser depth
C_f	skin friction coefficient
C_p	ratio of specific heats
$\hat{e}$	unit vector
H	total enthalpy or head, shape factor
H_R	relative total enthalpy
h	enthalpy, static head
h_1, h_2, h_3	metric coefficients
I	integral parameter defined by equation (4.37)
K_{ij}	geodesic curvature
k	coefficient in equation (4.61)
ℓ	distance, mixing length
m	meridional distance
$\dot{m}$	mass flow rate
n	normal distance, distance from hub in meridional plane, index for power-law profile
P	total pressure
P_R	relative total pressure
p	pressure
p^*	reduced static pressure
R_c	radius of curvature
Re	Reynolds number

R_i	Richardson number
R_m	meridional radius of curvature
R_δ	Reynolds number based on boundary layer thickness
r	radius normal to axis of rotation
r*	radius at which wake disappears in diffuser
s	distance measured along streamline, entropy
T	temperature
t	time, thickness
u,v,w,	relative velocity components in (x_1,x_2,x_3) directions
U	velocity at boundary layer edge
U_t	impeller tip speed
V	absolute velocity
W	relative velocity
x_1,x_2,x_3	orthogonal curvilinear coordinates
y	direction normal to surface
z	direction parallel to axis of rotation
Z	number of blades

Greek Letters

α	meridional flow angle
β	relative flow angle
γ	ratio of specific heats, diffuser angular momentum ratio, direction cosine
δ	boundary layer thickness
δ^*	boundary layer displacement thickness
ε	tangent of limiting wall streamline angle

η	dimensionless distance from wall, y/δ
Θ	boundary layer momentum thickness
θ	circumferential angle
κ	ratio of boundary layer thickness to displacement thickness, δ/δ^*
λ	swirl parameter, pressure gradient parameter
μ	viscosity, impeller work input coefficient
ν	kinematic viscosity
ξ	dimensionless diffuser radius
π	ratio of circumference to diameter for a circle
ρ	density
σ	ratio of wake thickness to passage width
τ	shear stress
ϕ	slope of conic surface in meridional plane
ψ	relaxation factor
Ω	vorticity
ω	rotational speed

Subscripts

0	condition at wall, stagnation condition
1	streamwise direction
2	direction normal to streamlines and tangent to surface
3	direction normal to surface
b	condition at blade surface
e	condition at impeller exit
h	hub

i	condition at impeller inlet
m	meridional direction
n	normal direction
ps	pressure surface
r	radial direction
s	shroud
ss	suction surface
t	conditions at impeller tip
z	axial direction
θ	circumferential direction

Superscripts

$\bar{}$	average
$\hat{}$	mass averaged

Abstract of Dissertation Presented to the Graduate Council of the University of Florida in Partial Fulfillment of the Requirements for the Degree of Doctor of Philosophy

A METHOD OF ANALYSIS FOR THREE-DIMENSIONAL VISCOUS FLOW IN CENTRIFUGAL IMPELLERS

By

Frank Warren Lincoln

Chairman: R.B. Gaither
Co-Chairman: V.P. Roan
Major Department: Mechanical Engineering

An analytical model is developed for steady, incompressible flow in shrouded centrifugal impellers of arbitrary design. The method is based on the assumption of an inviscid core flow with surrounding boundary layers on the passage walls.

The core flow calculation, which is applicable to incompressible or subsonic compressible flow, employs a streamline curvature technique to solve the governing equations on two intersecting families of stream surfaces. By employing several hub-to-shroud and blade-to-blade stream surfaces whose coordinates are determined as part of the solution, a truly three-dimensional analysis is achieved.

An orthogonal streamline coordinate system is used in the solution of boundary layer momentum integral equations which include the effects of rotation and streamline

curvature. Simple models for the boundary layer crossflow velocity profiles and the secondary flow in the corner regions permit a step-by-step calculation of the boundary layers on the hub, shroud and blade surfaces.

Finally, the inviscid and viscous flow analyses are combined, and the computed boundary layer displacement thickness is used to modify the passage geometry. Since the individual calculation schemes are strongly coupled, several iterations are required to achieve satisfactory convergence.

Reasonable agreement is obtained when predicted boundary layer development and discharge velocity profiles are compared with measurements in a rotating rectangular diffuser and a radial-flow impeller. Sample inviscid and viscous flow calculations are also presented for several other impeller configurations.

CHAPTER I

INTRODUCTION

Centrifugal or radial flow compressors have received considerable interest in recent years. Because of their high power-to-weight ratio, small gas turbines employing single stage centrifugals are preferred over those using multistage axial compressors for applications such as helicopters, light aircraft, and ground vehicles. However, the efficiency levels of centrifugal turbomachines are well below those of axial machines. This is a result, not only of the comparative lack of development effort, but also of the greater complexity of the flow in centrifugal impellers.

A single stage centrifugal compressor or pump consists of four basic elements:

1 An inlet section or duct designed to provide a uniform flow at the impeller inlet.

2 The impeller, in which energy is transferred to the fluid by increasing its angular momentum through turning of the relative flow, and also by increasing its radius of rotation. The primarily axial portion of an impeller, where most of the flow turning occurs, is called an inducer.

3 A radial diffuser which converts part of the kinetic energy leaving the impeller into static pressure rise.

4 An outlet section or collector located downstream of the diffuser.

The centrifugal impeller, which is our principal concern here, has three essential components: the hub, the shroud, and the blading. The hub and shroud contours are surfaces of revolution designed to efficiently turn the flow from an axial direction at the inlet to a radial direction at the discharge. When the shroud (outer surface) is attached to the blading, it is called a shrouded impeller. The blade shapes are dictated by a compromise between aerodynamic, stress, and manufacturing requirements.

Methods in use today for the design and analysis of centrifugal impellers are inadequate in all respects, and are usually based on two-dimensional flow solutions. Attempts to include viscous effects have been limited to simple geometries, or have used boundary layer techniques suitable only for planar flows.

The real flow in a centrifugal impeller is known to be highly three-dimensional with strong secondary flows, thick boundary layers, and regions of separation. Secondary flow arises within the impeller boundary layers as a result of Coriolis and centrifugal forces which induce pressure gradients normal to the mainstream direction.

These secondary flows can lead to significant redistribution of low energy fluid within the impeller passages, and thus have an important effect on the impeller discharge flow.

Clearly, what is needed is a prediction method which takes into account the three-dimensional nature of both the mainstream flow and the boundary layer flow. The development of such a method is the objective of this work.

The analysis described herein is applicable to shrouded centrifugal impellers having a constant width vaneless diffuser, and a uniform, irrotational upstream flow. It is assumed that the impeller flow comprises a boundary layer region surrounding a frictionless core flow. The core flow is calculated using a three-dimensional streamline curvature technique which requires no assumptions regarding stream surface shape or flow direction, and is applicable to incompressible or subsonic compressible flow. An orthogonal streamline coordinate system is employed in the solution of the boundary layer momentum equations which include terms resulting from rotation and curvature. Finally, the viscous and inviscid flow calculations are coupled in an iterative manner to determine the complete impeller flow field.

Chapter II provides a brief review of the recent literature relating to centrifugal impellers and three-dimensional boundary layers.

In Chapter III, a procedure is developed for analyzing the three-dimensional inviscid flow in an impeller without any restrictions on the stream surface shapes.

Chapter IV presents a three-dimensional turbulent boundary layer analysis for the impeller passage flow which includes the important effects of rotation and curvature.

In Chapter V, the analyses developed for the inviscid flow and the boundary layer flow are combined to provide an iterative solution technique for the complete passage flow.

Chapter VI shows some results obtained using the inviscid and viscous flow models and also presents a comparison of predicted and measured flows for a rotating diffuser and a radial-flow impeller.

Finally, some conclusions are given in Chapter VII.

CHAPTER II

REVIEW OF THE LITERATURE

This chapter presents a survey of the currently available technical literature relevant to the flow in centrifugal impellers. First, a brief account is given of several of the inviscid flow analysis methods presently in use. Second, the literature pertaining to the calculation of three-dimensional turbulent boundary layers is summarized with emphasis on momentum integral techniques. Finally, some of the recent experimental studies concerning flow in rotating passages and in centrifugal impellers are discussed.

Inviscid Flow Analyses

The pioneering work in the area of three-dimensional inviscid flow analysis was done by Wu [1] in the early 1950's.† He developed a general theory for steady compressible flow through an arbitrary turbomachine, and proposed a calculation method which involved satisfying the equations of motion on two intersecting families of stream surfaces known

†Reference [1] provides a good review of earlier literature on inviscid flow analysis methods for turbomachinery.

as the first kind (S1 or blade-to-blade) and the second kind (S2 or hub-to-shroud). Wu postulated that a complete three-dimensional solution could be obtained using a finite difference technique and iterating between the flows on the two families of stream surfaces, but this still has not been done.

As an alternative to the fully three-dimensional flow analysis envisioned in reference [1], several two-dimensional methods were developed for obtaining approximate solutions in either a hub-to-shroud or a blade-to-blade plane. One such method for analyzing flow in the hub-to-shroud or meridional plane was derived by Hamrick et al. [2] at NACA, and was based on a streamline curvature formulation with the assumption of axial symmetry. The streamline curvature approach, which is described by Smith [3] and Novak [4], involves first expressing the equations of motion in terms of the slope and curvature of the streamlines in the meridional plane, and then using an iterative procedure to adjust the streamlines and their meridional normals so that the equations governing conservation of mass, momentum, and energy are satisfied simultaneously. This method was applied to incompressible flow through centrifugal pump impellers in references [5] and [6], and in [5] it was shown that the assumption of axial symmetry is not needed if the flow is determined for a known S2 stream surface between the blades. A major

improvement to the basic streamline curvature approach was conceived by Katsanis [7], who employed fixed straight lines in the meridional plane in place of the streamline normals. Recently, this improved method has been used to analyze the meridional flow in centrifugal compressors [8].

An alternate means of solving the same governing equations on a hub-to-shroud S2 stream is known as matrix through-flow. This approach was developed by Marsh [9], and represents the first successful computational scheme derived from the theory of reference [1]. In both the streamline curvature and matrix through-flow methods, a two-dimensional solution is obtained on a mean S2 stream surface midway between the blades. The shape of this surface is assumed parallel to the mean blade shape except near the inlet and exit where empirical corrections are required. To provide a better approximation to the flow near the impeller inlet and discharge and along the blade surfaces, a parallel effort was pursued to establish procedures for flow in the blade-to-blade plane.

Either the finite difference stream function technique, or the streamline curvature analysis can be employed to predict the two-dimensional flow on a blade-to-blade surface of revolution, e.g., Kramer [10] and Katsanis [11]. However, these methods rely upon an estimate of the normal distance between two closely spaced stream surfaces through

which a specified mass flow passes. This spacing is determined by flow variations in the hub-to-shroud direction which must be obtained from a meridional plane solution.

A combination of two different two-dimensional solutions (a blade-to-blade solution and a meridional solution) results in what is termed a quasi-three-dimensional solution. Reference [12] suggests several possible combinations of current NASA two-dimensional flow analysis methods, and also presents a comparison of the blade surface velocities predicted by the various techniques. The large discrepancies between the predicted velocities (see Fig. 6.1 in Chapter VI) are attributed to the uncertainty of analyzing a highly three-dimensional flow with two-dimensional methods. A similar approach is reported by Senoo and Nakase [13], who employ a streamline curvature analysis much the same as that given in reference [7] in the meridional plane, and an improved (faster) solution technique [14] for the stream function equation on a blade-to-blade surface of revolution.

The principal deficiency in all of the above techniques is the failure to account for the true three-dimensional nature of the flow by requiring the S1 stream surfaces to be axisymmetric and the S2 surfaces to follow the mean blade shape. In a centrifugal impeller the stream surfaces may twist considerably as a result of work addition and blade blockage. Consequently, it is impossible to

properly satisfy conservation of mass since the true coordinates of the stream surface are not known.

Three-Dimensional Turbulent Boundary Layers

The prediction methods under development or in use today for three-dimensional turbulent boundary layer flows fall into two classes: (1) differential methods which apply finite difference approximations to solve the governing partial differential equations, and (2) momentum integral techniques employing analytical representations of the boundary layer velocity profiles. The differential methods clearly offer greater accuracy and more detailed information about the flow, while the integral schemes are generally less complicated and not as time consuming.

Reasonably successful differential analyses have been developed by Nash [15] and Bradshaw [16]. Both methods use an empirically modified turbulence kinetic energy equation for each of the turbulent shear stress components in addition to the continuity and time-average momentum equations. Nash employed a simple explicit finite difference procedure to integrate the governing equations, and Bradshaw solved a set of hyperbolic differential equations by the method of characteristics. Neither approach has been tested in a flow situation anywhere near as complex as in the passages of a centrifugal impeller.

Solution of the momentum integral equations for three-dimensional flow is considerably more difficult than for two-dimensional flow because of the additional variables involved. Also, because the velocity vector within a three-dimensional boundary layer is skewed (i.e., its direction varies with distance from the wall), it is necessary to specify velocity profile relations for two directions instead of one (e.g., streamwise and crosswise).

The survey paper by Cooke and Hall [17] gives the three-dimensional boundary layer equations in their general form, and discusses several existing momentum integral techniques for both laminar and turbulent flow. This treatment is restricted to stationary coordinate systems where the boundary layer crossflow (flow normal to the local free-stream direction) is the result of a turning mainstream flow.

The influence of coordinate rotation was dealt with by Mager [18], who derived momentum integral equations applicable to incompressible flow over a rotating surface. He also presented a solution for turbulent flow through a stationary curved duct which compared favorably with experiment. His method was based on a crosswise velocity profile model originally suggested by Prandtl, a power-law profile for the streamwise direction, and a small crossflow assumption which allowed all derivatives in the

crosswise direction to be neglected. As a result of these simplifications, the boundary layer momentum integral equations reduced to a pair of ordinary differential equations governing the streamwise development of momentum thickness (θ_{11}) and the tangent of the boundary layer deflection angle (ε), i.e., the tangent of the angle between the resultant wall shear stress direction and the local freestream flow direction.

Cumpsty and Head [19] applied the integral approach to the turbulent flow past an infinite swept wing. Their formulation included all the important terms in the streamwise and crosswise momentum equations, and was not restricted to small crossflow. Using Mager's crossflow model and an empirical entrainment equation for the streamwise shape factor, they were able to solve for the streamwise boundary layer development and the crossflow parameter ε by successive approximation. It should be noted, however, that although the boundary layer in this case is indeed three-dimensional, the fact that the flow does not vary in the spanwise direction allows one to eliminate derivatives in the crosswise direction and thus simplify matters considerably.

Cham and Head [20] used essentially the same solution technique as given in reference [19] for flow past a rotating body of revolution. The major contribution here lies in using a coordinate system on body geometry to

formulate the problem and then transforming to another more convenient system for solution of the equations. However, this approach is not of any advantage when the flow is asymmetric as in the case of flow through an impeller.

Boundary layers occurring in axial flow compressors and current methods of predicting them are discussed by Horlock [21]. The annulus wall (hub and casing) boundary layers, which are highly three-dimensional because of the turning mainstream, are analyzed by treating the flow as axisymmetric and simulating the blade effects by introducing distributed body forces into the governing equations. Horlock also points out that the profile or blade surface boundary layers in axial machines may be considered as almost two-dimensional unless separation occurs.

Dring [22] developed a momentum integral analysis for the annulus wall boundary layer in an axial turbine. His solution was based on Mager's [18] equations for constant shape factor (H) without the rotation terms. By considering the freestream flow to be irrotational, he was able to formulate the problem in an intrinsic coordinate system with stream function and potential function as independent variables. This led to a pair of coupled partial differential equations for θ_{11} and ε which he forced to be parabolic by an appropriate choice of the crosswise velocity profile, and then solved by the method of characteristics.

The boundary layer development on a rotating helical blade (representing the inducer section of a centrifugal impeller) contained in an annulus has been studied by Lakshminarayana et al. [23]. Measurements indicated earlier transition to turbulence and increased wall shear stress compared to stationary flat plate flow. Also, they observed much higher ε values in the laminar boundary layer region than in the turbulent region.

As mentioned earlier, the use of an integral method requires an auxiliary equation to relate the crosswise velocity components to the other parameters of the flow. In addition to the Prandtl-Mager model originally used in reference [18], several others have been proposed. One of the best known is the triangular profile due to Johnston [24]. This model provides a relation between the crosswise and streamwise velocity components in terms of the boundary layer deflection angle and an additional parameter related to the mainstream turning angle. Johnston also obtained fairly good correlation of the model with data from his own experiment and from other three-dimensional flows.

More general crossflow models have been suggested, but their use in a momentum integral scheme inevitably introduces new unknown parameters into the problem. For example, Shanebrook and Hatch [25] proposed a family of crossflow profiles based on a polynomial representation of the

crosswise velocity component as a function of the streamwise profile. One of the major objectives of this work was to provide a model capable of handling cross-over of s-shaped profiles encountered when the transverse pressure gradient is suddenly reversed, a situation which is unlikely in a centrifugal impeller passage.

Experimental Investigations

Most of the centrifugal pump and compressor performance data gathered in the past are of an overall nature, i.e., based on time-averaged and circumferentially averaged measurements taken at fixed locations downstream of the impeller. This type of information obscures the true three-dimensional character of the flow leaving the impeller, and therefore cannot be used to judge prediction methods concerned with the details of the flow. However, such data are often employed to evaluate and improve the various correlations proposed for estimating the slip factor (a measure of the average deviation of the relative flow from the blade direction at the impeller discharge). For example, Stahler [26] and Wiesner [27] compared predictions based on several well-known empirical and theoretical relations for slip factor with experimental values. The methods recommended for use as design tools showed reasonable agreement with the data ($\pm$ a few percent).

Dean [28] has criticized the indiscriminate use of slip factor correlations having no sound theoretical basis. He points out that the important fluid dynamic variable is the deviation of the flow (1-slip factor), and that when the data of reference [27] are plotted in terms of this parameter there is a scatter of as much as $\pm$ 50%.

An extensive investigation of the internal flow characteristics of centrifugal compressors was conducted by the NACA in the early 1950's [29]. As part of this research, actual flow measurements were obtained inside a 48-inch-diameter radial-inlet impeller by Hamrick *et al.* [30]. Recently, however, Dean [28] has reported that his own calculations indicate that these data do not satisfy continuity.

Similar studies were carried out by Acosta and Bowerman [31] for centrifugal pump impellers having both two-dimensional and three-dimensional configurations. The data obtained from these investigations and from the NACA impeller showed a region of low efficiency or high losses near the suction surface at the impeller discharge. This phenomenon was also observed by Ash [32] who measured the internal flow field of a mixed flow† impeller, and by Fujie [33, 34, 35] in his investigation of various centrifugal impeller designs.

---

†A mixed flow impeller discharges the flow at a meridional angle which is less than 90 degrees to the axis of rotation.

Lohmann [36] tested several radial flow impellers with varying blade loading characteristics in order to determine whether suction surface separation or secondary flow was the major factor responsible for the accumulation of low energy fluid adjacent to the suction surface. Measurements of the impeller discharge velocity profile with a hot-wire anemometer showed that secondary flows within the boundary layers along the hub and shroud surfaces transporting low velocity fluid to the suction side of the passage were the principal factor. This conclusion was later substantiated by Senoo et al. [37], who employed flow visualization techniques to observe the secondary flows in a centrifugal compressor impeller.

Recently, Lennemann [38] (see also reference [39]) obtained complete measurements of the relative velocity field in a radial-flow impeller using an elaborate hot-film technique. The impeller was fully shrouded and had swept-back circular arc blades of constant height. A large region of low velocity fluid was observed adjacent to the suction surface near the exit. This was attributed primarily to the action of secondary flows within the hub and shroud boundary layers.

In another report (Lennemann and Howard [40]), a hydrogen bubble flow visualization technique was used to study unsteady flow phenomena in both shrouded and

unshrouded centrifugal impellers. The results indicated that unsteady relative flow and unequal flow conditions in adjacent passages are primarily a boundary layer separation problem which occurs only at low flow rates well below the design point.

Further work based on the data reported in reference [38], but concentrating on the impeller discharge flow, is described by McDonald et al. [41]. They employed an analytical technique similar to the method of reference [11] to predict the blade-to-blade flow distribution for the same radial impeller used by Lennemann and Howard [38, 39, 40]. Comparison of the inviscid flow predictions with experimental data for relative velocities and flow direction showed a marked discrepancy, particularly near the impeller exit.

Attempts to include viscous effects in centrifugal impeller analyses are usually limited to the use of two-dimensional boundary layer calculation methods with no correction for the effects of Coriolis and centrifugal accelerators. Senoo et al. [42] have taken this approach, but by using three separate empirical correction factors to account for rotational and three-dimensional effects, they were able to achieve satisfactory agreement between measured and predicted slip factors for six different three-dimensional impeller designs. The experimental measurements associated with this work indicated two important characteristics

of the passage boundary layers: (1) the pressure surface boundary layers in all the impellers were less than 1/10 as thick as the suction surface boundary layers at the discharge, and (2) the ratio of actual suction surface boundary layer thickness at the impeller exit to the thickness computed using the two-dimensional method (Truckenbrodt) was inversely proportional to aspect ratio, i.e., (blade height)/(passage width). These results provide further evidence of the strong influence of secondary flow on the blade surface boundary layers.

The effects of rotation on the turbulent boundary layers in ducts of simple geometry have been studied by several investigators as a means of understanding the flow in the more complex passages of a centrifugal compressor. Considerable work in this area has been carried out at the M.I.T. Gas Turbine Laboratory since 1961. Experimental studies are reported in references [43], [44], and [45] where velocity profiles and wall shear stress were measured at mid-height along the pressure and suction surfaces of constant cross-section rectangular channels. These investigations showed that wall shear stress increased on the pressure side of the channel and decreased on the suction side as compared to the nonrotating values. Furthermore, as a result of secondary flows, large accumulations of low energy fluid were observed adjacent to the suction surface, particularly for the low aspect ratio ducts.

As a continuation of the rotating duct studies, Moore [46, 47, 48] measured the pressure and suction surface boundary layer development in a rotating rectangular diffuser closely resembling a passage of a radial-flow impeller. Data were obtained using a hot-wire probe for three different flows and one rotational speed. At the low flow rate, backflow was observed near the pressure surface, and at the larger flow rates a large wake region was detected adjacent to the suction surface. The measurements indicated significant crosswise velocity components in the direction of rotation within the end wall (hub and shroud) boundary layers, but the detailed structure of these layers and the associated crossflow profiles were not measured. (Detailed measurements of the end-wall boundary layer crossflow velocity distribution in a rotating rectangular duct are presented in reference [49]). In addition, the flow in the wake region was without backflow, and there appeared to be very little mixing between the wake and the freestream flow as discovered earlier by Dean [28].

Moore also developed a flow model for the rotating diffuser based on an approximate relation for the inviscid flow, and a modified two-dimensional momentum integral method for the boundary layers. Using a simple theory for the secondary flow through the corner regions, he was able to compute the core flow and boundary layers simultaneously.

The predicted results for the two larger flows compared favorably with the measured data for pressure and suction surface boundary layer development,† and thus provide some encouragement for the development of viscous flow models applicable to the complex passage geometries found in real centrifugal impellers.

Since Moore's results were for a single channel discharging to the stationary atmosphere, flow conditions near the exit were quite different from those in an actual impeller with adjacent flow passages. Fowler [50] investigated the flow in rotating two-dimensional channels of varying area, and used auxiliary side passages to simulate exit conditions. He found that the influence of adjacent channels, and downstream conditions in general, were very important. Particularly strong effects were noted regarding the flow along the suction surface and the blade-to-blade exit velocity profile.

The effects of rotation and surface curvature on turbulence structure or stability have been studied by several investigators. Litvai [51] has measured the velocity profiles on both curved and straight blades in a rotating impeller 5 meters in diameter. His preliminary results indicate that the modified velocity profiles

---

†According to reference [48], the best agreement was obtained when only 25% of the calculated crossflow was used.

resulting from these effects can be described with two additional empirical parameters which depend on local flow conditions.

Johnston [52, 53], who discusses rotation effects, and Bradshaw [54], who treats surface curvature effects, suggest simple correlations for mixing length based on the gradient Richardson number (ratio of nonconservative body forces to inertia forces). Both authors stress the importance of including rotation and curvature effects in turbulent boundary layer predictions.

Closing Remarks

Two important conclusions can be drawn from the work summarized in this chapter. Firstly, it is apparent that further attempts to correlate the complicated flow phenomena occurring in centrifugal pumps and compressors (e.g., slip factors) are impractical because of the large number of variables. Secondly, although we have achieved a fair qualitative understanding of the impeller flow through experiment, there is no method available which can predict the actual flow in a real centrifugal impeller. The objective of the present work is to develop such a method.

CHAPTER III

INVISCID FLOW ANALYSIS

In this chapter, a procedure is developed for analyzing three-dimensional inviscid flow in shrouded centrifugal impellers of arbitrary design. The method, which is applicable to either incompressible or subsonic compressible flow, is based on a minimum of simplifying assumptions, and is directed at impellers having an axial inlet and a radial discharge followed by a vaneless diffuser.

The approach followed involves application of the streamline curvature technique to solving the governing equations along two intersecting families of stream surfaces. By employing several hub-to-shroud and blade-to-blade stream surfaces whose coordinates are determined as part of the solution, a truly three-dimensional analysis is achieved. Furthermore, flow conditions at the impeller exit, the most critical area with respect to performance prediction, are calculated directly without resorting to empirical correction factors.

Governing Equations

The impeller flow is analyzed relative to a coordinate system which rotates at constant angular velocity

about the impeller axis. Use of a rotating reference frame is necessary if the flow is to be treated as steady, since the action of a finite number of blades produces a nonsteady as well as discontinuous absolute flow within the impeller passages, even when the absolute flow upstream of the impeller is steady. An equally important consequence of this transformation is that the resultant relative flow is rotational regardless of whether or not vorticity is present in the upstream flow field.

The equation of motion for frictionless flow relative to an impeller rotating with angular velocity $\vec{\omega}$ is

$$\frac{D\vec{W}}{Dt} + 2\vec{\omega} \times \vec{W} + \vec{\omega} \times (\vec{\omega}\times\vec{r}) = -\frac{\nabla p}{\rho} \qquad (3.1)$$

where $\frac{D(\ )}{Dt}$ is the substantial derivative (derivative following the motion of a fluid particle) which equals $\vec{W}\cdot\nabla(\ )$ for steady flow. This equation may be derived from the inviscid equation of motion for an absolute (stationary) reference frame by substituting the following vector relation between the absolute and relative velocities in a rotating coordinate system [55]:

$$\vec{V} = \vec{W} + \vec{\omega} \times \vec{r} \qquad (3.2)$$

Note that two important terms are present in equation (3.1) because of coordinate rotation: the Coriolis acceleration

$(2\vec{\omega} \times \vec{W})$ which exists wherever the relative velocity vector is not parallel to the axis of rotation, and the centrifugal acceleration $(\vec{\omega} \times (\vec{\omega} \times \vec{r}))$ which depends only upon radial distance from the axis.

A cylindrical coordinate system is employed in the present analysis to take advantage of the axisymmetric geometry of centrifugal impellers, i.e., the hub and shroud which are surfaces of revolution. Three component equations are obtained by forming the scalar product of equation (3.1) with the unit vectors in the r, θ, and z directions

$$\frac{DW_r}{Dt} - 2\omega W_\theta - \omega^2 r - \frac{W_\theta^2}{r} = -\frac{1}{\rho}\frac{\partial p}{\partial r}$$

$$\frac{DW_\theta}{Dt} + 2\omega W_r + \frac{W_r W_\theta}{r} = -\frac{1}{\rho r}\frac{\partial p}{\partial \theta} \qquad (3.3)$$

$$\frac{DW_z}{Dt} = -\frac{1}{\rho}\frac{\partial p}{\partial z}$$

The equation of mass conservation is of the same form when written with respect to either a rotating or stationary coordinate system. Therefore, for steady relative flow we may write

$$\nabla \cdot (\rho \vec{W}) = 0 \; . \qquad (3.4)$$

In addition to the conservation equations for mass and momentum, the energy equation is required in order to determine the work done on the fluid and the increase in its energy level as it passes through the impeller. A simple, yet very useful form of the energy equation may be derived by considering conditions along the relative path of a fluid particle. First, expressing the centrifugal acceleration as the gradient of a scalar potential, and using the vector identity $(\vec{W}\cdot\vec{\nabla})\vec{W} = \nabla(W^2/2) - \vec{W} \times (\nabla \times \vec{W})$ to replace $\frac{D\vec{W}}{Dt}$ in equation (3.1), we have

$$\nabla\left(\frac{W^2}{2} - \frac{\omega^2 r^2}{2}\right) + \frac{\nabla p}{\rho} = \vec{W} \times (\nabla \times \vec{W}) - 2\vec{\omega} \times \vec{W} \qquad (3.5)$$

Then defining the relative total enthalpy as

$$H_R \equiv h + \frac{W^2}{2} - \frac{\omega^2 r^2}{2} \qquad (3.6)$$

and forming the scalar product of equation (3.5) with the relative velocity, we obtain

$$\frac{DH_R}{Dt} = \vec{W} \cdot [\vec{W} \times (\nabla \times \vec{W} + 2\vec{\omega})] + T\frac{Ds}{Dt} \qquad (3.7)$$

where the Gibbs equation $\left(\frac{TDs}{Dt} = \frac{Dh}{Dt} - \frac{1}{\rho}\frac{Dp}{Dt}\right)$ has been used to eliminate pressure. Since the bracketed term in equation

(3.7) is orthogonal to $\vec{W}$, the scalar product vanishes, and we find that the relative total enthalpy is invariant along a streamline for steady relative motion if the entropy is constant, or

$$\frac{DH_R}{Dt} = \frac{D}{Dt}\left(h + \frac{W^2}{2} - \frac{\omega^2 r^2}{2}\right) = 0 . \tag{3.8}$$

This result is valid even for flows with friction, since the dissipative term that would appear in equation (3.7) cancels with the entropy term for an adiabatic flow. For incompressible flows, where internal energy changes are usually neglected, a quantity called the relative total pressure P_R is constant along a streamline when the flow is inviscid and steady, or

$$\frac{DP_R}{Dt} = \frac{D}{Dt}\left(p + \frac{\rho W^2}{2} - \frac{\rho\omega^2 r^2}{2}\right) = 0 . \tag{3.9}$$

Boundary Conditions

The governing equations for steady incompressible or steady subsonic compressible flow constitute an elliptic boundary value problem which must be solved by iteration over the whole domain. An impeller with a finite number of blades influences the upstream and downstream flow fields, and,

theoretically, this domain of influence extends an infinite distance from the blading. Consequently, boundary conditions (e.g., pressure, velocity, etc.) must be specified at a sufficiently large distance from the blade leading and trailing edges that the solution is not restricted.

Consider for illustrative purposes, the two-dimensional radial-flow impeller shown schematically in Fig. 3.1. The boundaries of the flow field are the blade surfaces, and the upstream and downstream boundaries at constant radius which are located far enough (typically a distance on the order of one blade spacing) from the impeller to ensure uniform flow conditions at these stations. These upstream and downstream boundaries enclose all the blades; however, by assuming circumferentially periodic flow, the flow conditions along lines of constant radius are cyclic with a period equal to the blade spacing. This permits us to restrict the solution to a region that encloses the equivalent flow between any two blades and the upstream and downstream boundaries as shown in Fig. 3.1.

In general, the periodic boundaries outside the bladed region of the impeller must be determined as part of the overall solution. Downstream of the impeller exit these boundaries must be shaped such that the angular momentum of the fluid is conserved. Furthermore, the static pressures corresponding to two streamlines on opposite

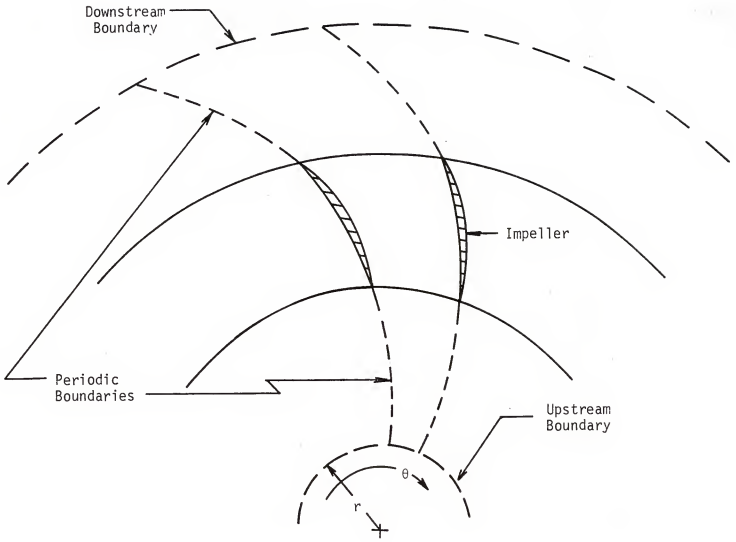

Fig. 3.1. Boundaries for Inviscid Flow Analysis

sides of a blade must be equal where they join at the trailing edge. For an inviscid flow this is equivalent to the Kutta condition which requires that the relative velocities be equal.

For the three-dimensional problem considered in this analysis, the domain of the solution also includes the hub and shroud surfaces of the impeller and their extentions to the upstream and downstream boundaries. In addition, the θ coordinates defining the periodic boundaries are now a function of both radial and axial location. Once the three-dimensional domain of the flow field is specified, the bounding surfaces may be taken as stream surfaces subject to the condition that the normal component of relative velocity be zero on these surfaces.

At the upstream boundary the absolute flow is assumed to be axisymmetric since a steady relative flow can exist in the impeller only when this requirement is satisfied. Consequently, the relative flow at this station is also axisymmetric, but not irrotational as a result of the change in reference frame.

Flow conditions at the downstream boundary may be assumed uniform with respect to θ and z, but it is not clear whether the outflow boundary conditions should be completely specified because of the possibility of restricting the elliptic nature of the flow. This problem is resolved by prescribing the minimum number of boundary

conditions at the downstream boundary which will still provide a convergent numerical solution.

Coordinate System and Geometry

The present analysis is applicable to shrouded centrifugal impeller configurations ranging from a two-dimensional impeller with a radial inlet and outlet (see Fig. 3.1) to a fully three-dimensional impeller with axial inflow and radial outflow. In all cases, a vaneless diffuser of constant axial width will form the hub and shroud surfaces in the region immediately downstream of the blading. A typical shrouded impeller with an axial inlet, a radial outlet, and a vaneless diffusing section is shown schematically in Fig. 3.2.

The hub and shroud surfaces which enclose the flow passages are surfaces of revolution. Thus, in order to completely describe an impeller's geometry it is necessary to specify the following: the hub and shroud coordinates, r and z; the mean blade shape, $\theta_b(r,z)$; the blade thickness distribution as a function of r and z; and the number of blades.

A convenient means of visualizing the complex geometry of a centrifugal impeller is to project its three-dimensional contours onto planes. The meridional plane (Fig. 3.3) is an r-z plane containing the axis of rotation

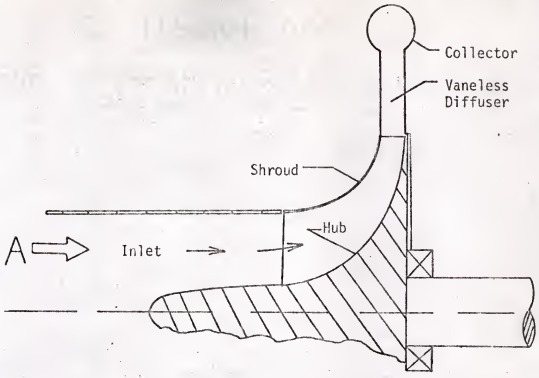

Fig. 3.2. Typical Centrifugal Impeller

View from A
(Shroud Removed)

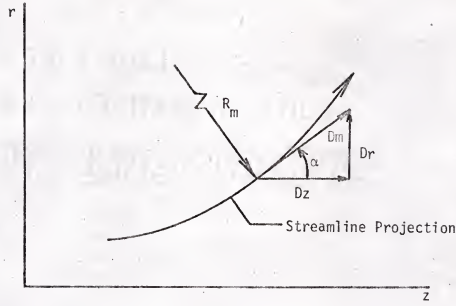

Fig. 3.3. Meridional Plane

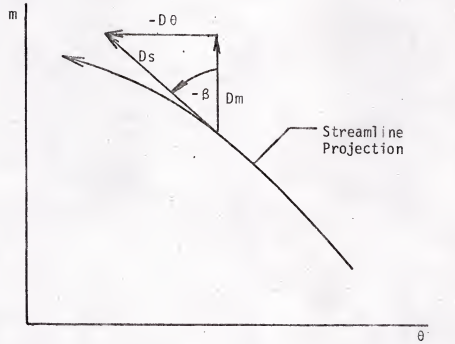

Fig. 3.4. m-θ Plane

and gives a true representation of the hub and shroud shapes. Parameters of interest in this plane are meridional distance or arc length (m), meridional flow angle (α), and meridional radius of curvature (R_m); these are defined in Fig. 3.3.

Another useful two-dimensional projection is obtained when meridional distance and circumferential angle are used as coordinates. The m-θ plane (Fig. 3.4) provides a picture of the flow in the blade-to-blade direction as well as the blade shape and thickness distribution. It should be noted, however, that angles and distances will be distorted when viewed in this plane unless the original coordinates lie on a cylindrical surface concentric with the z-axis. The arc length measured along a streamline of the relative flow (s) is related to meridional distance through the relative flow angle (β) as shown in Fig. 3.4.

The relative velocity components and their relationships with the flow angles α and β are illustrated in Fig. 3.5 Physically, α is the angle measured from the z-axis to the tangent to a streamline projection in the meridional plane, and β is the angle between a relative streamline and its projection on the meridional plane. The convention followed here is that β is positive when measured in the direction of rotation, i.e., the direction of increasing θ. In like manner, the velocity component W_θ is positive only when it points in the direction of rotation.

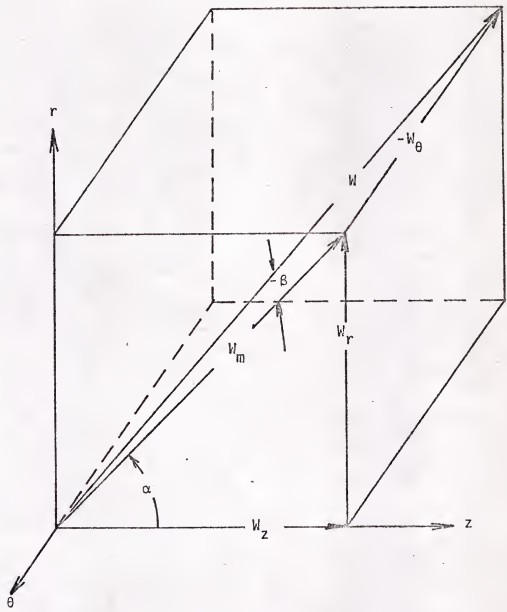

Fig. 3.5. Relative Velocity Components

A velocity diagram (or triangle) showing the relation between the absolute flow and the relative flow is given in Fig. 3.6. At any point within the impeller, the local blade speed (ωr) is equal to the magnitude of the vector differences between the absolute velocity ($\vec{V}$) and the relative velocity ($\vec{W}$).

Method of Analysis

A three-dimensional solution of the governing equations is obtained here through iteration using the method of streamline curvature [3, 4]. This approach requires that the coordinates of several relative streamlines be known or assumed throughout the flow field. In contrast to standard finite difference techniques where the grid point locations remain fixed during the computations, the streamline curvature analysis involves repeated adjustment of the calculation grid.

In order to provide an initial approximation to the streamline locations, the impeller passage is divided into a number of stream tubes of equal mass flow rate. The bounding surfaces of these stream tubes, including the solid surfaces of the passage, are known as stream surfaces of the first and second kind, or S1 and S2 stream surfaces in the terminology of reference [1], and their mutual intersections take place along the relative streamlines.

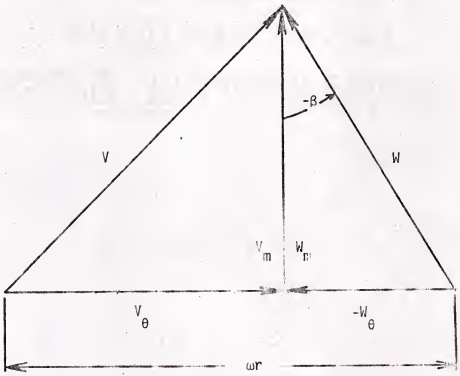

Fig. 3.6. Velocity Triangle

Fig. 3.7(a) depicts an S1 stream surface defined by the loci of fluid particles originally lying on a circular arc such as AEC upstream of the blades, and an S2 stream surface formed by fluid particles originally lying on a radial line such as DEF. In passing through an impeller, these surfaces will become skewed. This effect is illustrated in Fig. 3.7(b) which shows the meridional plane view of the S1 stream surface. A similar twisting occurs for an S2 stream surface.

In the three-dimensional flow analysis presented herein, the relative stream surfaces are allowed to assume whatever shape is required to satisfy the governing equations. This represents a considerable improvement over existing two-dimensional or quasi-three-dimensional methods which require that the shapes of the stream surfaces be assumed.

Problem Formulation

In the analysis to follow, the equation of motion will be combined with the energy equation to eliminate the static pressure, yielding a principal equation for the total differential of velocity in terms of flow conditions along a streamline. The resulting equation is then used in conjunction with an integral form of the conservation of mass equation to relate relative velocities at adjacent streamlines and determine the flow distribution at a given passage cross-section.

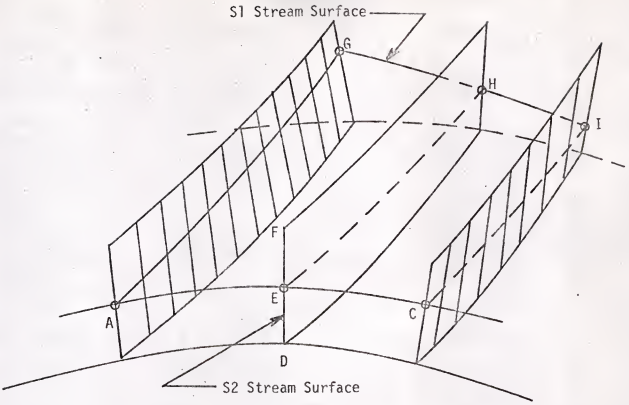

(a)

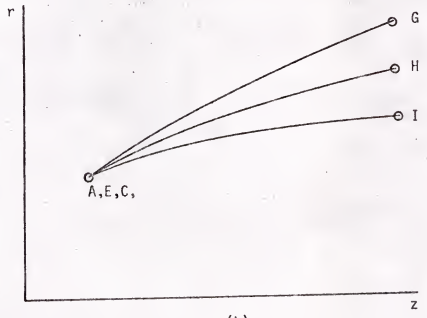

(b)

Fig. 3.7. S1 and S2 Stream Surfaces

A relation between static pressure and enthalpy which applies to isentropic flow along a streamline is obtained from the Gibbs equation, i.e.,

$$Dh = \frac{1}{\rho} Dp \quad .$$

Substitution of this equation into the energy equation (3.8) gives the following results for the differential change in pressure along a relative streamline:

$$\frac{1}{\rho} Dp = D\left(\frac{\omega^2 r^2}{2}\right) - D\left(\frac{W^2}{2}\right) \quad . \tag{3.10}$$

An expression identical to equation (3.10) is obtained from equation (3.9) for inviscid, incompressible flow.

Next, equation (3.10) is integrated along a streamline from an upstream station where flow conditions are known, to an arbitrary location within the impeller. Expressing the result in terms of the static enthalpy for isentropic compressible flow, and the static head for incompressible flow, we get

$$h - h_i = \frac{\omega^2 r^2}{2} - \frac{\omega^2 r_i^2}{2} + \frac{W_i^2}{2} - \frac{W^2}{2} \tag{3.11}$$

where the subscript denotes inlet conditions. Referring to Fig. 3.6, the relative velocity may be expressed in terms of

the absolute velocity using $V_m = W_m$ and $V_\theta = W_\theta + \omega r$, or

$$V^2 = W^2 + 2\omega r V_\theta - \omega^2 r^2 \quad .$$

Then making use of the definition of total enthalpy or total head, i.e.,

$$H \equiv h + \frac{V^2}{2}$$

equation (3.11) becomes

$$h = H_i - \omega(rV_\theta)_i + \frac{\omega^2 r^2 - W^2}{2} \qquad (3.12)$$

When equation (3.12) is differentiated we obtain the following relation for the total differential of static pressure or enthalpy:

$$\frac{1}{\rho}dp = dh = dH_i - \omega d(rV_\theta)_i + \omega^2 r dr - W dW \qquad (3.13)$$

where dH_i is zero throughout the flow field only when the flow at the upstream station has uniform total enthalpy or total head, and $d(rV_\theta)_i$ is zero provided the absolute flow is irrotational at this station (a reasonable assumption when there are no inlet guide vanes).

The three component momentum equations (3.3) contain spatial derivatives of pressure. Noting that the total differential of static pressure in a steady relative flow is given by

$$dp = \frac{\partial p}{\partial r}dr + \frac{\partial p}{\partial \theta}d\theta + \frac{\partial p}{\partial z}dz$$

we may rewrite equation (3.13) in the form

$$\frac{1}{\rho}\frac{\partial p}{\partial r}dr + \frac{1}{\rho}\frac{\partial p}{\partial \theta}d\theta + \frac{1}{\rho}\frac{\partial p}{\partial z}dz = dH_i - \omega d(rV_\theta)_i + \omega^2 r dr - WdW \quad .$$

Next, the three component equations are substituted into the left-hand side of the preceding expression yielding

$$\left[\frac{DW_r}{Dt} - 2\omega W_\theta - \omega^2 r - \frac{W_\theta^2}{r}\right]dr + \left[\frac{DW_\theta}{Dt} + 2\omega W_r + W_r W_\theta\right] rd\theta$$

$$+ \frac{DWz}{Dt}dz = -dH_i + \omega d(rV_\theta)_i - \omega^2 r dr + WdW \quad .$$

Then solving for the total differential of the relative velocity, we obtain

$$\begin{aligned} dW = {} & \frac{1}{W}\left[\frac{DW_r}{Dt} - 2\omega W_\theta - \frac{W_\theta^2}{r}\right]dr \\ & + \frac{1}{W}\left[r\frac{DW_\theta}{Dt} + 2\omega r W_r + W_r W_\theta\right]d\theta \\ & + \frac{1}{W}\frac{DW_z}{Dt}dz + \frac{1}{W}\left[dH_i - \omega d(rV_\theta)_i\right] . \end{aligned} \qquad (3.14)$$

Equation (3.14) may be put in a form suitable for numerical computation by manipulating the streamwise derivatives. Along any streamline of the relative flow, the following relation holds:

$$\frac{D(\ )}{Dt} = W \frac{D(\ )}{Ds}$$

where s is the coordinate in the streamline direction. A similar relation applies for any desired direction, e.g.,

$$\frac{D(\ )}{Dt} = W_m \frac{D(\ )}{Dm} \tag{3.15}$$

where Dm is the increase in the coordinate m in the meridional plane which a fluid particle undergoes as it moves an incremental distance Ds in the flow direction. Using equation (3.15) we can write the substantial derivatives in equation (3.14) as

$$\frac{DW_r}{Dt} = W_m \frac{DW_r}{Dm}, \qquad \frac{DW_\theta}{Dt} = W_m \frac{DW_\theta}{Dm}, \qquad \frac{DW_z}{Dt} = W_m \frac{DW_z}{Dm}.$$

Furthermore, the relative velocity components and the flow angles shown in Fig. 3.5 are related as follows:

$$W_m = W\cos\beta \qquad W_r = W_m\sin\alpha$$

$$W_\theta = W\sin\beta \qquad W_z = W_m\cos\alpha \; . \tag{3.16}$$

Now, making use of the foregoing relations we obtain

$$\frac{DW_r}{Dt} = W_m\left[\sin\alpha\frac{DW_m}{Dm} + W_m\cos\alpha\frac{D\alpha}{Dm}\right]$$

$$\frac{DW_\theta}{Dt} = W_m\left[\tan\beta\frac{DW_m}{Dm} + \frac{W_m}{\cos^2\beta}\frac{D\beta}{Dm}\right]$$

$$\frac{DW_z}{Dt} = W_m\left[\cos\alpha\frac{DW_m}{Dm} - W_m\sin\alpha\frac{D\alpha}{Dm}\right]$$

where $\frac{D\alpha}{Dm}$ is the curvature of a streamline measured in the r-z or meridional plane, and $\cos\beta\frac{D\beta}{Dm}$ is the streamline curvature in the m-θ plane since $\cos\beta = \frac{Dm}{Ds}$. Finally, the desired equation for the differential change in relative velocity may be written as

$$dW = Adr + Bd\theta + Cdz + \frac{1}{W}\left(dH_i - \omega d(rV_\theta)_i\right) \tag{3.17}$$

where

$$A = \sin\alpha\cos\beta\frac{DW_m}{Dm} + W\cos\alpha\cos^2\beta\frac{D\alpha}{Dm}$$

$$- 2\omega\sin\beta - \frac{W\sin^2\beta}{r}$$

$$B = r\sin\beta\frac{DW_m}{Dm} + rW\frac{D\beta}{Dm} + 2\omega r\sin\alpha\cos\beta \qquad (3.18)$$

$$+ W\sin\alpha\sin\beta\cos\beta$$

$$C = \cos\alpha\cos\beta\frac{DW_m}{Dm} - W\sin\alpha\cos^2\beta\frac{D\alpha}{Dm} \quad .$$

Equations (3.17) and (3.18) are similar in form to those used in existing quasi-three-dimensional analyses, e.g., references [5] and [11]. In these methods, however, the principal equation is applied to a single stream surface: a hub-to-shroud (S2) surface which usually coincides with the mean blade shape, or a blade-to-blade (S1) surface comprising a surface of revolution.

The terms making up the right-hand side of equation (3.17) are functions of streamline geometry, the streamwise distribution of meridional velocity, and flow conditions at the upstream station. If these terms are known or estimated during an iteration cycle of the calculation, the relative velocity at any point along a streamline can be determined from conditions on an adjacent streamline by integration in the appropriate direction.

In order to apply equation (3.17) together with a suitable form of the continuity equation, a three-dimensional calculation grid must first be established. This is done by dividing up the length of the flow channel with a number

of stations or surfaces approximately normal to the meridional flow direction. Many of the two-dimensional and quasi-three-dimensional meridional flow analyses mentioned previously employ an orthogonal grid to solve the governing equations. But recently, Katsanis [7] developed a method where quasi-orthogonals or fixed straight lines are used in place of streamline normals in the meridional plane. This approach is extended to fully three-dimensional flow by rotating the straight lines about the z-axis to form conic surfaces which remain fixed in position during the computations. As a result, the intersections of the streamlines with the conic surfaces form the grid system as shown in Fig. 3.8

The meridional plane view of Fig. 3.8(a) shows a section of one ray of a typical conic surface extending from hub to shroud. The grid points indicated by circles represent the intersections of the meridional streamline projections for one of the S2 stream surfaces with the conic surface.

A view normal to the conic surface is depicted in Fig. 3.8(b). On this surface, the coordinate n is the distance along a ray in the meridional plane measured from the impeller hub. It is important to note that the hub and shroud surfaces, the blade surfaces, and the S1 and S2 stream surfaces shown here form the boundaries of stream tubes carrying equal mass flow rates.

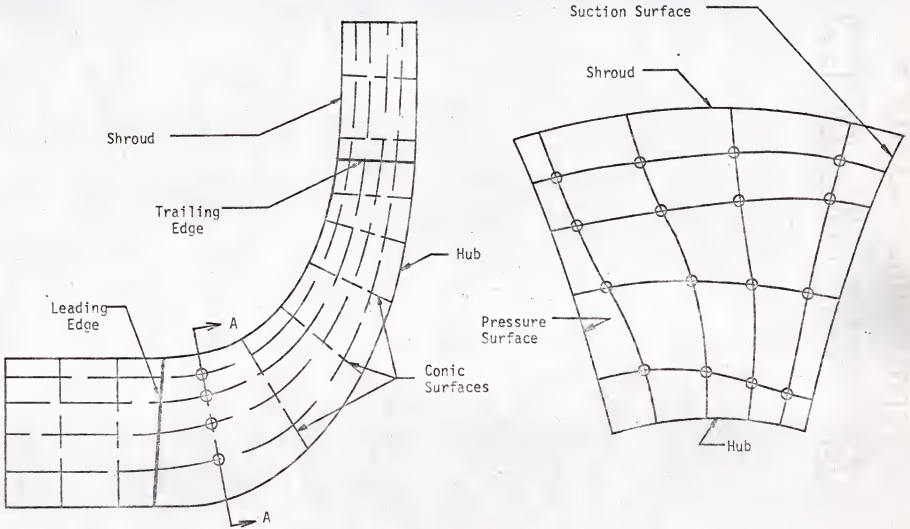

Fig. 3.8. Calculation Grid for Inviscid Flow Analysis

In order to satisfy the requirement of equal mass flow per stream tube, the conservation of mass equation (3.4) is employed as a surface integral at each passage cross-section or conic surface to adjust the streamline locations. This integration is performed in an alternating manner until no further adjustment is required: first from hub to shroud along all S2 stream surfaces; then from blade to blade along all S1 stream surfaces. For each integration along a given stream surface, the two adjacent stream surfaces of the same kind and the passage walls make up the boundaries of the cross-sectional flow area on the conic surface. The required mass flow through this area is determined at the outset by the total passage flow rate and the number of S1 and S2 stream surfaces specified.

Since the mass flow rate across a given surface is the integral of the density times the normal velocity component over the area of the surface, it follows that:

$$\dot{m} = \iint_A \rho W_n dA$$

where W_n is the relative velocity component normal to the conic surface. Referring to Fig. 3.9, the normal velocity component for a particular streamline is given by

$$W_n = W_m \cos(\phi - \alpha) \qquad (3.19)$$

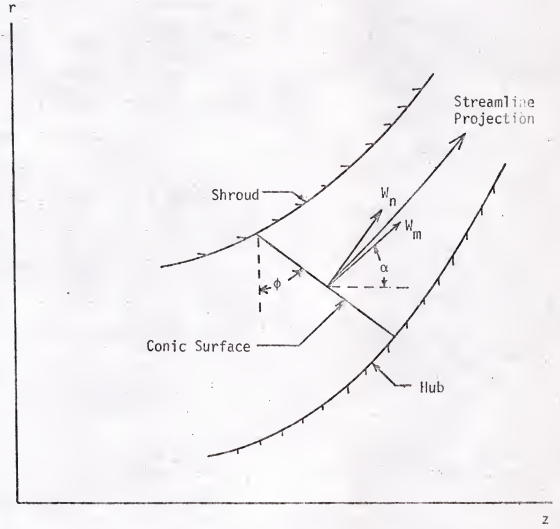

Fig. 3.9. Normal Velocity Component

where ϕ is the angle measured at the impeller shroud between a plane normal to the z-axis and the conic surface, and α and W_m are the meridional flow angle and the velocity component defined previously. Now, using equation (3.19) and the conic surface coordinates shown in Fig. 3.8(b), the conservation of mass equation becomes

$$\dot{m} = \iint_A \rho W \cos\beta \cos(\phi-\alpha) r d\theta dn \qquad (3.20)$$

where the limits of integration depend upon the type of stream surface (S1 or S2) along which the integration proceeds.

Consider for example, the flow integration at a given streamwise station along the S1 stream surface extending from blade to blade shown in Fig. 3.10(a). In this case equation (3.20) is evaluated as an iterated double integral in the following form:

$$\dot{m} = \int_{\theta_1}^{\theta_2} \left[\int_{n_1}^{n_2} \rho W \cos\beta \cos(\phi-\alpha) r dn \right] d\theta \qquad (3.21)$$

where the limits of the inner integral are determined by the coordinates of the two adjacent S1 stream surfaces, and the limits of the outer integral are the coordinates corresponding to the intersections of the intermediate S1 stream surface with the blade surfaces. First, equation (3.17) is

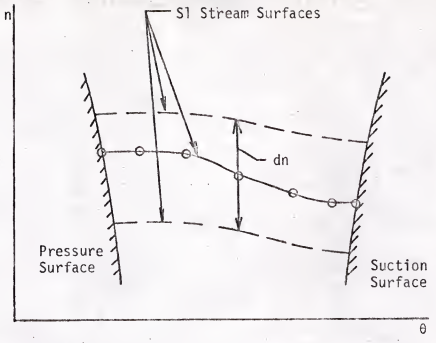

(a) Integration Along an S1 Stream Surface

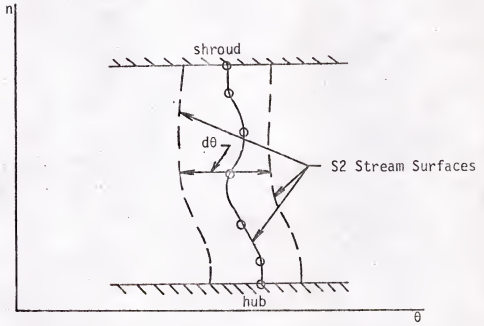

(b) Integration Along an S2 Stream Surface

Fig. 3.10. Boundaries for Mass Flow Integration

integrated along the intermediate S1 surface from the pressure side to the suction side of the passage. This gives the relative velocity at each of the grid points located on the conic surface at the intersections of the S1 surface with the S2 stream surfaces. The velocity at the pressure surface used to start the integration is initially an approximation based on the previous iteration cycle. Next, using the relative velocity distribution just obtained for the intermediate surface, equation (3.17) is integrated between the adjacent S1 surfaces at each grid point while holding θ constant. Then the inner integral of equation (3.21) is evaluated for each θ value corresponding to a grid point on the intermediate surface. With this information, equation (3.21) can be integrated with respect to θ across the passage to determine the mass flow rate.

A similar procedure is employed for the S2 stream surfaces. Fig. 3.10(b) shows an S2 surface extending from hub to shroud. For this situation the appropriate form of equation (3.20) is

$$\dot{m} = \int_{n_1}^{n_2} \left[\int_{\theta_1}^{\theta_2} \rho W \cos\beta \cos(\phi-\alpha) r d\theta \right] dn \qquad (3.22)$$

where the limits of the inner integral are determined by the positions of the adjacent S2 surfaces, and the limits of the outer integral correspond to the hub and shroud coordinates on the conic surface.

The mass flow rate calculated using either of the above procedures is compared to the actual mass flow, and if they do not agree, a new estimate is made for the velocity at the first grid point and the calculation is repeated. When the flow rates do match within tolerance, the distribution of integrated mass flow along an intermediate stream surface is used to adjust the grid point coordinates (θ for an S1 surface and n for an S2 surface) such that the equal mass flow per stream tube requirement is satisfied. A complete solution is achieved when the required variations in the grid point locations are sufficiently small throughout the flow field.

Numerical Solution

The approach used to obtain an inviscid flow solution for a particular impeller geometry and operating condition may be summarized as follows:

1 Specify the following input data: hub and shroud contours, mean blade shape, normal blade thickness, number of blades, leading and trailing edge coordinates, rotational speed, mass flow rate, fluid conditions at the inlet station, and number of grid points.

2 Assume initial stream surface locations and thereby establish coordinates for all grid points. Estimate initial values for all parameters in equation (3.17) at the grid points.

3 Compute a refined estimate of all parameters by using a single S2 stream surface solution with blade-to-blade flow variations neglected.

4 Relocate all S1 stream surfaces to satisfy the equal mass flow per stream tube criterion.

5 Adjust the upstream and downstream periodic boundaries so that angular momentum is conserved.

6 Begin the main iteration cycle wherein the principal equations (3.17) and (3.21) or (3.22) are applied alternately along all S1 stream surfaces, and then along all S2 stream surfaces.

7 Calculate the flow angles and streamwise derivatives required in the evaluation of equation (3.17) using the results of the previous iteration cycle.

8 Starting at the upstream station, the principal equations are integrated along each blade-to-blade or hub-to-shroud stream surface to determine the distribution of mass flow through the area bounded by the adjacent stream surfaces of the same kind.

9 Based on the mass flow distribution just obtained, compute corrected grid point coordinates along each stream surface by inverse interpolation.

10 Correct the blade surface grid point coordinates by converting the local normal blade thickness to an equivalent thickness in the circumferential direction.

11 If the required grid point corrections are not sufficiently small, repeat steps 6 through 10.

12 If the inlet and outlet boundary conditions are not satisfied, repeat steps 5 through 11.

13 Tabulate the results of the flow field calculation for all grid points: streamline coordinates, velocities, flow angles, pressures, etc.

Next, a detailed description is given of some of the numerical techniques employed in the analysis.

Initial approximation for the flow field. Before the iterative calculation cycle can begin, it is necessary to estimate grid point coordinates and velocities throughout the flow field. At the upstream station, values of all flow variables are determinable from the input data, provided conditions at the inlet plane are uniform in r and θ. This permits us to establish the upstream S1 and S2 stream surface coordinates. Their downstream configurations, however, must be determined in subsequent calculations. The axial and radial coordinates of the streamlines are estimated by dividing the flow passage into equal area annuli, and the circumferential coordinates are assumed to be equally spaced between the blades. For compressible flow, the density at each grid point is initially set equal to the inlet value. Relative velocities are computed using a one-dimensional meridional velocity approximation and the local rotor speed.

Upstream flow. The coordinates of the upstream periodic boundaries are determined through application of the conservation of mass and angular momentum equations to the pressure and suction surface stagnation streamlines. The local value of angular momentum per unit mass of fluid is given by the product of radius with the tangential component of the absolute velocity. Referring to Fig. 3.6, this may be written as

$$rV_\theta = rW_\theta + \omega r^2 \quad . \tag{3.23}$$

In the region upstream of the impeller where the flow is not influenced by the blade forces, the angular momentum must be constant along a streamline. If the tangential velocity component V_θ is zero at the inlet station (no prerotation), the usual case when there are no inlet guide vanes, then equation (3.23) becomes

$$W_\theta = -\omega r \quad .$$

The relative fluid angle β is given by $\tan^{-1}(W_\theta/W_m)$ as shown in Fig. 3.6, and also by the following relation in terms of streamline coordinates:

$$\beta = \tan^{-1}\left(r \frac{D\theta}{Dm}\right) \quad . \tag{3.24}$$

Hence, it follows from the above relations that

$$\frac{D\theta}{Dm} = -\frac{\omega}{W_m} \quad . \tag{3.25}$$

If the meridional velocity is known or estimated at each grid point in the inlet region, equation (3.25) can be integrated along the stagnation streamlines yielding the θ coordinates of the upstream periodic boundaries. These boundaries are S2 stream surfaces with a circumferential spacing equal to 2π divided by the number of blades as a result of the circumferential periodicity assumption.

In addition, it is necessary to provide boundary values at the upstream station for the parameters in equation (3.17). As stated in the section on boundary conditions, constraining the flow at the upstream and downstream boundaries may not be realistic except when they are located an infinite distance from the impeller, and especially when the flow within the impeller is highly three-dimensional. Consequently, explicit boundary conditions are employed only when the inlet and exit stations are a reasonable distance (at least one blade spacing for the inlet and at least 25% of the tip radius for the exit) from the blading and the inlet flow is uniform across the passage. The appropriate expressions for the streamwise derivatives of β and θ in this case are as follows:

$$\frac{D\beta}{Dm} = -\frac{\sin\beta\cos\beta}{W_m}\frac{DW_m}{Dm} - \frac{\sin\alpha\cos^2\beta}{W_m}\left[\frac{(rV_\theta)}{r^2}i + \omega\right]$$

$$\frac{D}{Dm} = \frac{\left[\frac{(rV_\theta)}{r^2}i - \omega\right]}{W_m} \qquad (3.26)$$

where the meridional velocity, angular momentum, and flow angles are evaluated at the inlet station. The derivative of meridional velocity $\frac{DW_m}{Dm}$ may be taken as zero for a constant area axial flow passage, and is given by $-\frac{W_m}{r}$ for a constant width radial flow passage with incompressible flow. In either case, uniform flow unaffected by the rotating impeller is implied.

In the general three-dimensional flow situation where the preceding relations do not apply, e.g., the passage cross-sectional area varies upstream of the impeller, the second derivatives of β and θ at the inlet station are specified as some fraction of those at the adjacent grid points. This approach is also followed for the meridional curvature $\frac{D\alpha}{Dm}$, and results in considerably fewer constraints on the flow than a first derivative boundary condition.

Downstream flow. The periodic boundaries downstream of the impeller are determined using the conservation equations for mass and angular momentum, and the condition that the pressure and suction surface streamlines join at constant

pressure at the blade trailing edge (Kutta condition). In addition, boundary conditions at the exit station are calculated in a manner similar to that used for the upstream flow.

At the impeller discharge the angular momentum of the fluid is determined in part by the flow direction which depends upon the shape of the periodic boundaries. Therefore, it is necessary to use a trial and error approach to establish these bounding surfaces. The following procedure is employed:

1 Assume exit stagnation streamlines beginning at the trailing edge and estimate the mass averaged angular momentum imparted to the fluid based on the average meridional velocity and flow angle at the impeller discharge.

2 For this value of angular momentum, calculate the area-averaged meridional velocity at each downstream station and integrate equation (3.27) from the trailing edge to the exit station to find the θ coordinates of the periodic boundaries.

$$\theta - \theta_t = \int_{m_t}^{m} \left[\frac{(r\hat{V}_\theta)_t}{r^2 \overline{W}_m} - \frac{\omega}{\overline{W}_m} \right] dm \qquad (3.27)$$

3 Locate the remaining S2 stream surfaces at equal intervals between the periodic boundaries as a first approximation.

4 After satisfying the continuity and momentum equations for the initially chosen periodic boundaries, the Kutta condition is checked at the trailing edge at mid blade height. If this condition is not met, a new set of stagnation streamlines is assumed and the process repeated. The shape of the downstream boundaries is controlled by the value of $(r\hat{V}_\theta)_t$ in equation (3.27), and in the iterative procedure employed here, this parameter is set by specifying the impeller work coefficient $\mu = (\hat{V}_\theta/\omega r)_t$ which is restricted to values between 0 and 1.

5 Once a satisfactory solution is obtained, the flow conditions at the downstream boundary should be examined for circumferential uniformity. If the flow here is not uniform, the downstream station must be located farther from the axis.

Since there is a finite blade thickness at the trailing edge, the inviscid flow will experience a sudden expansion in this region. To provide a smooth transition and a better model of the actual viscous flow, a wake which is stationary relative to the impeller is assumed to start at the trailing edge between the pressure and suction surface S2 stream surfaces which enclose each blade. The thickness of this wake is assumed to vary quadratically with radius ratio (the basis for this model is discussed in Chapter V) from the blade tangential thickness at the trailing edge to zero a short distance downstream.

When the flow is compressible, the average meridional velocity is dependent upon density as well as passage area, and additional calculations are required to determine the periodic boundary shapes. For isentropic flow, the density is given in terms of the inlet total properties and the local temperature by

$$\frac{\rho}{\rho_{0_i}} = \left(\frac{T}{T_{0_i}}\right)^{\frac{1}{\gamma-1}} . \tag{3.28}$$

Using equation (3.12), the following relation is obtained for temperature ratio:

$$\frac{T}{T_{0_i}} = \frac{h}{H_i} = 1 - \frac{W^2 + 2\omega(rV_\theta)_i - \omega^2 r^2}{2C_p T_{0_i}} . \tag{3.29}$$

Then with the velocity triangle relations shown in Fig. 3.7, the density ratio may be written as

$$\frac{\rho}{\rho_{0_i}} = \left[1 - \frac{\omega\{(r\hat{V}_\theta)_t - (rV_\theta)_i\} - \frac{(r\hat{V}_\theta)_t^2}{r^2} - \bar{W}_m^2}{2C_p T_{0_i}} \right]^{\frac{1}{\gamma-1}} . \tag{3.30}$$

An equivalent expression for density ratio is

$$\frac{\rho}{\rho_{0_i}} = \frac{\dot{m}}{\rho_{0_i} A \bar{W}_m}$$

where $\dot{m}$ is the total impeller flow, and A is the cross-sectional area of the vaneless diffuser. The last two equations are solved iteratively for $\bar{W}_m$ at each radial station downstream of the impeller. A similar approach is employed in the first iteration cycle to provide an initial approximation for the impeller exit conditions.

Blade surface coordinates. Two types of impeller blading are considered in the present analysis: (1) radial blades for which the mean blade shape θ_b is a function of the axial coordinate (z) only, and (2) blades for which θ_b varies linearly between the hub and shroud along the straight line segments formed by the conic surfaces in the r-z plane.

The normal blade thickness t_n is required as input at the hub and shroud locations for each station. In order to determine the reduced passage area due to blade blockage, and also the coordinates of the grid points on the blade surfaces, the tangential blade thickness is needed. A relation between normal and tangential blade thickness for an arbitrary mean blade shape $\theta_b(r,z)$ is given by the direction cosine between the normal to the mean blade surface $F(r,\theta,z) = \theta - \theta_b(r,z) = 0$ and the tangential direction, i.e.

$$\frac{t_n}{t_\theta} = \hat{n}\cdot\hat{e}_\theta = \frac{\nabla F}{|\nabla F|}\cdot\hat{e}_\theta \quad .$$

As a result, the tangential thickness may be written

$$t_\theta = t_n \sqrt{1 + r^2\left(\frac{\partial\theta_b}{\partial r}\right)^2 + r^2\left(\frac{\partial\theta_b}{\partial z}\right)^2} \quad . \tag{3.31}$$

The partial derivatives in equation (3.31) must be evaluated from the mean blade shape θ_b for specified values of r and z. When radial blades are used $\partial\theta_b/\partial r$ is zero, but in the general case both terms may be finite. Since θ_b is specified along the hub and shroud where the meridional distances do not change during the calculations, it is convenient to compute the total derivative of θ_b with respect to m along these surfaces just once at the outset. Referring to Fig. 3.5, we obtain

$$\frac{d\theta_b}{dm} = \frac{\partial\theta_b}{\partial r}\frac{dr}{dm} + \frac{\partial\theta_b}{\partial z}\frac{dz}{dm} = \frac{\partial\theta_b}{\partial r}\sin\alpha_b + \frac{\partial\theta_b}{\partial z}\cos\alpha_b \tag{3.32}$$

where the meridional flow angle is assumed to vary linearly from hub to shroud. Also, the total derivative of θ_b with respect to n, the distance along a ray of a conic surface in the r-z plane, is given by (see Fig. 3.9):

$$\frac{d\theta_b}{dn} = \frac{\partial\theta_b}{\partial r}\frac{dr}{dn} + \frac{\partial\theta_b}{\partial z}\frac{dz}{dn} = \frac{\partial\theta_b}{\partial r}\cos\phi_b - \frac{\partial\theta_b}{\partial z}\sin\phi_b \qquad (3.33)$$

Solving equations (3.32) and (3.33) simultaneously yields

$$\frac{\partial\theta_b}{\partial r} = \frac{\frac{d\theta_b}{dm}\sin\phi - \frac{d\theta_b}{dn}\cos\alpha_b}{\cos(\phi-\alpha_b)} \qquad (3.34)$$

and

$$\frac{\partial\theta_b}{\partial z} = \frac{\frac{d\theta_b}{dm}\cos\phi - \frac{d\theta_b}{dn}\sin\alpha_b}{\cos(\phi-\alpha_b)} \qquad (3.35)$$

The total derivative $\frac{d\theta_b}{dn}$ is determined from the known values of θ_b at the hub and shroud, and a linear variation of $\frac{d\theta_b}{dm}$ with n is assumed. If the blading is radial,

$$\frac{\partial\theta_b}{\partial z} = \frac{\frac{d\theta_b}{dm}}{\cos\alpha_b} \quad ,$$

and otherwise equations (3.34) and (3.35) are used together with equation (3.31) to find the tangential blade thickness at each pressure and suction surface grid point. Finally, assuming the blade thickness is equally distributed on either side of the mean blade surface, the θ coordinates at the blade surface are computed from

$$\theta = \theta_b \pm \frac{t_\theta}{2r} \quad . \tag{3.36}$$

Flow angles and derivatives. The method used in this analysis to compute the derivatives occurring in equation (3.18), as well as those needed to evaluate flow angles, is the cubic spline fit [56] which is discussed in Appendix A. This technique allows a mathematical representation of a function given at discrete points by fitting a smooth cubic polynomial through the data. Besides function values, the method requires two arbitrary end conditions which correspond to the boundary conditions at the upstream and downstream stations.

For each streamline, the r, θ, and z coordinates and the relative velocity are known or estimated at the grid point locations. First, the meridional flow angle defined in Fig. 3.3 is calculated from

$$\alpha = \tan^{-1}\left(\frac{Dr}{Dz}\right) \quad . \tag{3.37}$$

At the impeller exit the flow angle is usually equal to 90 degrees, and a rotation of coordinates is employed to avoid infinite slopes [8].

Next, the meridional radius of curvature is computed using

$$\frac{1}{R_m} = \frac{D\alpha}{Dm} \tag{3.38}$$

where the meridional distance m is obtained by integrating the following equation along a streamline:

$$Dm = \sqrt{(Dr)^2 + (Dz)^2} \tag{3.39}$$

Although the end point slopes in equations (3.37) and (3.38) are available from the inlet and outlet calculations, better results are often obtained with a less restrictive second derivative end condition (see Appendix A).

The relative flow angle β is calculated from the streamline slope in the m-θ plane (Fig. 3.4) as follows:

$$\beta = \tan^{-1}\left(r \frac{D\theta}{Dm}\right) \tag{3.40}$$

with boundary conditions for θ given by equation (3.26) for the upstream station and by a similar expression for the downstream station.

The remaining parameters in equation (3.18), $\frac{DW_m}{Dm}$ and $\frac{D\beta}{Dm}$, are computed from the streamwise distributions of W_m and β and the appropriate boundary conditions (e.g., equation (3.26)). Finally, the values of A, B, and C are determined at each grid point.

Mass flow integration. A flow integration is performed at each passage cross-section during a given iteration cycle along all S1 or S2 stream surfaces with the exception of the solid surfaces and the periodic boundaries.

In the first iteration cycle, however, this integration is done for a mean S2 stream surface only. Based on the results of each integration, improved estimates for relative velocities and grid point coordinates are determined and the maximum streamline correction is examined for convergence.

Fig. 3.11 depicts a portion of a typical passage cross-section or station as it would appear in n-θ coordinates. The flow area of interest for an S1 stream surface integration is bounded by the surfaces designated by Sl_{j-1} and Sl_{j+1}, and the pressure and suction surfaces of the blades. Since the S1 and S2 stream surfaces divide the passage mass flow into equal parts, the flow rate passing through this area must equal twice the total passage flow divided by one less than the number of S1 stream surfaces. Other information needed for the flow integration includes the distances denoted by $\Delta n_{k,1}$ and $\Delta n_{k,2}$ between the Sl_j stream surface and the adjacent surfaces, the angles α and β along the three S1 surfaces, and the angle ϕ which is constant for a given conic surface. The above parameters are evaluated at each $\theta_{k,j}$ corresponding to a grid point on Sl_j. Those values required on Sl_{j-1} and Sl_{j+1} can be determined quite accurately using piecewise cubic interpolation which is described in Appendix A. A similar procedure is employed for the S2 stream surfaces in which case the stream surface spacing is found in terms of the difference in θ between

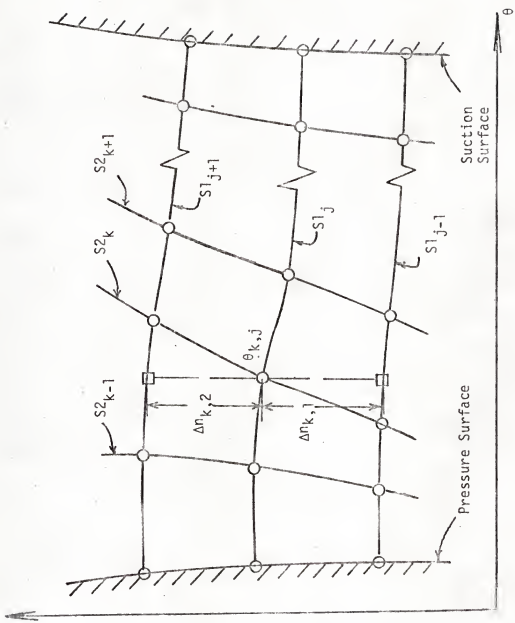

Fig. 3.11. Coordinates for Mass Flow Integration (S1 Stream Surface)

adjacent S2 surfaces and the $S2_k$ stream surface at each value of n corresponding to a grid point on $S2_k$.

Consider the flow integration along the typical S1 stream surface shown in Fig. 3.11. First, the relative velocity $W_{1,j}$ at the pressure surface is estimated from the previous iteration cycle. Then with the parameters in equation (3.17) known at the grid points along $S1_j$, this equation is integrated from the pressure surface to the suction surface. The coordinate changes appearing in equation (3.17) are evaluated from the grid point locations along $S1_j$. Next, the velocities are determined along stream surfaces $S1_{j-1}$ and $S1_{j+1}$ at values of θ corresponding to the grid points along $S1_j$. If a linear variation with n is assumed, the relative velocities are given by

$$W_{k,1} = W_{k,j} - \left(\frac{dW}{dn}\right)_{k,j} \Delta n_{k,1} \tag{3.41}$$

and

$$W_{k,2} = W_{k,j} + \left(\frac{dW}{dn}\right)_{k,j} \Delta n_{k,2} \tag{3.42}$$

with

$$\frac{dW}{dn} = A\cos\phi + C\sin\phi + \frac{1}{W}\left[dH_i - d(rV_\theta)_i\right] \tag{3.43}$$

where ϕ is defined in Fig. 3.9. (Note, if the calculation

is along an S2 stream surface, $\frac{dW}{dn}$ is replaced by $\frac{dW}{d\theta}$ and the velocities are found at constant values of n.) When the flow is compressible, the density is obtained from equation (3.28) at the grid points along Sl_j and also at the interpolated points on Sl_{j-1} and Sl_{j+1}. With the foregoing information the inner integral of equation (3.21), i.e.,

$$\int_{n_1}^{n_2} [\rho W \cos\beta \cos(\phi-\alpha) r] dn$$

can be evaluated for each value of θ on Sl_j using the trapezoidal rule and values of the bracketed term on the three surfaces. Next, equation (3.21) is integrated across the passage yielding the mass flow rate between Sl_{j-1} and Sl_{j+1}. This integration is done numerically using the cubic spline fit technique (Appendix A). It is important to note that a special integration procedure must be employed in the region between the blade surface and the adjacent S2 stream surface whenever there is significant blade lean causing θ to vary from hub to shroud along the blade surface intersection with the conic surface.

An iterative solution is required to find the relative velocity distribution on Sl_j which yields the desired mass flow. The correct distribution is obtained by varying the velocity at the first grid point $W_{1,j}$ using the secant

method to force convergence. However, this approach cannot converge to the desired mass flow if the flow is compressible and choking occurs. During the first stages of the calculation procedure, choked flow in a stream tube may be indicated even though the final solution is completely subsonic.† To avoid stopping the calculations in such situations, the velocity distribution yielding the maximum mass flow less than or equal to the desired value is taken as the correct solution. Another problem which is handled similarly for either compressible or incompressible flow is negative velocities at the pressure surface or hub. This behavior is often observed experimentally at flow rates well below design point, and is referred to as "relative eddy." By allowing negative velocities to occur on the bounding surfaces, the calculations can be completed without an iteration failure.

Once the mass flow rate has been determined as a function of θ along $S1_j$ or n along $S2_k$, corrected values of these coordinates are obtained by inverse interpolation. Again this involves the use of cubic spline curves to fit a curve of distance along $S1_j$ or $S2_k$ versus the integrated mass flow rate between the adjacent stream surfaces. Then,

†Choking occurs in the rotating passages of a turbomachine when the relative Mach number reaches one. In the stationary inlet duct and vaneless diffuser it occurs when the meridional Mach number is one.

interpolated values of θ or n are determined at equal increments in the flow rate. These new coordinates represent the corrected grid points. Rather than adjust the coordinates the indicated amount, which might result in instabilities in the computation, two restrictions are employed. First, an underrelaxation factor is used to limit the change to some fraction of the calculated value, and second, the maximum allowable change in coordinates is related to the actual dimensions of the impeller.

When the stream surface of integration is adjacent to a boundary, it is assumed that the coordinate θ on the hub or shroud surface, or the coordinate n on the blade surface is equal to that of the corresponding grid point on the adjacent surface. This does not apply to the corner grid points which are not really used in the calculation and remain fixed in position. For these points the relative velocity is not determined by the flow integration, and must be computed from equation (3.17) and conditions at the adjacent grid points. When the coordinate adjustment takes place along the S2 surfaces, the corrected values of r and z are calculated from the hub and shroud coordinates and the new values of n by interpolation. It should be noted that the grid point coordinates are not changed until the calculations are completed for the entire flow field. Thus the results of an S1 stream surface calculation cycle become

input to the subsequent S2 surface calculation which determines the input to still another S1 cycle, etc.

The maximum grid point shift, either Δn or $\Delta\theta$, is examined once the calculations are completed at all stations during a given S1 or S2 stream surface cycle. If this shift is within tolerance for both the S1 and S2 surfaces in two consecutive cycles, a solution has been obtained. This solution is only valid, however, for the particular periodic boundary shapes assumed at the inlet and outlet. A complete solution, on the other hand, will result when the upstream and downstream flows satisfy conservation of angular momentum, and the Kutta condition is met at the trailing edge.

Closing Remarks

The three-dimensional inviscid flow calculation procedure described in this chapter represents a considerable advancement over existing two-dimensional and quasi-three-dimensional techniques. In particular, this approach requires none of the conventional assumptions regarding stream surface shape, and thus provides a true three-dimensional analysis. Equally important, the flow conditions at the impeller exit are calculated without the usual recourse to empirical corrections.

However, regardless of how sophisticated an inviscid flow analysis is employed, one cannot expect an accurate

prediction of flow conditions near the impeller exit. This is because viscous effects cannot be ignored in any realistic flow model for a centrifugal impeller. In the next chapter, a three-dimensional turbulent boundary layer analysis is developed as the second step in the construction of a combined inviscid/viscous flow calculation procedure.

CHAPTER IV

BOUNDARY LAYER ANALYSIS

In this chapter, an analysis is presented for three-dimensional turbulent boundary layer flow within the passages of a shrouded centrifugal impeller. The analysis is restricted to the steady relative flow of an incompressible fluid, and it is further assumed that the passage flow comprises a boundary layer region surrounding a frictionless core.

The three-dimensional boundary layer equations are first written for an orthogonal curvilinear coordinate system which corresponds to the projections of the outer inviscid flow streamlines and their orthogonals onto the impeller surfaces. Next, momentum integral equations are derived for two essentially different types of boundary layer flow within the impeller passages: (1) the hub and shroud boundary layers, and (2) the blade surface boundary layers. Individual calculation methods are then developed which include the important effects of secondary flow. Interactions between the hub, shroud, and blade boundary layers are taken into account using a simple momentum transport model for

the corner regions proposed by Moore [46]. The resulting prediction technique provides a complete description of the impeller flow when used in conjunction with the inviscid flow analysis presented in Chapter III.

Governing Equations

The equations governing the flow of a constant property fluid relative to a coordinate system rotating at constant angular velocity about an arbitrary axis in space are the continuity equation

$$\nabla \cdot \vec{W} = 0 \tag{4.1}$$

and the momentum equation

$$\frac{\partial \vec{W}}{\partial t} + \vec{W} \cdot \nabla \vec{W} + 2\vec{\omega} \times \vec{W} + \vec{\omega} \times (\vec{\omega} \times \vec{r}) = -\frac{\nabla p}{\rho} + \nabla \cdot \bar{\bar{\tau}} \tag{4.2}$$

where $\bar{\bar{\tau}}$ represents the sum of the time-averaged turbulent stress tensor and the molecular stress tensor.

The boundary layer equations will be formulated in orthogonal curvilinear coordinates. In this system, the location of a point in the flow field is determined by the values of the coordinates (x_i, i=1,2,3) at the intersection of the surfaces x_1=constant, x_2=constant, and x_3=constant.

The differential arc length $d\ell$ is related to the infinitesimal changes in the coordinates x_i through the metric coefficients or scale factors h_i, i.e.,

$$(d\ell)^2 = h_1^2(dx_1)^2 + h_2^2(dx_2)^2 + h_3^2(dx_3)^2 \qquad (4.3)$$

where h_1, h_2 and h_3 are generally functions of the coordinates x_i.

For this coordinate system with velocity components u, v and w, the equation of continuity becomes

$$\frac{1}{h_1h_2h_3}\left[\frac{\partial}{\partial X_1}(h_2h_3u) + \frac{\partial}{\partial X_2}(h_1h_3v) + \frac{\partial}{\partial X_3}(h_1h_2w)\right] = 0 \qquad (4.4)$$

The component form of the momentum equation for steady relative flow is [57]

1-momentum

$$\frac{u}{h_1}\frac{\partial u}{\partial X_1} + \frac{v}{h_2}\frac{\partial u}{\partial X_2} + \frac{w}{h_3}\frac{\partial u}{\partial X_3} + \frac{uv}{h_1h_2}\frac{\partial h_1}{\partial X_2} - \frac{v^2}{h_1h_2}\frac{\partial h_2}{\partial X_1} + \frac{uw}{h_1h_3}\frac{\partial h_1}{\partial X_3} - \frac{w^2}{h_1h_3}\frac{\partial h_3}{\partial X_1}$$

$$= -\frac{1}{\rho h_1}\frac{\partial p}{\partial X_1} + \frac{\omega^2 r}{h_1}\frac{\partial r}{\partial X_1} - 2(\omega_2 w - \omega_3 v) + \frac{1}{\rho h_3}\frac{\partial \tau_1}{\partial X_3} \qquad (4.5)$$

2-momentum

$$\frac{u}{h_1}\frac{\partial v}{\partial x_1} + \frac{v}{h_2}\frac{\partial v}{\partial x_2} + \frac{w}{h_3}\frac{\partial v}{\partial x_3} + \frac{uv}{h_1 h_2}\frac{\partial h_2}{\partial x_1} - \frac{u^2}{h_1 h_2}\frac{\partial h_1}{\partial x_2} + \frac{vw}{h_2 h_3}\frac{\partial h_2}{\partial x_3} - \frac{w^2}{h_2 h_3}\frac{\partial h_3}{\partial x_2}$$

$$= -\frac{1}{\rho h_2}\frac{\partial p}{\partial x_2} + \frac{\omega^2 r}{h_2}\frac{\partial r}{\partial x_2} - 2(\omega_3 u - \omega_1 w) + \frac{1}{\rho h_3}\frac{\partial \tau_2}{\partial x_3} \qquad (4.6)$$

3-momentum

$$\frac{u}{h_1}\frac{\partial w}{\partial x_1} + \frac{v}{h_2}\frac{\partial w}{\partial x_2} + \frac{w}{h_3}\frac{\partial w}{\partial x_3} + \frac{uw}{h_1 h_3}\frac{\partial h_3}{\partial x_1} - \frac{u^2}{h_1 h_3}\frac{\partial h_1}{\partial x_3} + \frac{vw}{h_2 h_3}\frac{\partial h_3}{\partial x_2} - \frac{v^2}{h_2 h_3}\frac{\partial h_2}{\partial x_3}$$

$$= -\frac{1}{\rho h_3}\frac{\partial p}{\partial x_3} + \frac{\omega^2 r}{h_3}\frac{\partial r}{\partial x_3} - 2(\omega_1 v - \omega_2 u) \qquad (4.7)$$

In equations (4.5)-(4.7) the coordinate x_3 is taken normal to the surface, and the usual boundary layer simplifications [58] have been applied to the viscous terms. Turbulent normal stresses have been neglected, and terms the order of magnitude of the boundary layer thickness (assuming that u is the order (1) and $\delta \ll 1$) or smaller have been dropped. Also, τ_1 and τ_2 denote the total (laminar plus turbulent) shear stresses in the directions of the surface orthogonals x_1 and x_2. The terms involving derivatives of the metric coefficients h_i include the geodesic curvatures of the curves x_j=constant in the plane of x_i and x_j. In indicial notation the six geodesic curvatures are given by

$$K_{ij} = -\frac{1}{h_i h_j}\frac{\partial h_i}{\partial X_j} \qquad (i,j = 1,2,3) \tag{4.8}$$

One simplification of the governing equations which is quite reasonable for boundary layer applications is to specify $h_3 = 1$[17]. With this assumption, x_3 is interpreted as the distance along a straight line normal to the surface. If the surface curvature is small with respect to the boundary layer thickness,† the resulting system closely approximates a triply orthogonal coordinate system in the region of interest. Furthermore, the curvatures K_{31} and K_{32} are eliminated from the equations.

Streamline Coordinates

A choice remains for the coordinates x_1 and x_2 lying in the surface x_3 = constant. The most suitable alternatives for the complicated flow path of an impeller are (1) a coordinate system based on the flow channel geometry, e.g., meridional coordinates [20], and (2) a streamline coordinate system employing the surface projections of the inviscid core flow streamlines and their orthogonal trajectories. The first possibility offers the advantage of simplifying the evaluation of the metric coefficients h_1 and h_2 [17], while the second choice leads to convenient boundary conditions at the outer edge of the boundary layer [18].

†The boundary layer thickness δ is defined as the distance normal to the surface at which the streamwise velocity profile deviates from the inviscid flow velocity profile by less than 1%.

In addition, the streamline coordinate system allows the use of established two-dimensional turbulent boundary layer velocity profile and shear stress relations as a reasonable approximation to the streamwise flow [19]. Based on these considerations, a streamline coordinate system appears the best choice for the present application.

A right-handed streamline coordinate system is depicted in Fig. 4.1. The boundary layer velocity component in the streamwise direction is denoted by u, and x_1 coincides with the direction of a streamline just outside the boundary layer. The metric coefficients (h_1,h_2,h_3) determine the length elements in the coordinate directions as follows:

$$\begin{aligned} ds &= h_1 dx_1 \\ dn &= h_2 dx_2 \\ dy &= dx_3 \end{aligned} \tag{4.9}$$

where s is the distance measured along the streamline projected on the surface $(x_3=0)$, n is the distance measured along the surface orthogonals, and y is normal to the surface $(h_3=1)$. Henceforth, s, n and y will be used to denote the coordinate directions and distances in streamline coordinates.

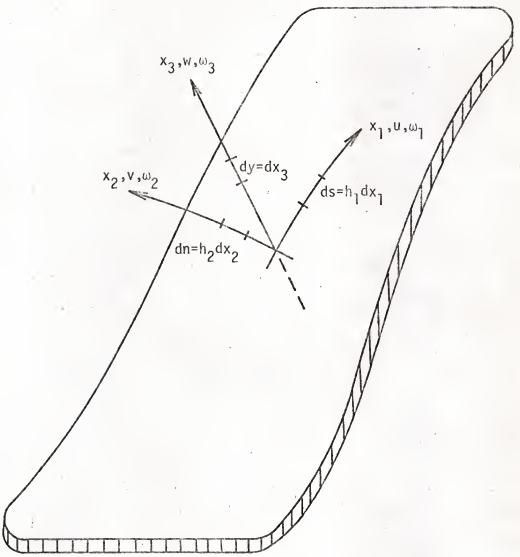

Fig. 4.1. Streamline Coordinate System

The continuity equation in s, n and y coordinates is

$$\frac{\partial u}{\partial s} - K_{21}u + \frac{\partial v}{\partial n} - K_{12}v + \frac{\partial w}{\partial y} - K_{13}w - K_{23}w = 0 \qquad (4.10)$$

where the geodesic curvatures K_{21} and K_{12} may be interpreted physically as the streamline convergence or divergence, and the local curvature of the streamlines in the tangent plane, respectively. The terms K_{13} and K_{23} represent the streamwise and lateral curvatures of the surface y=0.† By performing an order of magnitude analysis similar to that of reference [59], it can be shown that the last two terms of equation (4.10) may be neglected when $\delta/R_c \ll 1$, where R_c is the radius of curvature of the surface in the direction of s or n. For most practical impeller designs this is the case, and the appropriate form of the continuity equation is

$$\frac{\partial u}{\partial s} - K_{21}u + \frac{\partial v}{\partial n} - K_{12}v + \frac{\partial w}{\partial y} = 0 \qquad (4.11)$$

An order of magnitude analysis of equations (4.5)-(4.7) and consideration of the impeller flow path geometry

†Consider the case of axial flow past an arbitrary body of revolution. The geodesic curvature K_{23} is simply the reciprocal of the local body radius multiplied by the cosine of the meridional angle ($\alpha = \tan^{-1}(dr/dz)$), and K_{13} is the local surface curvature in the meridional plane ($d\alpha/dm$).

permit the following simplifying assumptions for the boundary layer flow:

1 The Coriolis acceleration term $\omega_1 w$ in equation (4.6) is negligible compared to $\omega_3 u$, and the term $\omega_2 w$ in equation (4.5) is small relative to $\omega_3 v$ [18] except on the blade surfaces in the radial portion of an impeller where $\omega_2 \approx \omega$ and $\omega_3 \approx 0$.

2 The convective acceleration terms in the 3-momentum equation (4.7) are of the order of magnitude of the boundary layer thickness (since w is of order (δ)), and thus may be neglected.

3 The terms containing the lateral curvature K_{23} are negligible because (i) the boundary layers are reasonably thin on the hub and shroud surfaces in the axial portion of the impeller where K_{23} is the largest, and (ii) the blade surfaces are nearly flat in the hub-to-shroud direction.

With the foregoing simplifications the component momentum equations written for s, n and y coordinates are

s-momentum

$$u\frac{\partial u}{\partial s} + v\frac{\partial u}{\partial n} + w\frac{\partial u}{\partial y} - K_{12}uv + K_{21}v^2 - K_{13}uw$$

$$= -\frac{1}{\rho}\frac{\partial p}{\partial s} + \omega^2 r\frac{\partial r}{\partial s} + 2\omega_3 v - 2\omega_2 w + \frac{1}{\rho}\frac{\partial \tau_1}{\partial y} \qquad (4.12)$$

n-momentum

$$u\frac{\partial v}{\partial s} + v\frac{\partial v}{\partial n} + w\frac{\partial v}{\partial y} - K_{21}uv + K_{12}u^2$$
$$= -\frac{1}{\rho}\frac{\partial p}{\partial n} + \omega^2 r\frac{\partial r}{\partial n} - 2\omega_3 u + \frac{1}{\rho}\frac{\partial \tau_2}{\partial y} \qquad (4.13)$$

y-momentum

$$K_{13}u^2 = -\frac{1}{\rho}\frac{\partial p}{\partial y} + \omega^2 r\frac{\partial r}{\partial y} + 2(\omega_2 u - \omega_1 v) \qquad (4.14)$$

Equations (4.12)-(4.14) and the continuity equation (4.11) form the basis of the present analysis. A closed set of equations in the dependent variables u, v, w and p is obtained if the shear stresses τ_1 and τ_2 are related to the mean velocity field, and the inviscid flow pressure, velocity components, and curvatures are known at the outer edge of the boundary layer.

Inviscid Flow Relations

Outside the boundary layer an inviscid core flow is assumed to exist, thus the relative total pressure remains constant along a streamline, or

$$P_R = p + \rho\frac{U^2}{2} - \rho\frac{\omega^2 r^2}{2} = \text{constant} \qquad (4.15)$$

where U is the relative velocity at the boundary layer edge.

Equation (4.15) may be differentiated to yield an expression for the streamwise pressure gradient

$$-\frac{1}{\rho}\frac{\partial p}{\partial s} = U\frac{\partial U}{\partial s} - \omega^2 r\frac{\partial r}{\partial s} \tag{4.16}$$

Provided the absolute total pressure is uniform across the passage far upstream of the impeller, a similar result is obtained for the pressure gradient normal to the streamlines

$$-\frac{1}{\rho}\frac{\partial p}{\partial n} = U\frac{\partial U}{\partial n} - \omega^2 r\frac{\partial r}{\partial n} \tag{4.17}$$

These relations may be substituted in equations (4.12) and (4.13) when the variation in pressure through the boundary layer is negligible. This criterion is met if (1) the thickness of the layer is small relative to a characteristic length, or (2) the Coriolis and curvature terms of equation (4.14) are negligible.

An additional relation may be derived from the expression for the vorticity of the inviscid core flow

$$\vec{\Omega} = \nabla \times \vec{W} = -2\vec{\omega} \tag{4.18}$$

where $-2\vec{\omega}$ is the relative vorticity resulting from an irrotational absolute flow upstream of the impeller. With

$\vec{W} = \hat{e}_1 W_1 + \hat{e}_2 W_2 + \hat{e}_3 W_3$, the components of the vorticity vector in orthogonal streamline coordinates are

$$\Omega_1 = -2\omega_1 = \frac{\partial W_3}{\partial n} - \frac{1}{h_2}\frac{\partial (h_2 W_2)}{\partial y} \tag{4.19}$$

$$\Omega_2 = -2\omega_2 = \frac{1}{h_1}\frac{\partial (h_1 W_1)}{\partial y} - \frac{\partial W_3}{\partial s} \tag{4.20}$$

$$\Omega_3 = -2\omega_3 = \frac{1}{h_2}\frac{\partial}{\partial s}(h_2 W_2) - \frac{1}{h_1}\frac{\partial (h_1 W_1)}{\partial n} \tag{4.21}$$

Along an inviscid flow streamline, the velocity components W_2 and W_3 are zero, and $W_1 = W = U$. Therefore, equation (4.21) reduces to

$$2\omega_3 = \frac{\partial U}{\partial n} + \frac{U}{h_1}\frac{\partial h_1}{\partial n} \tag{4.22}$$

Recalling the definitions of geodesic curvature, we obtain the following useful relation for K_{12} in terms of the inviscid flow field:

$$K_{12} = \frac{1}{U}\frac{\partial U}{\partial n} - \frac{2\omega_3}{U} \tag{4.23}$$

Hub and Shroud Boundary Layers

The boundary layers which develop on the hub and shroud surfaces of most centrifugal impellers are characterized

by strong secondary flows induced by the blade-to-blade pressure gradient. These secondary flows transport low energy fluid across the passage toward the blade suction surface. An important consequence of this process is a reduction in boundary layer growth as compared to an equivalent two-dimensional flow.

The fluid within the boundary layers is subject to essentially the same transverse pressure gradient as the outer core flow. In the inviscid core this pressure gradient is balanced by centrifugal and Coriolis forces, but inside the boundary layers the magnitude of these forces is diminished because of the defect in streamwise velocity component. As a result, fluid particles within the boundary layer follow a more sharply curved path than those along an outer inviscid flow streamline.

If the n-momentum equation (4.13) is rewritten with the shear stress and streamline divergence terms neglected and using equations (4.17) and (4.23), it can be shown that the driving force for boundary layer crossflow is given by

$$K_{12}(v^2 - u^2) + 2\omega_3(V - u)$$

i.e., the combined effects of centrifugal acceleration due to the curvature of the outer flow streamlines, and the transverse component of the Coriolis acceleration. The

influence of the first term is characterized by a non-dimensional curvature parameter (r_t/R_c), where r_t is the impeller discharge radius and R_c is the local radius of curvature $|1/K_{12}|$ of an inviscid flow streamline projected on the surface. This parameter represents the ratio of the centrifugal acceleration to the convective acceleration in the freestream. Similarly, the rotation parameter $(2\omega_3 r_t/U)$ provides a measure of the importance of Coriolis forces relative to freestream inertial forces. Both parameters are significant in an impeller having an axial inlet and a radial discharge; curvature effects dominate in the axial portion, while rotation effects are strongest in the radial portion. This is illustrated in Fig. 4.2 where the curvature and rotation parameters are plotted for conditions along the hub and shroud of a radial-bladed centrifugal compressor. These parameters provide only an approximate indication of the crossflow intensity, however, since the migration of boundary layer fluid across the passage also depends upon the streamwise boundary layer velocity profile.

Momentum Integral Equations

As stated previously, the hub and shroud boundary layers are expected to remain thin with respect to a characteristic passage dimension because of secondary flow and streamline divergence effects. Hence, the change in pressure through the boundary layer as given by equation (4.14)

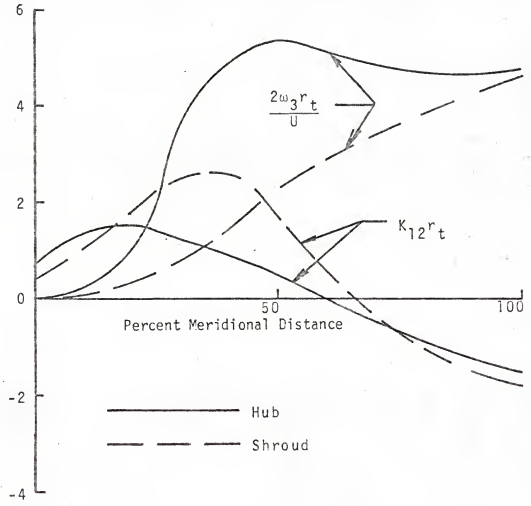

Fig. 4.2. Curvature and Rotation Parameters for the Hub and Shroud of a Radial-Bladed Compressor

will be negligible, and we may assume $\left(\frac{\partial p}{\partial s}\right)_y = \left(\frac{\partial p}{\partial s}\right)_\delta$ as in conventional two-dimensional boundary layer theory. Also, the term containing the streamwise surface curvature K_{13} may be omitted on the grounds that $\delta/R_c << 1$. With these simplifications and the use of equations (4.12) and (4.13), the streamwise and crosswise momentum equations become

s-momentum

$$u\frac{\partial u}{\partial s} + v\frac{\partial u}{\partial n} + w\frac{\partial u}{\partial y} - K_{12}uv + K_{21}v^2 = \frac{1}{U}\frac{\partial U}{\partial s} + 2\omega_3 v + \frac{1}{\rho}\frac{\partial \tau_1}{\partial y} \qquad (4.24)$$

n-momentum

$$u\frac{\partial v}{\partial s} + v\frac{\partial v}{\partial n} + w\frac{\partial v}{\partial y} - K_{21}uv + K_{12}u^2 = \frac{1}{U}\frac{\partial U}{\partial n} - 2\omega_3 u + \frac{1}{\rho}\frac{\partial \tau_2}{\partial y} \qquad (4.25)$$

The procedure employed in deriving the momentum integral form of these equations is similar to that used in the two-dimensional case. An expression for w is obtained through integration of the continuity equation (4.11)

$$w = -\int_0^y \left(\frac{\partial u}{\partial s} - K_{21}u + \frac{\partial v}{\partial n} - K_{12}v\right) dy \qquad (4.26)$$

Next, with equation (4.26) used to eliminate w, the momentum equations are integrated through the boundary layer with the following boundary conditions:

$$u = v = w = 0,\ \tau_1 = (\tau_1)_0,\ \tau_2 = (\tau_2)_0 \quad \text{for } y = 0$$
$$u = U,\ v = 0,\ \tau_1 = \tau_2 = 0 \quad \text{for } y = \delta \tag{4.27}$$

The integral forms of equations (4.24) and (4.25) may be written as

$$U\frac{\partial}{\partial s}\int_0^\delta u\,dy - \frac{\partial}{\partial s}\int_0^\delta u^2 dy = \frac{(\tau_1)_0}{\rho} - \delta U\frac{\partial U}{\partial s} + K_{21}\int_0^\delta (U-u)u\,dy$$
$$+ K_{21}\int_0^\delta v^2 dy - K_{12}\int_0^\delta uv\,dy + K_{12}\int_0^\delta (U-u)v\,dy \tag{4.28}$$
$$+ \frac{\partial}{\partial n}\int_0^\delta uv\,dy - U\frac{\partial}{\partial n}\int_0^\delta v\,dy - 2\omega_3\int_0^\delta v\,dy$$

and

$$\frac{\partial}{\partial n}\int_0^\delta v^2 dy + \frac{\partial}{\partial s}\int_0^\delta uv\,dy - 2K_{21}\int_0^\delta uv\,dy + K_{12}\int_0^\delta u^2 dy$$
$$-K_{12}\int_0^\delta v^2 dy = \delta U\frac{\partial U}{\partial n} - 2\omega_3\int_0^\delta u\,dy - \frac{(\tau_2)_0}{\rho} \tag{4.29}$$

It is convenient to express equations (4.28) and (4.29) in terms of the six three-dimensional boundary layer thickness parameters [17]. The definitions used here are

$$\delta_1^* = \int_0^\delta (1-\frac{u}{U})dy \qquad \delta_2^* = \int_0^\delta \frac{v}{U}dy$$

$$\Theta_{11} = \int_0^\delta (1-\frac{u}{U})\frac{u}{U}dy \qquad \Theta_{21} = \int_0^\delta \frac{uv}{U^2}dy \qquad (4.30)$$

$$\Theta_{12} = \int_0^\delta (1-\frac{u}{U})\frac{v}{U}dy \qquad \Theta_{22} = \int_0^\delta \frac{v^2}{U^2}dy$$

Only five of these thicknesses are independent, however, and it is easily shown that

$$\delta_2^* = \Theta_{12} + \Theta_{21} \quad . \qquad (4.31)$$

Using these definitions and equation (4.23) we obtain the momentum integral equation for the streamwise flow

$$\frac{\partial\Theta_{11}}{\partial s} + \frac{1}{U}\frac{\partial U}{\partial s}(2\Theta_{11}+\delta_1^*) = \frac{(\tau_1)_0}{\rho U^2} - \frac{\partial\Theta_{12}}{\partial n} + K_{21}(\Theta_{11}+\Theta_{22}) - \frac{4\omega_3}{U}\Theta_{12} \qquad (4.32)$$

and similarly, for the crosswise flow we get

$$\frac{\partial\Theta_{22}}{\partial n} + \frac{\partial\Theta_{21}}{\partial s} + 2(\frac{1}{U}\frac{\partial U}{\partial s} - K_{21})\Theta_{21} - K_{12}(\Theta_{11}+\delta_1^*-\Theta_{22}) \qquad (4.33)$$

$$- \frac{2\omega_3}{U}(\delta_1^*-2\Theta_{22}) = - \frac{(\tau_2)_0}{\rho U^2}$$

Equations (4.32) and (4.33) are two coupled, nonlinear partial differential equations which incorporate the effects of secondary flow, streamline curvature, streamline convergence or divergence, and coordinate rotation. When these effects are not present, the above equations reduce to the familiar two-dimensional momentum integral equation, i.e.,

$$\frac{\partial \theta_{11}}{\partial s} + \frac{1}{U}\frac{\partial U}{\partial s}(2\theta_{11}+\delta_1^*) = \frac{(\tau_1)_0}{\rho U^2} \tag{4.34}$$

Before one can attempt a numerical solution of equations (4.32) and (4.33) for a given external flow field, the following information must be supplied:

1 A parametric representation of the streamwise velocity profile.

2 A shear stress law for the streamwise direction.

3 An additional equation to relate the change in shape of the streamwise profile to the other parameters.

4 A relation for the crosswise shear stress component $(\tau_2)_0$.

5 Some means of relating the crossflow thicknesses, or the crossflow velocity v, to the other parameters of the flow.

Note that the first three requirements also apply to the

calculation of two-dimensional turbulent boundary layers. All five auxiliary relations are critical to the success of any three-dimensional momentum integral scheme, and there is at present no obviously correct choice for any of them.

Crossflow Relations

A typical three-dimensional boundary layer velocity profile resolved into its streamwise and crosswise components is illustrated in Fig. 4.3. The wall shear stress components $(\tau_1)_0$ and $(\tau_2)_0$ are related through the angle between the limiting flow direction at the wall (direction of the resultant wall shear stress) and the direction of an external streamline projected on the wall. The tangent of this angle is defined as [24]

$$\varepsilon \equiv \lim_{y \to 0} \frac{v}{u} = \frac{(\tau_2)_0}{(\tau_1)_0} \tag{4.35}$$

The major advantage gained by replacing $(\tau_2)_0$ with a new unknown ε is its convenient use as a parameter in one of the various crossflow velocity profiles suggested in the literature. Perhaps the best known and most widely used crossflow model is the Prandtl-Mager relation [18]

$$\frac{v}{U} = G\left(\frac{y}{\delta}\right) \cdot g\left(\frac{y}{\delta}\right) \cdot \varepsilon \tag{4.36}$$

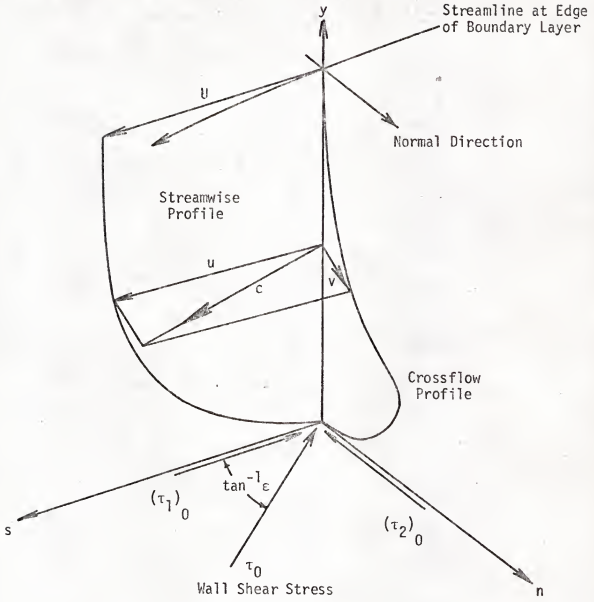

Fig. 4.3. Velocity Profiles and Shear Stress Components

The functions G and g must satisfy the boundary conditions:

$$G = 0, \qquad g = 1 \qquad \text{at } y = 0$$

$$G = 1, \qquad g = 0 \qquad \text{at } y = \delta \ .$$

Mager used $g = (1-y/\delta)^2$ and $G = u/U$ with a power law approximation for the streamwise velocity profile. He obtained good agreement when comparing this model with experimental data for flow in a stationary curved duct. This approach also gave good results for turbulent flow over a rotating disk [60].

There have been several other relations proposed for the crossflow profile, but the experimentally verified triangular model of Johnston [24] is probably the most firmly based. However, it is somewhat more complex than equation (4.36) since an additional parameter is required. In this model the boundary layer is divided into two regions. Near the wall the crossflow velocity is given by

$$\frac{v}{U} = \epsilon \frac{u}{U}$$

and in the outer region by

$$\frac{v}{U} = A\left(1 - \frac{u}{U}\right) \ .$$

The new parameter A is assumed to be a function of the total angle through which the main flow has been turned from an initially collateral flow condition. It should be noted that neither of the crossflow models mentioned above can handle reversals in flow direction (s-shape), but this situation is not expected in the hub and shroud boundary layers.

A polar plot (hodograph) showing typical crossflow profiles predicted by equation (4.36) and also by the triangular model is given in Fig. 4.4 The plot indicates, as pointed out in reference [19], that the two crossflow representations can actually produce quite similar results. Therefore, it is reasonable to use equation (4.36) and avoid the additional complexity of the two-parameter model, and also the uncertainty associated with A in a flow subject to centrifugal and Coriolis forces.

The expressions for the crossflow thickness given by equations (4.30) may now be simplified using equation (4.36) to give

$$\Theta_{12} = \delta\varepsilon \int_0^1 (1-\frac{u}{U})\frac{u}{U}(1-\eta)^2 d\eta = I_{12}\delta\varepsilon$$

$$\Theta_{21} = \delta\varepsilon \int_0^1 (\frac{u}{U})^2 (1-\eta)^2 d\eta = I_{21}\delta\varepsilon \qquad (4.37)$$

$$\Theta_{22} = \delta\varepsilon^2 \int_0^1 (\frac{u}{U})^2 (1-\eta)^4 d\eta = I_{22}\delta\varepsilon^2$$

continued

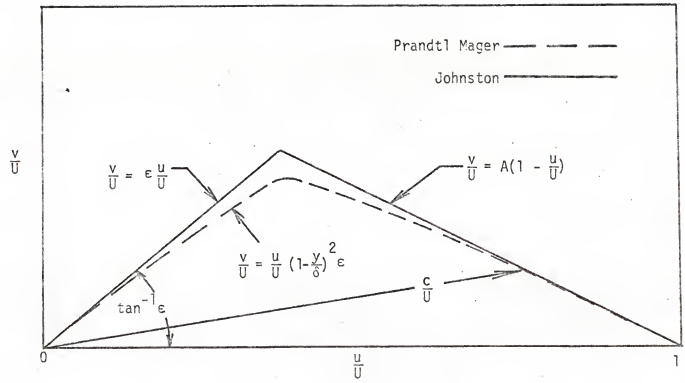

Fig. 4.4. Comparison of Crossflow Models

$$\delta_2^* = \delta\varepsilon \int_0^1 \frac{u}{U}(1-\eta)^2 d\eta = I_2 \delta\varepsilon$$

As a result, the crossflow terms appearing in the momentum integral equations now depend only on ε, the boundary layer thickness δ, and the integral terms denoted by I. The integral terms are easily evaluated from the streamwise velocity profile.

Streamwise Formulation

Several investigators [18, 23, 61, 62] have found that the streamwise velocity profile and shear stress in a three-dimensional turbulent boundary layer are adequately represented by two-dimensional relations. Provided the added three-dimensional terms do not greatly outweigh the parameters governing two-dimensional boundary layer development, a reasonably accurate prediction of local streamwise properties may be obtained using existing methods. Based on this premise, a well-established two-dimensional turbulent boundary layer technique, Moses [63], was selected as the starting point for calculation of the streamwise flow. This method, which is described in Appendix B, was used successfully by Moore [46] to compute three-dimensional boundary layer growth in a rotating rectangular diffuser.

By assuming that the crossflow thickness Θ_{12} is nearly constant in the blade-to-blade or crosswise

direction,† one may eliminate the derivative $\frac{\partial \Theta_{12}}{\partial n}$ from the streamwise momentum integral equation (4.32). However, the magnitude of Θ_{12} may still be appreciable, so the last term in this equation must be retained. With the above simplification, the form of equation (4.32) valid for the hub and shroud surfaces away from the blades is

$$\frac{\partial \Theta_{11}}{\partial s} + \frac{1}{U}\frac{\partial U}{\partial s}(2\Theta_{11}+\delta_1^*) = \frac{(\tau_1)_0}{\rho U^2} + K_{21}(\Theta_{11}+\Theta_{22}) - \frac{4\omega_3}{U}\Theta_{12}. \quad (4.38)$$

The last three terms in this equation are negative for a diverging passage with secondary flow directed towards the blade suction surface. Thus, even in a strong adverse pressure gradient, the hub and shroud boundary layers should remain thin relative to the suction surface boundary layer. This behavior is partially substantiated by the rotating duct experiments of reference [49], where a decrease in end-wall boundary layer thickness was observed with increasing rotation rate.

To make use of the Moses method, equation (4.38) is written in the form of equation (B.1) of Appendix B with an upper limit of integration n_1, i.e.,

†This assumption is reasonable except near the corner regions (where the hub and shroud surfaces intersect the blades). In these regions the principal changes in the magnitude of the crosswise velocities occur.

$$\left(\frac{u}{U}\right)_{\eta_1} \frac{\partial}{\partial s}\left(R_\delta \int_0^{\eta_1} \frac{u}{U}\, d\eta\right) - \frac{1}{U}\frac{\partial}{\partial s}\left(UR_\delta \int_0^{\eta_1} \left(\frac{u}{U}\right)^2 d\eta\right) = \frac{(\tau_1)_0 - (\tau_1)_{\eta_1}}{\mu U}$$

$$- \eta_1 \frac{R_\delta}{U}\frac{\partial U}{\partial s} + K_{21} R_\delta \left[\left(\frac{u}{U}\right)_{\eta_1} \int_0^{\eta_1} \frac{u}{U} d\eta - \int_0^{\eta_1} \left(\frac{u}{U}\right)^2 d\eta\right] + K_{21} R_\delta (I_{22})_{\eta_1} \varepsilon^2$$

$$- \frac{2\omega_3}{U} R_\delta \left[\left(1 + \left(\frac{u}{U}\right)_{\eta_1}\right)(I_2)_{\eta_1} - 2(I_{21})_{\eta_1}\right]\varepsilon \qquad (4.39)$$

where equations (4.37) have been substituted for the cross-flow integrals. When equation (4.39) is evaluated for $\eta_1 = 0.3$ and $\eta_1 = 1.0$, two ordinary differential equations result for skin friction coefficient and boundary layer thickness Reynolds number R_δ, the two parameters defining the streamwise velocity profile. The equations are solved by stepwise integration along the surface projections of the inviscid flow streamlines adjacent to the hub and shroud. The remaining unknown parameter ε, the tangent of the limiting wall streamline angle, must be determined simultaneously by integration of equation (4.33).

Crosswise Formulation

An approximate solution for the boundary layer crossflow parameter ε may be carried out by integrating

the crosswise momentum integral equation (4.33) either in the streamwise direction (the approach followed by Mager [18], Cumptsy and Head [19], and others), or across the passage in the blade-to-blade direction (as done by Moore [46]). Both approaches require a simplifying assumption to eliminate one of the partial derivatives ($\partial\theta_{22}/\partial n$ or $\partial\theta_{21}/\partial s$) when the external flow is not axisymmetric.†

For integration in the streamwise direction it is customary to assume the crossflow is small and neglect the normal derivative $\partial\theta_{22}/\partial n$ [18, 25]. If this scheme was employed in the hub and shroud boundary layer calculation, the influence of the bounding surfaces (blades) would be lost. In fact, the predicted crossflow would be independent of blade spacing and similar to that for a rotating body of revolution.

The blade-to-blade integration, on the other hand, does account for the crossflow restriction due to the blades by allowing one to specify an initial condition at the pressure surface. Making use of equations (4.35) and (4.37) and assuming that the streamwise derivative ($\partial\theta_{21}/\partial s$) is negligible compared to the crosswise derivative ($\partial\theta_{22}/\partial n$), equation (4.33) becomes

---

†When the outer inviscid flow is axisymmetric ($\partial(\ )/\partial\theta = 0$), the crosswise momentum equation may be transformed into an ordinary differential equation with s as the independent variable.

$$\frac{d\varepsilon}{dn} = \frac{1}{2\delta I_{22}} \left\{ \frac{2\omega_3 \delta_1^*}{U} + K_{12}(\delta_1^* + \Theta_{11}) - \left[\frac{C_f}{2} + 2\left(\frac{1}{U}\frac{\partial U}{\partial s} - K_{21}\right)\delta I_{21} \right] \varepsilon \right.$$

$$\left. - \left[\left(\frac{4\omega_3}{U} + K_{12} \right) \delta I_{22} + \frac{d}{dn}(\delta I_{22}) \right] \varepsilon^2 \right\} \tag{4.40}$$

This ordinary differential equation may be integrated from pressure surface to suction surface along either the hub or the shroud to determine ε at a given streamwise station.

Calculation Procedure

The calculation grid used for the hub and shroud boundary layer analysis is depicted in Fig. 4.5. As stated previously, both the impeller geometry and the inviscid flow field are specified in terms of cylindrical coordinates, while the boundary layer equations are formulated in streamline coordinates. In the latter case, the coordinate system itself changes from one iteration cycle to the next as the streamlines and their orthogonal trajectories shift in position. In order to avoid the construction of a new coordinate grid with each boundary layer solution, meridional coordinates (m, θ, y) based on impeller geometry are used to establish the streamwise calculation grid right at the start.

As shown in Fig. 4.5, the meridional distances along the hub and shroud surfaces are initially divided

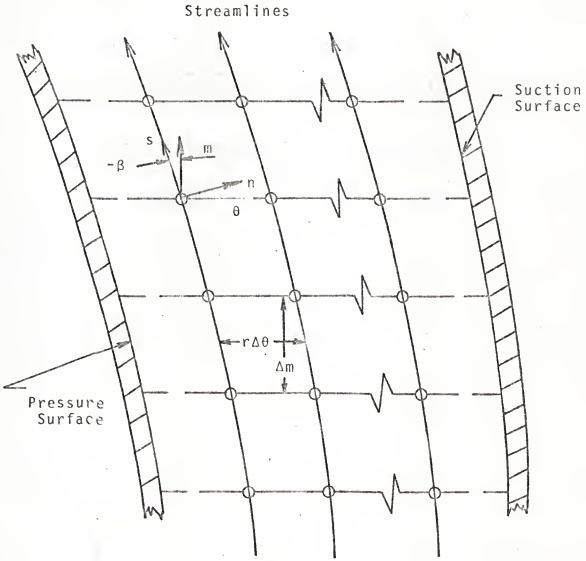

Fig. 4.5. Calculation Grid for Hub and Shroud Boundary Layers

into small increments Δm. Then for each boundary layer calculation cycle, the streamwise step size which is measured along the surface projections of the external streamlines is computed from

$$\Delta s = \frac{\Delta m}{\cos \bar{\beta}}$$

where $\bar{\beta}$ is the average relative flow angle between grid points. All of the inviscid flow parameters needed in the boundary layer solution, including β, are known as a function of m for each of the streamlines adjacent to the surface. The component of angular velocity perpendicular to the hub or shroud surface is given by

$$\omega_3 = \omega \sin\alpha \tag{4.41}$$

where $\alpha = \tan^{-1} \frac{dr}{dz}$. An expression for the geodesic curvature K_{21} is derived in Appendix C, i.e.,

$$K_{21} = -\frac{1}{r} \frac{\partial r}{\partial s} + \tan\beta \frac{\partial \beta}{\partial s} - \frac{1}{r \cos\beta} \frac{\partial \beta}{\partial \theta} \tag{4.42}$$

Using these relations and the modified Moses method, equation (4.39) is integrated along several hub and shroud streamline projections. This calculation is restricted, however, to those streamlines away from the corner regions

(which are treated in a subsequent section) where the approximate flow model is clearly inapplicable.

The approximate form of the crosswise momentum integral equation (4.40) is employed to compute the crossflow parameter distribution at each streamwise step. It may be transformed for integration in the circumferential direction using the following relation among derivatives:

$$\frac{1}{r}\frac{\partial(\ )}{\partial\theta} = \sin\beta\frac{\partial(\ )}{\partial s} + \cos\beta\frac{\partial(\ )}{\partial n} \quad . \tag{4.43}$$

Since streamwise derivatives have been neglected, equation (4.40) now becomes

$$\varepsilon\frac{d\varepsilon}{d\theta} = r\cos\beta\ (a + b\varepsilon + c\varepsilon^2) \tag{4.44}$$

where

$$a = \frac{\frac{2\omega_3\delta_1^*}{U} + K_{12}(\delta_1^* + \Theta_{11})}{2\delta I_{22}}$$

$$b = \frac{\frac{C_{f_1}}{4} + (\frac{1}{U}\frac{\partial U}{\partial s} - K_{21})I_{21}\delta}{I_{22}\delta}$$

$$c = \frac{2\omega_3}{U} + \frac{K_{12}}{2} + \frac{1}{2\delta I_{22}r}\frac{\partial(\delta I_{22})}{\partial\theta}$$

This equation is integrated at each streamwise station (m= constant) from the blade pressure surface corner to just outside the suction surface boundary layer. An initial condition of $\varepsilon = 0$ at the pressure surface is used to start the calculation. The integration is carried out using the analytical solution of equation (4.44) for constant coefficients on several intervals between streamlines, or

$$r\cos\beta(\theta_{K+1}-\theta_K) = \left[\frac{1}{2c}\ln(a+b\varepsilon+c\varepsilon^2) - \frac{b}{2cd}\ln\left(\frac{2c\varepsilon+b-d}{2c\varepsilon+b+d}\right)\right]_{\varepsilon_K}^{\varepsilon_{K+1}}$$

where $d = \sqrt{b^2 - 4ac}$ and the subscripts denote the streamlines at either end of the integration step. This relation is solved by iteration with a, b, c, and β taken as mean values on the interval. All other terms required in the evaluation of a, b, and c are obtained from the streamwise boundary layer solution or the inviscid flow solution. The streamline curvature is computed from an expression derived in Appendix C, i.e.,

$$K_{12} = \frac{\partial\beta}{\partial s} + \frac{\tan\beta}{r}\frac{\partial r}{\partial s} \qquad (4.45)$$

The hub and shroud surface streamlines closest to the blades are not used for the streamwise integration, and it is assumed that boundary layer parameters in the corner regions are the same as those at the adjacent streamlines.

Blade Surface Boundary Layers

The boundary layers formed on the blade surfaces of a typical centrifugal impeller are strongly influenced by three-dimensional effects. These include secondary flows arising within the blade boundary layer which are induced by the hub-to-shroud pressure gradient, and also secondary flows induced by the blade-to-blade pressure gradient which transport low energy fluid to or from the blade boundary layers via the corner regions. The latter effect has been shown to be the major cause for boundary layer separation on the suction surface near the exit of a radial flow impeller [36, 46]. In addition, rotation of the impeller and flow path curvature affect the turbulence structure or stability of the flow and can also cause the pressure gradient normal to the wall to become an important factor.

In the discussion on the hub and shroud boundary layers it was pointed out that the crossflow intensity in the blade-to-blade direction is roughly proportional to the sum of the non-dimensional curvature and rotation parameters. Since the same crosswise momentum equation applies to the blade boundary layers as well, these parameters are also indicative of the degree of boundary layer crossflow occurring on the blades as a result of the hub-to-shroud pressure gradient. Fig. 4.6 shows how curvature parameter (r_t/R_c) and rotation parameter $(2\omega_3 r_t/U)$ vary along the

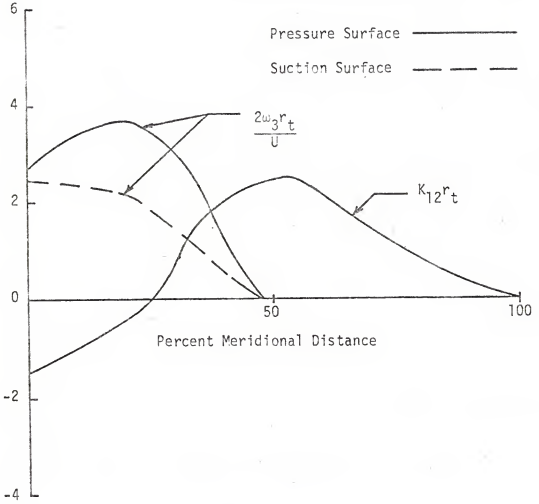

Fig. 4.6. Curvature and Rotation Parameters for the Blade Surfaces of a Radial-Bladed Compressor

pressure and suction surfaces of a radial-bladed impeller (the same configuration used to obtain Fig. 4.2). Note that for the blades, the rotation or Coriolis effects are strongest where the flow is primarily axial, while curvature effects dominate near the middle of the flow path where the flow is turned from axial to radial. For an impeller designed with other than radial blading, e.g., swept-back blades, one would expect the rotation parameter to drop off more slowly with streamwise distance, and the curvature parameter to have a lower maximum value.

Simplifying Assumptions

The boundary layers formed on the hub, shroud, and blade surfaces of an impeller cannot be independent of one another. On the contrary, they are strongly coupled through both their interaction with the inviscid flow field, and the migration of low energy fluid (crossflow) from one bounding surface to another by way of the corner regions. It is also apparent that the crossflows generated on the blade surfaces by the hub-to-shroud pressure gradient and the crossflows generated on the hub and shroud by the blade-to-blade pressure gradient must interact in a very complex manner. This is especially true in the corners where our knowledge of the flow is most inadequate.

In view of the complicated and unresolved nature of the blade surface boundary layers in a three-dimensional

impeller passage, a detailed flow analysis is impractical if not impossible at present. Instead, an approximate model is employed in which crossflows resulting from the hub-to-shroud pressure gradient are neglected, and the blade-to-blade pressure gradient is assumed to be the only source of secondary flow. Clearly, the validity of this model is most questionable near the leading edge and in the axial portion of the impeller. However, the crossflow development would be inhibited near the inlet since the blade boundary layers have not had much opportunity to thicken (unless separation occurs). This approach is further justified by comparing Figs. 4.2 and 4.6. For this particular impeller, the effective driving force for boundary layer crossflow is significantly larger for the hub and shroud than for the blades over most of the flow path. This trend is even more pronounced for impeller designs of the "pressure balanced" type [64], where the hub-to-shroud pressure gradient is minimized by an appropriate selection of the meridional curvature and blade angle distributions.

One must still account for the influx or efflux of boundary layer fluid through the corner regions. The crossflow magnitude entering or leaving the blade boundary layers can be determined using the crossflow computed for the hub and shroud streamlines nearest the pressure and suction surfaces. A model proposed by Moore [46] which assumes

streamwise momentum is conserved in the corners is used to relate the distribution of the crosswise velocity component in the blade boundary layer to the distribution in the hub or shroud boundary layer.

Once again the streamwise flow is assumed to be adequately represented by two-dimensional boundary layer velocity profile and shear stress relations (modification of the turbulence structure is accounted for, however, through empirical correction of the eddy viscosity). The Moses method (Appendix B) provides these relations, and in the present analysis it is extended to take into account the extra effects of crossflow, rotation, and streamline curvature.

Finally, as an alternative to computing the boundary layer characteristics along several streamlines adjacent to the blades, it is assumed that the blade boundary layer properties which describe the streamwise flow are uniform in the hub-to-shroud direction along a streamline normal (reasonable for small aspect ratios, i.e., (blade height)/(passage width), and small hub-to-shroud velocity gradients). The pressure and suction surface boundary layers are calculated using the inviscid flow input and surface geometry corresponding to a streamline near the mid-blade height. To simplify the governing equations, the boundary layer flow at this location is treated as being collateral (v=0).

In other words, it is considered a plane of symmetry flow with an allowance for either convergent or divergent crossflows, i.e., although crosswise velocities are zero, transverse derivatives arising from crossflow through the corner regions may be non-zero.

Momentum Integral Formulation

With the transverse velocity component assumed negligible, the streamline momentum equation (4.12) becomes

$$u\frac{\partial u}{\partial s} + w\frac{\partial u}{\partial y} - K_{13}uw = -\frac{1}{\rho}\frac{\partial p}{\partial s} - \omega^2 r\frac{\partial r}{\partial s} - 2\omega_2 w + \frac{1}{\rho}\frac{\partial \tau_1}{\partial y} \qquad (4.46)$$

and the continuity equation (4.11) reduces to

$$\frac{\partial u}{\partial s} - K_{21}u + \frac{\partial v}{\partial n} + \frac{\partial w}{\partial y} = 0 \qquad (4.47)$$

The Coriolis acceleration component normal to the wall ($-2\omega_2 u$) and the blade surface curvature (K_{13}) often become important in the radial portion of an impeller; consequently, the usual assumption that $\frac{\partial p}{\partial y} = 0$ is unreasonable. When pressure derivatives normal to the blade surface reach an order of magnitude unity, the pressure change through the layer becomes of order δ. Therefore, when the boundary layer thickness is large compared to the passage dimensions, as is expected on the suction surface near the exit, one

must use the y-momentum equation (4.14) to determine the local streamwise pressure gradient $(\frac{\partial p}{\partial s})_y$. Equation (4.14) may be written as

$$-\frac{1}{\rho}\frac{\partial p^*}{\partial y} = K_{13}u^2 - 2\omega_2 u \tag{4.48}$$

where p* is the reduced static pressure defined as

$$p^* = p - \frac{1}{2}\omega^2 r^2 \tag{4.49}$$

An expression for the streamwise pressure gradient within the boundary layer is obtained by first differentiating equation (4.48) with respect to s (the surface curvature is assumed to vary slowly so that derivatives of K_{13} and ω_2 may be neglected), or

$$-\frac{1}{\rho}\frac{\partial^2 p^*}{\partial y \partial s} = K_{13}\frac{\partial u^2}{\partial s} - 2\omega_2 \frac{\partial u}{\partial s}$$

Then integrating through the layer to y=δ and employing equation (4.16) to eliminate the freestream pressure gradient gives

$$-\frac{1}{\rho}\left(\frac{\partial p^*}{\partial s}\right)_y = U\frac{\partial U}{\partial s} + 2\omega_2 \int_y^\delta \frac{\partial u}{\partial s}dy - K_{13}\int_y^\delta \frac{\partial u^2}{\partial s}dy \tag{4.50}$$

A momentum integral equation for the streamwise flow may be derived from equation (4.46) by substituting equation (4.50) for $(\frac{\partial p^*}{\partial s})_y$ and then using the continuity equation (4.47) to eliminate w. When the resulting expression is integrated through the boundary layer to a height $h \leq \delta$, we obtain

$$(u)_h \int_0^h \frac{\partial u}{\partial s}\,dy - \int_0^h \frac{\partial u^2}{\partial s}\,dy = \frac{(\tau_1)_0 - (\tau_1)_h}{\rho} - hU\frac{\partial U}{\partial s}$$

$$- K_{21}\left[\int_0^h u^2 dy - (u)_h \int_0^h u dy\right] - \int_0^h \left(\frac{\partial u}{\partial y}\frac{\partial}{\partial n}\int_0^y v dy\right) dy \qquad (4.51)$$

$$- K_{13}\int_0^h \left[u\int_0^y \left(\frac{\partial u}{\partial s} - K_{21}u + \frac{\partial v}{\partial n}\right)dy + \int_y^\delta \frac{\partial u^2}{\partial s}dy\right] dy$$

$$+ 2\omega_2 \int_0^h \left[\int_0^y \left(\frac{\partial u}{\partial s} - K_{21}u + \frac{\partial v}{\partial n}\right)dy + \int_y^\delta \frac{\partial u}{\partial s}dy\right] dy$$

Equation (4.51) consists of the usual two-dimensional momentum integral equation plus four additional terms arising from (i) streamline convergence or divergence (K_{21}), (ii) momentum transport resulting from crossflow into or out of

the blade boundary layers, (iii) streamline curvature in the s-y plane (K_{13}), and (iv) the components of Coriolis acceleration normal to the wall ($-2\omega_2 u$) and in the streamwise direction ($2\omega_2 w$). To make use of the Moses method, it is necessary to express these extra terms as functions of the parameters A and R_δ.

The last term of equation (4.51) (the term resulting from Coriolis effects) may be simplified by noting that

$$\int_0^y \frac{\partial u}{\partial s}\,dy + \int_y^\delta \frac{\partial u}{\partial s}\,dy = \int_0^\delta \frac{\partial u}{\partial s}\,dy = \delta\frac{\partial U}{\partial s} - \frac{\partial}{\partial s}\left(U\delta_1^*\right)$$

It is more difficult to obtain a simple expression for the next to the last term (the curvature term) because velocity appears squared. However, since blade curvature effects are normally of minor importance compared to Coriolis effects (a ratio of 25% at most [65]), an approximate method is used to account for them here. First, we may write

$$\int_y^\delta \frac{\partial u^2}{\partial s}\,dy = \frac{\partial}{\partial s}\int_y^\delta u^2 dy - U^2\frac{\partial \delta}{\partial s} = \frac{\partial}{\partial s}\left[U^2(\delta-\delta_1^*-\theta_{11})\right]$$

$$- U^2\frac{\partial \delta}{\partial s} - \frac{\partial}{\partial s}\int_0^y u^2 dy$$

Now, assuming we can represent the streamwise velocity

profile by a power-law profile

$$\frac{u}{U} = \left(\frac{y}{\delta}\right)^{\frac{1}{n}}$$

with $n=2/(H-1)$ and derivatives of H neglected, we obtain

$$u\int_0^y \frac{\partial u}{\partial s}dy = U\eta^H\left[\frac{1-H}{1+H}\frac{\partial(U\delta)}{\partial s} + \delta\frac{\partial U}{\partial s}\right]$$

and

$$\frac{\partial}{\partial s}\int_0^y u^2dy = \frac{U\eta^H(1+H)}{H}\left[\frac{1-H}{1+H}\frac{\partial(U\delta)}{\partial s} + \delta\frac{\partial U}{\partial s}\right]$$

In addition, we have

$$K_{12}u\int_0^y udy = \frac{2K_{12}U^2\delta\eta^H}{1+H}$$

and

$$u\int_0^y \frac{\partial v}{\partial n}dy = U\delta\eta^{\frac{H-1}{2}}\frac{\partial}{\partial n}\int_0^y vdy$$

The preceding expressions are now substituted into equation (4.51) which, after further manipulation, is rewritten in the same format as equation (B.1) to give

$$\left(\frac{u}{U}\right)_{\eta_1}\frac{\partial}{\partial s}\left(R_\delta\int_0^{\eta_1}\frac{u}{U}d\eta\right) - \frac{1}{U}\frac{\partial}{\partial s}\left(UR_\delta\int_0^{\eta_1}\left(\frac{u}{U}\right)^2 d\eta\right)$$

$$= \frac{(\tau_1)_0 - (\tau_1)_{\eta_1}}{\mu U} - \eta_1\frac{R_\delta}{U}\frac{\partial U}{\partial s} - K_{21}R_\delta\left[\int_0^{\eta_1}\left(\frac{u}{U}\right)^2 d\eta - \left(\frac{u}{U}\right)_{\eta_1}\int_0^{\eta_1}\frac{u}{U}d\eta\right]$$

$$- \int_0^{\eta_1}\left\{\frac{\partial}{\partial\eta}\left(\frac{u}{U}\right)\cdot\frac{\partial}{\partial n}\left(R_\delta\int_0^{\eta}\frac{v}{U}d\eta\right)\right\}d\eta + K_{13}\delta\left[\eta_1\left\{2\frac{R_\delta}{U}\frac{\partial U}{\partial s}\right.\right.$$

$$\left.\left. - \frac{H+1}{H}\left(\frac{\partial R_\delta^*}{\partial s} + \frac{R_\delta^*}{U}\frac{\partial U}{\partial s}\right)\right\} - \frac{R_\delta\eta_1^{H+1}}{H(H+1)}\left(\frac{1}{U}\frac{\partial U}{\partial s} - \frac{H-1}{H+1}\frac{1}{R_\delta}\frac{\partial R_\delta}{\partial s}\right)\right.$$

$$\left. - \frac{2K_{21}R_\delta\eta^{H+1}}{(H+1)^2} + \int_0^{\eta_1}\left\{\left(\frac{u}{U}\right)\cdot\frac{\partial}{\partial n}\left(R_\delta\int_0^{\eta}\frac{v}{U}d\eta\right)\right\}d\eta\right] + \frac{2\omega_2\delta}{U}\left[\eta_1\left(\delta\frac{\partial U}{\partial s} - \frac{\partial R_\delta^*}{\partial s}\right)\right.$$

$$\left. + K_{21}R_\delta\left(\int_0^{\eta_1}\eta\frac{u}{U}d\eta - \eta_1\int_0^{\eta_1}\frac{u}{U}d\eta\right) + \int_0^{\eta_1}\frac{\partial}{\partial n}\left(R_\delta\int_0^{\eta}\frac{v}{U}d\eta\right)d\eta\right] \qquad (4.52)$$

This is an approximate form of the streamwise momentum integral equation which is used to predict the turbulent boundary layer development along the blade surfaces.

Corner Flow

As has been noted, the flow in the corner regions is poorly understood, even qualitatively. Besides the boundary layer concept being questionable in the corners, it is also

quite likely that the separate streamline coordinate systems employed for the blades and for the hub or shroud would not be compatible here. Rather than attempting an in depth flow analysis of this region, Moore's [46] approximate model is used to estimate the crosswise velocity distribution in the blade boundary layers near the hub and shroud corners.

A typical corner region (the hub-pressure surface corner) is shown schematically in Fig. 4.7. Note that although a 90-degree turn is pictured here, the corner model is applicable to most other configurations of interest as well. In Moore's model it is assumed that (1) for a given corner cross-section (the plane area bounded by the hub surface, the blade surface, and the intersection of their respective boundary layers as shown in Fig. 4.7), the same amount of fluid leaves the corner as enters, or

$$\int_0^{\delta_h} v_h dy_h = \int_0^{\delta_b} v_b dy_b$$

and (2) that the streamwise momentum of a fluid particle is conserved in passing through the corner, or in other words, the particle will have the same streamwise velocity component (u) leaving as it did entering. Note that the second assumption is less critical than the first in that it merely relates the crosswise velocity distribution v(y) leaving the corner to that entering.

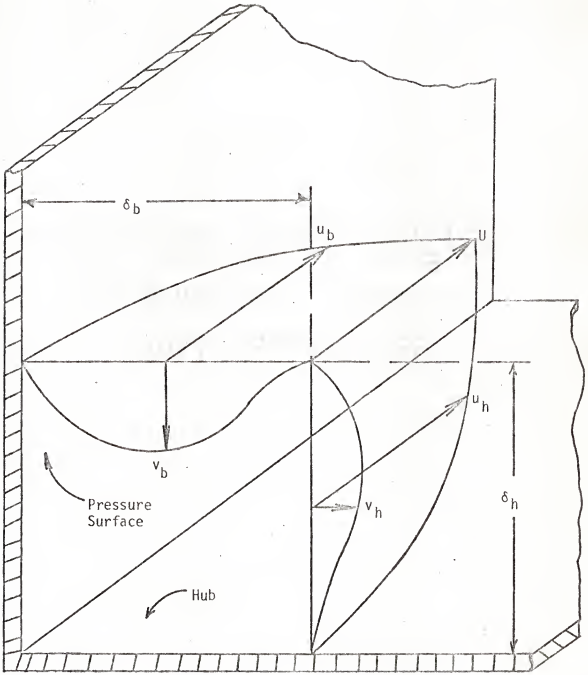

Fig. 4.7. Corner Region

Since the crossflow mass is constant by the first assumption, we may write

$$v_b dy_b = v_h dy_h .$$

Also, according to the second assumption the distance (dy_b) between two fluid particles entering the corner is related to the distance (dy_h) between two particles leaving the corner through

$$dy_b = dy_h \frac{(\frac{\partial u}{\partial y})_b}{(\frac{\partial u}{\partial y})_h} .$$

Combining these expressions and noting that the two streamwise velocity profiles (hub and blade) have the same free-stream velocity U, we obtain the following relation for the crosswise velocity component in the blade boundary layer in terms of the hub or shroud crossflow distribution and the boundary layer properties on either side of the corner region:

$$(\frac{v}{U})_b = (\frac{v}{U})_{h,s} \frac{\frac{\partial(\frac{u}{U})_b}{\partial \eta}}{\frac{\partial(\frac{u}{U})_{h,s}}{\partial \eta}} \frac{\delta_{h,s}}{\delta_b} \qquad (4.53)$$

Wake Flow

It is a well known fact that most centrifugal impellers contain a region of separated flow at the discharge and adjacent to the blade suction surface. Primarily, this results from the migration of boundary layer fluid from the hub, shroud, and pressure surfaces to the suction side of the passage. As pointed out by Dean [28], when separation occurs in the radial portion of an impeller the wake flow does not mix with the core flow to any extent. This is because the Coriolis forces present act to keep the high energy core flow separate from the low energy wake flow. Furthermore, no backflow is observed in the wake flow which continues to develop after the separation point since the blade-to-blade pressure gradient responsible for boundary layer migration is in effect over most of the passage length.

An approximate equation relating the growth of the wake to the main flow characteristics and the crossflow through the corner regions is obtained by integrating the continuity equation (4.47) through the boundary layer

$$\int_0^\delta \frac{\partial u}{\partial s} dy - K_{21} \int_0^\delta u dy + \int_0^\delta \frac{\partial v}{\partial n} dy + \int_0^\delta \frac{\partial w}{\partial y} dy = 0$$

and employing the following boundary conditions:

$$u = U, \quad v = 0, \quad w = w_\delta \qquad \text{at } y = \delta$$

$$u = v = w = 0 \qquad \text{at } y = 0$$

Then, using the definitions given by equations (4.30) we get

$$\frac{\partial}{\partial s}(\delta - \delta_1^*) + \frac{1}{U}\frac{\partial U}{\partial s}(\delta - \delta_1^*) - K_{21}(\delta - \delta_1^*)$$

$$+\frac{1}{U}\frac{\partial(U\delta_2^*)}{\partial n} = \frac{1}{U}\left\{U\frac{\partial \delta}{\partial s} - W_\delta\right\}$$

Note that the rate at which the wake region grows due to freestream fluid entering (entrainment rate) is given by the bracketed term on the right-hand side. Since little mixing is expected at the interface between the wake and core flow, this term is assumed negligible and the preceding equation becomes

$$\frac{\partial}{\partial s}(\delta - \delta_1^*) + \left(\frac{1}{U}\frac{\partial U}{\partial s} - K_{21}\right)(\delta - \delta_1^*) + \frac{1}{U}\frac{\partial}{\partial n}(U\delta_2^*) = 0 \qquad (4.54)$$

Moore [46] found that the measured velocity profiles in the wake region of his rotating rectangular diffuser were represented reasonably well by the following relation:

$$\frac{u}{U} = 3\eta^2 - 2\eta^3 \qquad (4.55)$$

For this profile we have $\delta = 2\delta_1^*$, and equation (4.54) reduces to

$$\frac{\partial \delta}{\partial s} + \left(\frac{1}{U}\frac{\partial U}{\partial s} - K_{21}\right)\delta = -\frac{2}{U}\frac{\partial (U\delta_2^*)}{\partial n} \qquad (4.56)$$

This equation is used to determine the suction surface wake development when separation occurs in the radial part of the impeller.

Curvature and Rotation Effects on Turbulence

The same nonconservative body force terms (curvature and rotation) that affect the normal pressure gradient in the blade boundary layers also have a significant influence on their turbulence structure and stability.† Reference [54] presents a detailed discussion of the effects of longitudinal surface curvature on turbulent shear layers, while references [52] and [53] are concerned mainly with the analogous Coriolis effects in rotating passages. In the present analysis, the results of these investigations are used in an attempt to account for a modification of the local turbulent shear stress caused by these effects.

†The boundary layer on a concave surface or on the pressure side of an impeller passage is unstable in the sense that turbulent fluctuations perpendicular to the surface are increased. In contrast, turbulence is suppressed in the stable boundary layer on a convex surface or on the suction side.

A measure of the importance of surface curvature and rotation is the Richardson number which represents the ratio of the nonconservative body forces to inertia forces in the boundary layer. When this ratio is small ($\leq .25$), the Richardson number for curvature is approximately

$$R_{i_{curv}} = \pm \frac{\frac{2u}{R_c}}{\frac{\partial u}{\partial y}} \tag{4.57}$$

and the corresponding parameter for rotation is approximately

$$R_{i_{rot}} = \frac{-2\omega_2}{\frac{\partial u}{\partial y}} \tag{4.58}$$

It follows that the combined effects of curvature and rotation are represented to the first order by

$$R_{i_{total}} = \frac{-2[\omega_2 \pm \frac{u}{R_c}]}{\frac{\partial u}{\partial y}} \tag{4.59}$$

When $R_i > 0$ turbulent shear stresses are increased over the no rotation, no curvature situation, and when $R_i < 0$ they are reduced.

A simple means of accounting for these effects on shear stress in the present method is through mixing length

$$\ell \equiv \frac{\sqrt{\frac{\tau}{\rho}}}{\frac{\partial u}{\partial y}} \quad .$$

Reference [54] suggests a correction of the form

$$\frac{\ell}{\ell_0} = 1 - k\, R_{i_{total}} \tag{4.60}$$

where the zero subscript denotes conditions at $R_i = 0$. However, the appropriate value for the coefficient k has not been firmly established. Most experimental data indicate a range from 2 to 6. To apply this correction to the Moses method (Appendix B) we simply rewrite equation (4.60) as

$$\frac{\tau}{\tau_0} = \left(1 - k\, R_{i_{total}}\right)^2 \tag{4.61}$$

where τ_0 is the shear stress at η=0.3 given by equation (B.2) and R_i is evaluated at η=0.3. A similar approach has been employed for a curved nonrotating diffuser [66] and fairly good results were obtained.

Calculation Procedure

A sketch of the calculation grid used for the blade boundary layers is presented in Fig. 4.8 where the pressure or suction surface is shown projected onto the

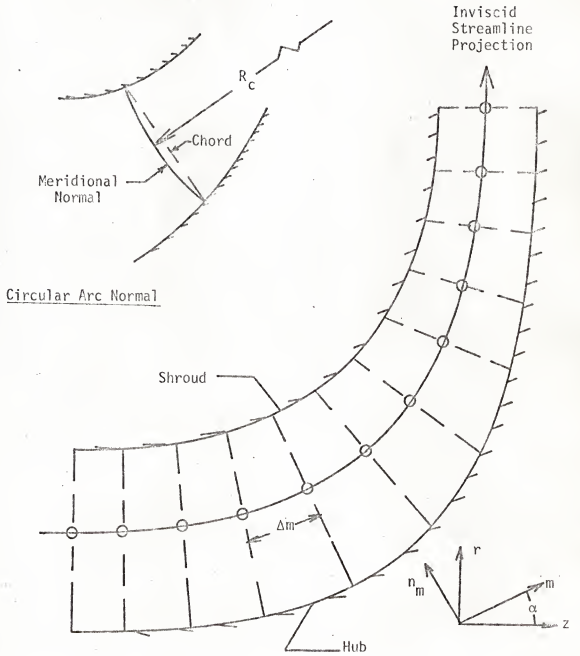

Fig. 4.8. Calculation Grid for Blade Surface Boundary Layers

meridional plane. The calculation proceeds along the surface projection of a streamline just outside the boundary layer near mid-blade height. Along this streamline, the local step size is determined by the blade angle β_b and the increment in meridional distance Δm between the dashed lines representing the chords of circular arc normals to the hub and shroud contours. In the corners of the passage, each of the normals intersects the lines corresponding to constant meridional distance along the hub and shroud. Thus, a streamwise station for all of the impeller surfaces is defined by a conic surface cutting through the passage. This is similar to the inviscid flow calculation grid, except that here the slope of a conic surface is equal to that of a chord rather than being arbitrary.

To begin the calculation, the blade boundary layers are either assumed turbulent from the leading edge, or an initially laminar flow is considered (see Chapter V). When the flow is turbulent, equation (4.52) is integrated step-by-step along the blades using a modified form of the Moses method (Appendix B). One integration step is completed for the boundary layers on all four surfaces before continuing downstream, and at the same time, the secondary flows through the corner regions are evaluated using the corner model described previously.

The crosswise velocity profile $v_b(y)/U$ on the blade surface near the hub or shroud is found from equation (4.53). This is accomplished using the properties (A, R_δ) of the hub or shroud boundary layer along a streamline near the blade, the properties of the blade boundary layer (assumed constant along a hub-to-shroud normal), and the crosswise velocity distribution in the hub or shroud boundary layer near the blade which is given by equation (4.36). Note that using the same values for A and R_δ at either end of a hub-to-shroud normal does not affect the magnitude of the secondary flow entering or leaving the blade boundary layer, but only the distribution of the crosswise velocity component in the blade boundary layer at the corner.

The streamwise momentum integral equation (4.52) contains several terms of the form

$$\int_0^{\eta_1} \phi \cdot \frac{\partial}{\partial \eta} \left(R_\delta \int_0^{\eta} \frac{v}{U} d\eta \right) d\eta$$

where $\phi = 1$, u/U, $\frac{\partial}{\partial \eta}(u/U)$. With the crosswise velocity distribution known near either end of a hub-to-shroud normal, and assuming the blade boundary layer thickness is constant along the normal, the transverse derivative may be approximated as follows:

$$\frac{\partial}{\partial n}\left(R_\delta \int_0^\eta \frac{v}{U} d\eta\right) \approx \frac{\delta_b}{\nu} \frac{\left\{\left(U_c \int_0^\eta \frac{v}{U} d\eta\right)_{shroud} - \left(U_c \int_0^\eta \frac{v}{U} d\eta\right)_{hub}\right\}}{\Delta n}$$

where U_c is the inviscid flow velocity at the intersection of the two boundary layers which meet at the corner, and Δn is the distance between the hub and shroud boundary layers measured along the normal.

The geodesic curvatures (K_{13} and K_{21}) and the angular velocity component ω_2 which appear in equation (4.52) are functions of the blade surface geometry and the inviscid streamline geometry. In general, these terms will vary along the blade surface in both the streamwise and hub-to-shroud directions. But since the blade boundary layer analysis is essentially lumped in the hub-to-shroud direction, the surface curvatures and the angular velocity component should represent average conditions along a normal.

The surface curvature in the s-y plane K_{13} is approximated by neglecting variations in θ along a hub-to-shroud normal. This leads to the same expression as was given earlier for K_{12} on the hub or shroud surfaces, i.e., equation (4.45) which is evaluated along the streamline projection shown in Fig. 4.9. It should be noted, however, that this effect is only included in the primarily radial part of the impeller to account for swept-back blading, and in this region θ is usually constant along a normal.

The streamline convergence or divergence K_{21} is assumed to be equal to the reciprocal of the local radius of a circular arc normal to the hub and shroud surfaces. This is also equivalent to the change in meridional angle along the normal, or

$$K_{21} = \pm \frac{1}{R_c} = \frac{\partial \alpha}{\partial n} . \tag{4.62}$$

The magnitudes of the three angular velocity components (ω_1, ω_2, ω_3) are usually more difficult to determine for the blade surfaces than for the hub and shroud because the normal to the surface may twist considerably along a streamline projection. To obtain the component ω_2 in the direction of a hub-to-shroud normal, the following relation is employed:

$$\omega_2 = \cos\gamma_2 \tag{4.63}$$

where $\cos\gamma_2$ is the direction cosine between the z-axis and the projection of the straight-line chord of a meridional normal onto the mean blade surface. Using the coordinates (r, θ, z) corresponding to the mean blade shape where the projected line segment intersects the hub and the shroud, we get

$$\cos\gamma_2 = \frac{(z_s - z_h)}{\sqrt{r_s^2 - 2r_h r_s \cos(\theta_s - \theta_h) + r_h^2 + (z_s - z_h)^2}} \quad . \qquad (4.64)$$

Although the other components are not required here, they are readily found when ω_2 and the flow angles are known. The streamwise component is given by $\omega_1 = \omega\cos\gamma_1$, where $\cos\gamma_1 = \cos\alpha\cos\beta$, and it follows that

$$\cos\gamma_3 = \sqrt{1 - \cos^2\gamma_1 - \cos^2\gamma_2} \quad .$$

Before the Moses method can be used to integrate equation (4.52), the coefficients (F_{i1}, F_{i2}) in equation (B.3) of Appendix B must be modified to account for any extra terms containing streamwise derivatives of A or R_δ. All other new terms are added to the functions denoted by G_i in equation (B.3). This includes the correction to turbulent shear stress at $\eta = 0.3$ for rotation and curvature effects which is given by equation (4.61).

Finally, if separation of the suction surface boundary layer should occur in the radial portion of the impeller, equation (4.56) is used to compute the subsequent growth of the wake due to secondary flow through the corner regions. The transverse derivative in this expression is evaluated using the same approximation that was used to compute similar terms in equation (4.52).

CHAPTER V

COMBINED FLOW ANALYSIS

Introduction

A complete analysis program for the internal flow characteristics of shrouded centrifugal impellers is developed by combining the separate inviscid core flow and boundary layer analysis procedures described in Chapters III and IV. The objectives of this chapter are to explain how the two calculation schemes are tied together and how they interact; to describe the additional theory and numerical techniques employed to successfully integrate them; and finally, to provide a general outline of the overall analysis procedure.

Because of the complicated geometric configuration of the typical centrifugal impeller passage, it is rarely possible to compute the simultaneous development of the core flow and boundary layers as is commonly done in diffuser analyses. Even in the case of an impeller with simple geometry, the strong interaction between the core flow pressure gradient and the suction surface boundary layer near the impeller exit prohibits this approach. Equally

important, the elliptic nature of the governing partial differential equations is lost completely when an attempt is made to solve both the inviscid and boundary layer equations by a step-by-step marching technique.

The basic approach used here consists of reducing the impeller passage area in the mainstream direction by an amount corresponding to the local displacement of the inviscid core flow streamlines by the boundary layer (i.e., an amount equal to the displacement thickness). Since the individual calculation methods are strongly coupled, several iterations between the two procedures are required to achieve a solution which is everywhere compatible.

Besides the three-dimensional turbulent boundary layer analysis for the impeller hub, shroud, and blade surfaces, other calculations are required to account for viscous effects in the region upstream of the impeller, at the impeller discharge, and in the vaneless diffuser. Also, in certain applications laminar flow is present to a sufficient extent near the blade leading edge that it must be considered in the analysis. These supplementary calculation schemes, which in addition to the methods of Chapters III and IV form the elements of the integrated computer program, are discussed in the following sections.

Upstream Flow

The inviscid core flow calculation procedure for the region upstream of the impeller is essentially the same as described in Chapter III. However, the three-dimensional turbulent boundary layer analysis outlined in Chapter IV pertains only to the impeller surfaces, and additional computations are required to predict the hub and shroud boundary layer development in the inlet region.

Furthermore, it is not always reasonable, although the option is available, to assume that the flow is initially turbulent at the blade leading edge. Consequently, a laminar boundary layer analysis is needed to provide initial conditions for the method of Chapter IV.

Laminar Boundary Layer Calculation

The region of laminar flow which begins at the blade leading edge will usually be of small extent because of the large Reynolds numbers encountered in turbomachinery, and thus should have negligible effect on the external flow. Therefore, the use of a complex three-dimensional boundary layer model is not warranted here, and the simple and reasonably accurate two-dimensional technique developed by Thwaites [67] is employed along the surface projections of the inviscid streamlines.

In the Thwaites method, the momentum integral equation is written in the form

$$\frac{d}{ds}\left(\frac{\lambda}{dU/ds}\right) = \frac{L(\lambda)}{U}$$

where

$$\lambda = \frac{\theta_{11}^2}{\nu}\frac{dU}{ds}$$

$$L = 2\left[\frac{\tau_0\theta_{11}}{\mu U} - \lambda(H+2)\right] .$$

By approximating L as a linear function of the pressure gradient parameter (i.e., $L \approx 0.45 - 6\lambda$), Thwaites obtained the following explicit relation for momentum thickness:

$$\left(\frac{\theta_{11}}{r_t}\right)^2 = \frac{0.45}{Re_t(U/U_t)^6}\int_0^{s/r_t}\left(\frac{U}{U_t}\right)^5 d\left(\frac{s}{r_t}\right) \qquad (5.1)$$

where all quantities have been made dimensionless using impeller tip speed (U_t) and radius (r_t). Equation (5.1) is integrated along the pressure and suction surfaces near mid-blade height starting at the leading edge. The local boundary displacement thickness is determined from the local shape factor H which is given as a universal function of λ.

The laminar boundary layer calculation is terminated if either of the following phenomena is predicted:

1 Natural transition from laminar to turbulent flow

2 Laminar separation followed by reattachment as a turbulent boundary layer.

Extreme cases where separation without reattachment occurs are not treated in the present analysis.

The location of the transition point is affected by several factors which include pressure gradient, Reynolds number, freestream turbulence, and surface roughness. In the present method, however, a simple empirical relation due to Michel which is given in reference [68] is used to determine transition. The formula is

$$Re_{\theta_{trans}} = 1.174\ Re_{\ell_{trans}}^{0.4} \tag{5.2}$$

This approach neglects the distance between the neutral stability point (point downstream of which disturbances are amplified) and the transition point. But since the pressure gradient is usually adverse, these two locations should be quite close. At the grid point or station immediately downstream of the transition point, the turbulent boundary layer calculation is initiated using the momentum thickness at transition. The shape factor used to start the turbulent

calculation is obtained from the following relation given by Coles [69]:

$$H_{trans} = 0.9698 + \frac{1.4754}{\log_{10} Re_{\theta_{trans}}} \qquad (5.3)$$

When the pressure gradient is sufficiently adverse, a laminar separation bubble is formed with subsequent reattachment as a turbulent boundary layer at some location downstream. Separation is assumed to occur when the pressure gradient parameter λ reaches a minimum value of -0.9 as suggested by Thwaites [67]. Since no reliable method is available for predicting the length of the separation bubble, the turbulent boundary layer calculation is started at the next station using the momentum thickness at separation and a shape factor of 1.6.

Inlet Region

The boundary layer along the hub and shroud surfaces upstream of the impeller is assumed turbulent at the first calculation station since there is normally a sufficient length of wetted surface upstream of this point to allow transition. Given initial values for momentum thickness Reynolds number and shape factor, a two-dimensional boundary layer solution is carried out until the bladed part of the impeller is reached. At the hub and shroud calculation

stations corresponding to the blade leading edge, the values computed for Re_θ and H are used to start the three-dimensional turbulent boundary layer solution.

For the outer casing (upstream extension of the shroud), the boundary layer is computed along surface projections of the absolute flow streamlines since the casing does not rotate with the impeller. Again, the Moses method (Appendix B) is used, but with just one modification--the streamline divergence term is included. It should be noted that crossflow is initiated within the shroud boundary layer as it passes from the stationary inlet duct to the rotating impeller surface. This crossflow, which is opposite in direction to that arising from the blade-to-blade pressure gradient, is neglected here as is the effect of the clearance gap.

The hub boundary layer, on the other hand, is computed using the relative streamline projections since this surface is rotating. When the hub is cylindrical, the inviscid flow streamlines will follow a helical path relative to the impeller and the boundary layer flow will be collateral. If the hub shape is other than cylindrical, this method (Moses) provides only a rough approximation since crossflow will be present in the boundary layer.

Initial Conditions

The laminar boundary layer solution for the blade leading edge region and the two-dimensional turbulent

calculation for the inlet region both provide initial conditions for the three-dimensional boundary layer analysis. These conditions, which may have a significant effect upon the downstream flow, are specified in terms of momentum thickness Reynolds number Re_θ and shape factor H. In order to furnish the initial parameter values required for the streamwise calculation, i.e., C_f and R_δ, a curve fit of the form $C_f = f(Re_\theta, H)$ and the relationship between θ_{11} and δ corresponding to the Moses method are employed. Initial values for the tangent of the limiting wall streamline angle ε, the parameter used in the hub and shroud boundary layer analysis, need not be specified except at the pressure surface corners where a value of zero is assumed.

Impeller Discharge Matching Condition

At the rotor exit or tip where fluid particles flowing along either side of a blade initially come into contact, we have the requirement that the static pressure be continuous. In other words, at the blade trailing edge the static pressures at corresponding points on the pressure and suction surfaces must be equal to satisfy the Kutta condition. For an inviscid flow with constant relative total pressure, it follows that the relative velocities must also be equal. But in reality, boundary layers exist on these surfaces making the equal velocity criterion employed in Chapter III inapplicable.

Therefore, in order to apply the condition of equal static pressures, we must first establish a relation between the relative velocities at the outer edges of the blade pressure and suction surface boundary layers, U_{ps} and U_{ss}.

The static pressure at any point within the inviscid core flow is given by equation (4.15) as

$$p = P_R - \rho\frac{U^2}{2} + \rho\frac{\omega^2 r^2}{2} \tag{5.4}$$

where the relative total pressure P_R is a constant determined by the upstream conditions. Also, according to equation (4.14) the static pressure gradient normal to the wall for flow within the boundary layer is

$$\frac{\partial p}{\partial y} = \rho\frac{\omega^2}{2}\frac{\partial r^2}{\partial y} + 2\rho\omega_2 u \tag{5.5}$$

where curvature effects have been neglected (this assumption is justified later). Integrating equation (5.5) from the wall to the edge of the boundary layer yields

$$p_\delta - p_0 = \rho\frac{\omega^2}{2}(r_\delta^2 - r_0^2) + 2\rho\omega_2\int_0^\delta u\,dy .$$

Noting the definition of boundary layer displacement thickness (4.30), and substituting equation (5.4) to eliminate

the static pressure at $y = \delta$ we obtain

$$P_R = P_0 - \rho\frac{\omega^2 r_0^2}{2} + \rho\frac{U^2}{2} + 2\rho\omega_2 U(\delta-\delta_1^*) \quad . \tag{5.6}$$

Equation (5.6) applies for either the pressure or the suction side of the passage, and since the radii and static pressures are equal at the trailing edge (neglecting blade thickness effects), we can equate the expressions for the two surfaces with the result

$$U_{ss}^2 - U_{ps}^2 = -4[\omega_{2_{ss}} U_{ss}(\delta-\delta_1^*)_{ss} + \omega_{2_{ps}} U_{ps}(\delta-\delta_1^*)_{ps}] \quad . \tag{5.7}$$

However, as already pointed out in Chapter IV, the pressure surface boundary layer will be much thinner than the suction surface boundary layer at the impeller exit, and we may simplify equation (5.7) to

$$\frac{U_{ps}}{U_{ss}} = \left\{1 + \frac{4\omega_2\delta_{1ss}^*(\kappa-1)}{U_{ss}}\right\}^{\frac{1}{2}} \tag{5.8}$$

where κ, which equals δ/δ_1^*, reaches a minimum value of 2 when the flow separates and forms a wake. According to equation (5.8), the relative velocity at the impeller exit will usually be greater near the pressure surface than it will near the suction surface, a trend that is well verified experimentally [36, 41].

To check the quantitative agreement of equation (5.8) with experimental data, it was applied to the measurements reported by Lennemann [38] for a 9-inch diameter impeller with circular arc blades operating at 140 rpm in water. For the maximum flow conditions, the data taken near mid-blade height indicated that $U_{ps} \approx 4.5$ ft/sec, $U_{ss} \approx 3.5$ ft/sec, $\delta^*_{l_{ss}} \approx 0.0173$ ft, and $\kappa \approx 3.6$. This results in a predicted pressure side velocity of 4.6 ft/sec, or a 2% error. If streamline curvature effects are accounted for by using the local blade surface radius, the predicted velocity is reduced by less than 2%. Thus, the neglect of curvature effects appears justified.

Flow in the Vaneless Diffuser

Generally, the flow entering the constant width vaneless diffuser section which is located immediately downstream of the impeller will be highly nonuniform with respect to both the axial and circumferential directions. At a radius sufficiently far downstream of the impeller discharge, the flow is expected to attain uniformity with the exception of the boundary layers on the stationary side walls. The region in between where these two flow conditions exist is not readily analyzed because of (1) the complex nature of the entering flow which is unsteady in stationary coordinates, (2) three-dimensional boundary layer flow along the parallel

walls, and (3) the mixing process between the core flow and the viscous wakes shed from the impeller surfaces.

It is realized that the impeller flow and diffuser flow must be coupled to some extent, but a detailed investigation of the vaneless diffuser is beyond the scope of the present analysis. Instead, a simple model which retains the assumption of an inviscid core flow is used to establish the downstream periodic boundaries needed for the inviscid flow solution described in Chapter III. Although this approach does not specifically account for losses downstream of the impeller, it does incorporate several of the important results from vaneless diffuser flow measurements and analytical techniques in current use.

The diffuser flow model is based on the analyses developed by Dean and Senoo [70] and Johnston and Dean [71]. In reference [70] a prediction method is proposed for vaneless diffuser losses wherein the impeller discharge flow is assumed uniform from hub to shroud, but in the circumferential direction the flow is divided into two regions: a jet adjacent to the pressure surface containing the high energy core flow, and a wake adjacent to the suction surface made up of low energy fluid. At a given radius, the throughflow velocity is assumed constant in either region, while an average value of the relative flow angle is used for the entire passage cross-section. Equations governing the radial

variation of the wake and jet parameters are derived by considering the frictional forces between the fluid and the walls and between the jet and wake, and accounting for reversible work transfer between the jet and the wake caused by the associated fluctuating pressure difference in absolute coordinates. The theory predicts a rapid decrease in wake thickness with increasing radius ratio (r/r_t), and also indicates that shear stresses arising from mixing between the jet and wake regions have a negligible effect upon the flow compared to the wall shear.

Reference [71] presents a simpler approach which may be used in place of the above analysis with only a slight sacrifice in accuracy. In this method, the angular momentum exchange or mixing between the jet and wake regions is assumed to occur immediately at the impeller exit resulting in axisymmetric flow throughout the diffuser. Then, considering only those shear stresses due to the walls, a one-dimensional analysis is carried out yielding a relation for the mass averaged angular momentum as a fraction of radius. The result may be written as

$$Y \equiv \frac{r\hat{V}_\theta}{(r\hat{V}_\theta)_t} = \frac{1}{1 + \lambda_t \hat{C}_f r_t / b_t \xi} \tag{5.9}$$

where $\hat{V}_\theta$ is the mass-flow-average absolute tangential velocity component, $\lambda = \hat{V}_\theta / \overline{V}_m$, $\overline{V}_m = \overline{W}_m$ is the area averaged

meridional velocity component, $\hat{C}_f$ is the integrated average friction coefficient from impeller tip to diffuser exit, b_t is the impeller discharge width or blade height (assumed equal to the diffuser width in the present analysis), and $\xi = (r-r_t)/r_t$.

The inviscid flow analysis described in Chapter III was based on the assumption that the mass-averaged angular momentum remains constant downstream of the impeller in order to calculate the periodic boundary shapes in the vaneless diffuser. In the combined flow analysis, however, equation (5.9) is applied at each radial station in the diffuser to determine the reduced value of $r\hat{V}_\theta$ which is used in conjunction with equation (3.27) to establish the θ coordinates of the downstream periodic boundaries. A value of $\hat{C}_f$ of 0.01 (within the range suggested by Johnston and Dean [71]) is used, and the average meridional velocity component at the impeller tip ($\bar{V}_{m_t}$) is evaluated using the passage area at the discharge corrected for the boundary layer displacement thicknesses on all surfaces. Again, as explained in Chapter III, the value of $\hat{V}_\theta$ at the impeller exit is specified in terms of $\mu = \hat{V}_{\theta_t}/U_t$ as part of the iteration required to satisfy the exit matching condition.

The displacement effect of the boundary layers may be significant within the impeller passages making it physically and numerically unreasonable to allow the inviscid

core flow and the surrounding boundary layers to mix together suddenly in the diffuser entry region. In the analysis of reference [70], the predictions indicate that a wake having zero through-flow will disappear at a radius ratio $r^*/r_t \leq 1.2$ based on calculations covering a broad range of the independent variables. Furthermore, a fair approximation to the rate at which the wake thickness decays with radius ratio is given by

$$\frac{\sigma}{\sigma_t} \simeq 1 - \left(\frac{\xi}{\xi^*}\right)^2 \quad \text{for} \quad \xi \leq \xi^* \tag{5.10}$$

where

$$\sigma \equiv \frac{\text{wake thickness}}{\text{passage width}} = \frac{r\Delta\theta_{wake}}{2\pi r/Z} = \frac{\Delta\theta_{wake}}{\Delta\theta_b}$$

and ξ^* is the value of ξ at which the wake thickness reaches zero (e.g., $\xi^* = 0.2$ for $r^*/r_t = 1.2$). A schematic showing the wake collapse model employed in the analysis is presented in Fig. 5.1. As indicated in the sketch, the wake thickness $r\Delta\theta_{wake}$ at the impeller tip represents the sum of the blade thickness and the pressure and suction surface boundary layer displacement thicknesses, all measured tangentially. Once a boundary layer solution has been obtained, a new inviscid flow calculation is performed using the wake borders as the periodic boundaries for the downstream flow. Finally, we

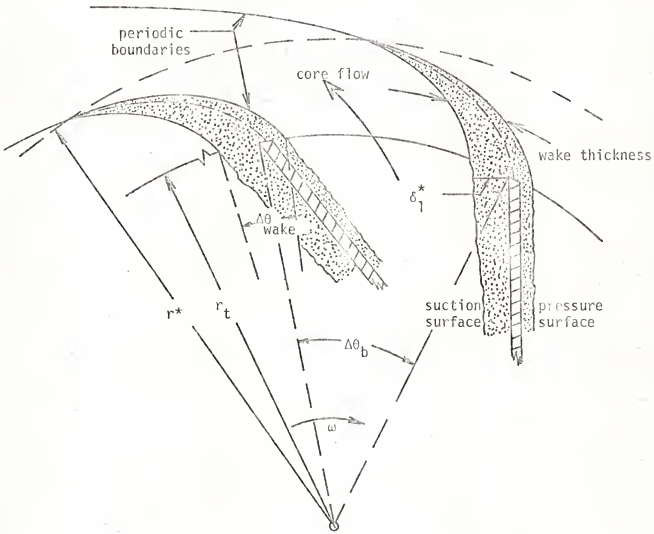

Fig. 5.1. Wake Collapse Model for Vaneless Diffuser

must account for the displacement of the diffuser core flow by the side wall boundary layers. In the absence of a detailed diffuser flow analysis, the boundary layer displacement thicknesses on the hub and shroud at the impeller discharge midway between the blades is used throughout the vaneless diffuser.

Viscous/Inviscid Flow Interaction

The predicted inviscid flow within the impeller passages can be modified to account for viscous effects through the addition of the boundary layer displacement thickness to the original channel geometry. With the new bounding surfaces prescribed, the calculation scheme described in Chapter III can be used to obtain a refined estimate of the impeller flow field. As a result, the calculated velocity and pressure distributions near the passage walls are altered causing subsequent changes in the predicted boundary layer development. This coupling between the viscous and inviscid regions makes it necessary to complete several iterations between the inviscid flow and boundary layer calculations before satisfactory convergency is achieved.

Inviscid Flow Input for Boundary Layer Analysis

As explained in Chapter III, the inviscid flow is calculated at a relatively small number of streamwise

stations ($\leq$ 20) defined by the intersections of conic surfaces with the impeller passages. The boundary layer flow (Chapter IV), on the other hand, is computed at several streamwise stations ($\geq$ 100) using a coordinate system based on the surface projections of the inviscid flow streamlines adjacent to the passage walls. In either case, the grid point locations can be expressed in terms of meridional distance m along a particular streamline. This allows direct interpolation back and forth between the two distinct calculation schemes and coordinate systems.

The required inviscid flow input to the turbulent boundary layer analysis includes:

1 Meridional distance along the streamlines adjacent to the blade pressure and suction surfaces.

2 The meridional and relative flow angles (α and β) at each grid point along the streamlines adjacent to the hub, shroud, and blade surfaces.

3 The radial and circumferential coordinates (r and θ) for the hub and shroud grid points, and the radial coordinates for the blade surface grid points.

4 Relative velocities at each grid point adjacent to the passage walls including the corner velocities (see Fig. 4.8).

Certain parameters such as the normal distances between the

hub and shroud, the curvatures of the meridional normals, the direction cosines needed to determine the angular velocity component ω_2 along the hub-to-shroud normals, and the meridional distances along the hub and shroud are computed only once at the start of the calculation procedure since they do not change from one iteration to the next. The angles, coordinates, and velocities listed above are obtained from the inviscid flow data by means of piecewise cubic interpolation (Appendix A). In the case of the blade surface velocities, it is sometimes necessary to correct for the surface normals being at an angle to the conic surfaces used to compute the inviscid flow. When the core flow prediction is based on a previously calculated displacement thickness distribution, the interpolation procedure is modified such that the relative velocities used in the boundary layer analysis correspond to those predicted along a normal to the surface at each grid point.

Corrections for Boundary Layer Displacement Thickness

After a boundary layer solution is established, including the separate calculations for the upstream flow and the laminar flow near the blade leading edge, the grid points adjacent to the impeller surfaces are relocated such that their normal distance from the wall equals the local boundary layer displacement thickness. First, however, the values of displacement thickness corresponding to the inviscid flow

grid points must be obtained from the values computed for the boundary layer grid points by interpolation. Since the number of boundary layer grid points is considerably greater than the number of inviscid flow grid points along a given streamline, simple linear interpolation is used with meridional distance as independent variable.

To correct the hub and shroud coordinates for boundary layer blockage, the grid points must be shifted along the straight line elements or rays defined by the intersections of the conic surfaces with the meridional plane (see Fig. 3.8). The distances along these rays is denoted by n, where n = 0 at the hub. Referring to Fig. 3.9, it can be shown that the distance Δn that a grid point should be displaced from the hub or shroud surface along a ray is related to the boundary layer displacement thickness through

$$\Delta n = \frac{\delta_1^*}{\cos(\phi - \alpha)} \quad . \tag{5.11}$$

Since a linear relation exists between the distance n and the r and z coordinates along a ray, it follows that

$$\Delta r = \frac{\Delta n}{n_s} (r_s - r_h) \tag{5.12}$$

and

$$\Delta z = \frac{\Delta n}{n_s} (z_s - z_h) \tag{5.13}$$

where the subscripts denote fixed values of the coordinates at the hub and shroud surfaces.

For the blades, the grid points adjacent to the pressure and suction surfaces must be shifted in the circumferential direction on the conic surfaces with n held constant. If we assume that the actual blade surfaces are parallel to the mean blade surface $\theta_b(r,z)$, then the following relation may be used to determine the local grid point displacement $\Delta\theta$:

$$\Delta\theta = \frac{\delta_1^*}{r} \sqrt{1 + r^2\left(\frac{\partial\theta_b}{\partial r}\right)^2 + r^2\left(\frac{\partial\theta_b}{\partial z}\right)^2} \qquad (5.14)$$

This is essentially the same as equation (3.31) which provides a relation between the normal and tangential blade thicknesses in terms of the mean blade shape.

The updated grid point locations found using equations (5.11)-(5.14) define the shape of either S1 stream surfaces which take the place of the original hub and shroud contours, or S2 stream surfaces which replace the blade surface coordinates. These newly determined passage boundaries, together with the downstream periodic boundaries established using the wake collapse model, become the geometric input for the next pass through the inviscid flow calculation.

The principal influences of the above corrections for viscous effects upon the inviscid core flow are as

follows:

1. A reduction in passage cross-sectional area resulting in an increase in the average core flow velocity.
2. A change in flow direction near the impeller surfaces due to the presence of boundary layers, particularly near the blade suction surface.

The first item is easily accommodated within the mass flow integration procedure described in Chapter III. But the calculation of flow angles (and also streamwise derivatives) near the passage walls often leads to numerical difficulties when separation occurs along the suction surface. Because of this, it is necessary to smooth either the boundary layer displacement thickness distribution or the computed flow angles adjacent to the blade surface. The latter approach has proven more effective, and is employed here in such a manner that the primary changes are reflected in the slopes, while the smoothed quantities are quite close in magnitude to their original values. Finally, because of the uncertainty associated with the streamwise derivatives occurring in equations (3.18) at grid points within the boundary layer, the parameters A, B, and C used to determine the relative velocity distribution are weighted less heavily near the wall. In other words, when equation (3.17) is integrated across the passage along an S1 stream surface, the numerical

integration between a grid point closest to the blade and the adjacent grid point is carried out using 50% and 150% of the parameter values (A,B,C) at the respective points.

Convergence Problems

Numerical stability can be a major problem with any iterative method. The application of boundary layer corrections to the impeller surface geometry often results in large changes in the calculated inviscid flow velocity field from one iteration cycle to the next. This undesirable feature can be avoided by using sufficient underrelaxation to stabilize the solution. In the present analysis, each boundary layer solution is determined from a velocity field weighted between the current inviscid flow solution and the previous input to the viscous flow calculations. Denoting the relaxation factor by ψ, for each grid point adjacent to the impeller surfaces we have

$$U_i' = U_{i-1}' + \psi(U_i - U_{i-1}') \tag{5.15}$$

where

U_i' = velocity at the boundary layer edge used for the i^{th} iteration

U_{i-1}' = velocity at the boundary layer edge used for the $(i-1)^{th}$ iteration

U_i = velocity obtained from the inviscid flow solution for the i^{th} iteration.

In a similar manner, the inviscid flow solutions are determined using a displacement thickness distribution given by the analogous expression with δ_1^* replacing U. It has been found that $\psi = 0.5$ is usually near the optimum for the first two iterations, while $\psi = 0.2$ gives satisfactory results for subsequent iterations.

Typical results are presented in Fig. 5.2 where the maximum values of $|U_i - U'_{i-1}|$ and $|\delta_{1_i}^* - \delta_{1_{i-1}}^{*'}|$ normalized with respect to impeller tip speed and radius are plotted against the number of iterations completed. The oscillatory behavior of the displacement thickness shown here results from a shifting of the location at which the suction surface boundary layer separates.

Additional stability is provided for early iterations by limiting the maximum allowable streamline shifts and the values for streamwise derivatives in the inviscid flow calculation. Also, a limitation is placed upon the maximum boundary layer displacement thickness based on passage dimensions.

Matching of Inviscid and Boundary Layer Velocity Profiles

When the separate calculations for the inviscid and viscous regions are combined iteratively, two difficulties arise regarding the patching together of the respective velocity profiles. First, because of the effects of relative

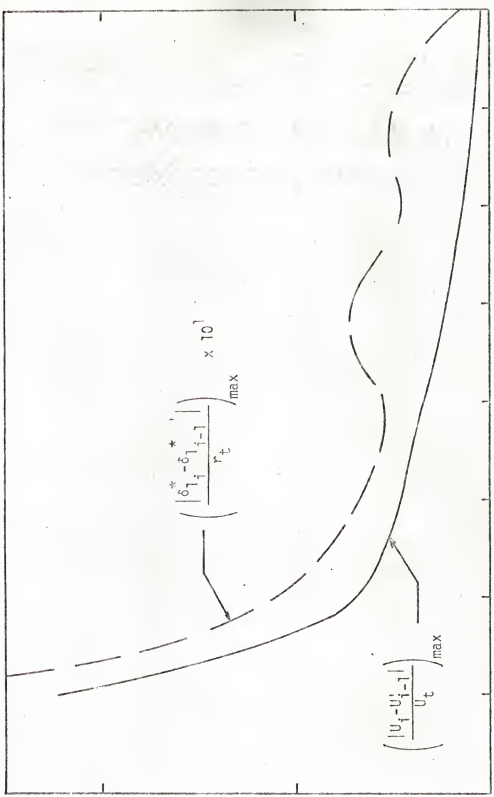

Fig. 5.2. Typical Convergence Properties of the Combined Flow Solution

vorticity ($-2\vec{\omega}$) and surface curvature (K_{13}), the inviscid core flow velocity W is not constant outside the boundary layer in a direction normal to the surface. Although this condition does not alter the equations governing boundary layer flow and does not invalidate the boundary layer hypothesis (providing W is not a rapidly varying function of y), it does impose the additional boundary condition that the slopes of the freestream and boundary layer velocity profiles must match at the outer edge of the boundary layer. The second problem is also a consequence of W varying with y, and it concerns the values of U (the relative velocity at $y = \delta$) used as input to the boundary layer analysis. As mentioned earlier, these velocities are evaluated as part of the mass flow integration at the grid points corresponding to the passage boundaries corrected for displacement thickness. Thus, if the local relative velocity gradient normal to the surface is nonzero, then there will be a difference in the value of U furnished as input (i.e., W at $y = \delta_1^*$) and the correct value corresponding to $y = \delta$.

An indication of the importance of these effects may be obtained by comparing the slope of the inviscid flow velocity profile at the outer edge of the boundary layer $(\partial W/\partial y)_\delta$ with the average slope of the boundary layer velocity profile $(\partial u/\partial y)_{avg}$. From equation (4.20) we obtain the following inviscid flow relation:

$$\left(\frac{\partial W}{\partial y}\right)_{\delta} = -2\omega_2 + K_{13}U \tag{5.16}$$

where ω_2 is the angular velocity component normal to the streamwise direction and parallel to the surface, and $|K_{13}|$ is approximately equal to the local surface curvature $(1/R_c)$ for $\delta/R_c << 1$. Representing the average boundary layer slope by U/δ yields

$$\frac{\left(\frac{\partial W}{\partial y}\right)_{\delta}}{\left(\frac{\partial U}{\partial y}\right)_{avg}} \simeq \frac{-2\omega_2\delta}{U} \pm \frac{\delta}{R_c} \tag{5.17}$$

which is similar to the expression for Richardson number given by equation (4.59). When equation (5.17) is applied in the blade-to-blade plane of a radial flow impeller with straight blades ($\omega_2 = \pm\omega$, $1/R_c = 0$), the right-hand side becomes $\pm 2\omega\delta/U$. According to reference [52], typical values for this term will be less than 0.1 near the exit of a centrifugal pump or compressor. For backward-leaning blades the slope ratio given by equation (5.17) is even smaller, since the rotation and curvature terms counteract one another. Hence it appears reasonable to neglect the slope discontinuity at $y = \delta$ in view of the approximate nature of the combined flow analysis.

Although the outer boundary condition is not enforced during the iterative calculations, it is desirable in the

final solution to have inviscid and boundary layer velocity profiles which join smoothly. This is particularly useful for comparison of predicted blade-to-blade velocity profiles with experimental results. Reference [72] suggests the following scheme for constructing composite profiles based upon the method of matched asymptotic expansion and accurate to the first order:

$$\begin{matrix}\text{composite}\\ \text{profile}\end{matrix} = \begin{matrix}\text{inner}\\ \text{profile}\end{matrix} + \begin{matrix}\text{outer}\\ \text{profile}\end{matrix} + \begin{matrix}\text{common}\\ \text{asymptote}\end{matrix} .$$

Denoting the resultant or composite streamwise velocity component by $\tilde{u}$, the above formula may be written

$$\tilde{u}(y) = u(y) + W(y) - U \quad . \tag{5.18}$$

The terms comprising equation (5.18) are illustrated in Fig. 5.3 where U is again taken to be the inviscid flow velocity computed for $y = \delta_1^*$, but used as the local freestream velocity in the boundary layer analyses.

In reference [72], this procedure was applied after only a single boundary layer calculation with U corresponding to the inviscid flow velocity computed at the surface ($y = 0$). But here it is assumed that $W(y) = U$ for $y \leq \delta_1^*$, hence the boundary layer velocity profile is unaltered by equation (5.18) within the displacement thickness.

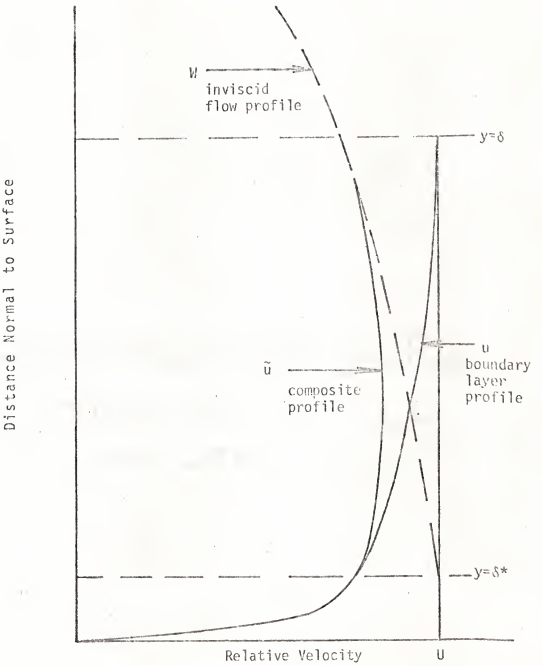

Fig. 5.3. Matching Inviscid Flow Velocity Profiles with Boundary Layer Profiles

Furthermore, it should be noted that the definition of boundary layer displacement thickness employed in the mass flow integration remains valid for the composite profile obtained using equation (5.18), i.e.,

$$U\delta_1^* \equiv \int_0^\delta (U-u)dy = \int_0^\delta (W-\tilde{u})dy \qquad (5.19)$$

where the expression on the right represents a generalized displacement thickness which accounts for W varying with y.

Overall Calculation Procedure

The details of the inviscid flow and boundary layer analyses are thoroughly documented in the preceding chapters, and will not be repeated here. Instead, the following brief summary of the combined flow analysis is provided:

1 Input control parameters, options, geometric data, upstream fluid properties, impeller operating conditions, grid specifications, and initial values for boundary layer solution.

2 Establish a permanent boundary layer calculation grid for the impeller surfaces consisting of streamwise stations along the hub and shroud, and chords of circular arc normals along the blade surfaces.

3 Compute a complete inviscid flow solution (steps 2 through 12 of the procedure outlined in Chapter III) using the prescribed surface geometry.

4 Interpolate along the inviscid flow streamlines adjacent to the passage boundaries to obtain the necessary input to the boundary layer analyses.

5 Calculate the boundary layer development along the hub, shroud, and blade surfaces using the procedures described previously.

6 Obtain displacement thickness values at the inviscid flow grid points by interpolation, and correct the hub, shroud, and blade surface coordinates for frictional effects.

7 Compute an improved estimate of the inviscid core flow using the same method as in step 3, but with the modified surface coordinates.

8 Repeat steps 4 through 7 until sufficiently small variations in displacement thickness and core flow velocity are indicated.

9 Output the complete flow field description including streamline coordinates, relative velocities, flow angles, boundary layer properties, and hub-to-shroud and blade-to-blade velocity profiles at the impeller exit plane.

At present, the additional iteration required to satisfy the exit matching condition, equation (5.8), is

performed externally by computing two or more complete solutions based upon different values of μ, the input parameter controlling the shape of the downstream periodic boundaries. By observing the variation of U_{ps}/U_{ss} with μ, the correct input value is readily determined in the majority of cases (when the variation is highly nonlinear, several guesses are required). Although this same procedure could just as easily be made a part of the overall calculation, the possibility of slow convergence and excessive computer time makes such an approach impractical at this time.

The computer program comprising the combined flow model is programmed in Fortran IV for the IBM 370/165. Storage requirements are approximately 450,000 bytes for an inviscid flow grid consisting of 21 streamwise stations, 13 blade-to-blade (S1) stream surfaces, and 13 hub-to-shroud (S2) stream surfaces. Typical computation time based on a 15x7x7 grid is at least 25 seconds per cycle (steps 4 through 7 above).

CHAPTER VI

RESULTS AND DISCUSSION

In this chapter, the analysis procedures developed in Chapters III, IV, and V for flow in centrifugal impellers are applied to several configurations for which the required geometrical data are available. Furthermore, the combined flow analysis is compared with experimental results for a rotating diffuser and a radial-flow impeller with swept-back blades.

Inviscid Flow Calculations

The inviscid flow calculation procedure described in Chapter III provides a useful tool for the design and analysis of centrifugal impellers. Although the important effects of viscosity are neglected, the detailed velocity field predicted by this method is still qualitatively correct over most of the passage (the largest deviation should occur near the impeller exit). Thus for design applications, the method could be used to determine (by trial and error) hub and shroud contours and blade shapes which do not result in large velocity gradients conducive to boundary layer separation and hence excessive losses.

A severe test of the inviscid flow analysis is provided in references [8] and [12], where specifications are given for a 6-to-1 pressure ratio centrifugal impeller with an inducer. It has swept-back blades and is operating at 75,000 rpm. The flow is highly three-dimensional, and is actually supersonic in the leading edge region near the shroud.

Figure 6.1 shows how the blade surface velocities predicted for this impeller by the present method compare with those obtained using three other compressible flow analyses. The methods presented for comparison represent some of the best available two-dimensional and quasi-three-dimensional techniques according to reference [12].

The CHANEL solution is simple to apply, and gives good results for subsonic, choked, and slightly supersonic flow in well-guided passages. However, it gives poor results near the inlet and exit because it is based on the assumption that the flow direction coincides with the passage shape, and employs a linear variation in streamline curvature from hub to shroud.

The TSONIC method provides a two-dimensional blade-to-blade streamline curvature solution on a surface of revolution for subsonic and transonic flow. To use this analysis, one must first specify the exit angle or slip factor, and also a flow rate and the thickness normal to

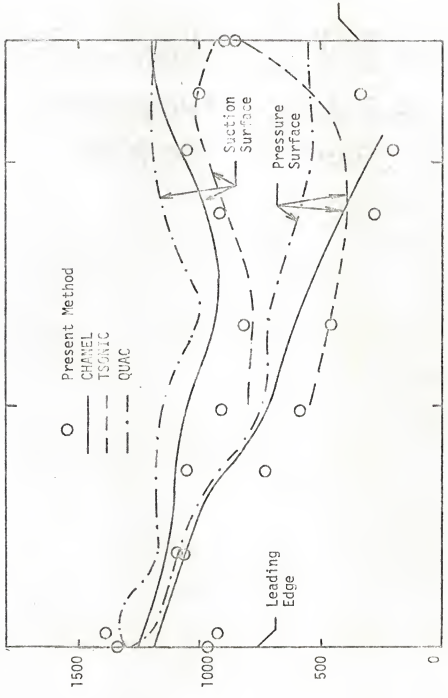

Fig. 6.1. Comparison of Inviscid Flow Analysis with Other Calculation Methods Blade Surface Velocities for 6:1 PR Transonic Compressor

the surface of revolution on which the flow is assumed to take place. This normal thickness is assumed constant in the blade-to-blade direction, and must be obtained from a mean S2 stream surface solution.

The QUAC analysis is a quasi-three-dimensional technique in which a linear blade-to-blade velocity distribution is superimposed on a two-dimensional meridional plane solution. This method also gives inadequate results near the inlet and exit.

The obvious discrepancy between the present method and the others near the leading edge is believed to result from the inaccuracy of the two-dimensional techniques in this region (the TSONIC solution is incomplete because of supersonic flow near the inlet). In fact, the impeller is operating at a positive incidence (i.e., $(\beta_b - \beta) > 0$ at the leading edge) of about 7 degrees; this should cause significant blade loading at the leading edge.

Since no detailed experimental data are available for this impeller, it is impossible to judge which approach gives the best results. However, it is clear from Fig. 6.1 that even though the same general trends are exhibited, there are substantial differences in the predictions.

Another numerical example using the inviscid flow analysis is presented in Fig. 6.2. Predicted relative velocity distributions are given for the hub, shroud, and blade

surfaces of a 6-inch diameter radial-bladed centrifugal compressor designed to operate with argon at 38,500 rpm (the geometric specifications were obtained from reference [8]). The surface velocities shown in Fig. 6.2 correspond to conditions along the mean S2 stream surface which extends from hub to shroud, and along the mean S1 stream surface which extends from blade to blade.

The solution represented in Fig. 6.2 was obtained using a total of sixteen streamwise stations or conic surfaces: ten of these were within the impeller, three were located upstream of the impeller, and three were placed downstream in the vaneless diffuser. At each streamwise station, seven S1 stream surfaces and seven S2 stream surfaces were used in calculating the flow field. The relative velocity distribution for the 8th station (located near the middle of the axial-to-radial turn) can be seen in Table I. The entries in this table represent velocities calculated at grid point locations defined by the intersections of the S1 and S2 stream surfaces on the 8th conic surface. They are arranged such that a value of j=1 denotes the hub S1 stream surface, and a value of k=1 denotes the pressure surface S2 stream surface, etc. This same format is used to display the other flow variables of interest at each passage cross-section.

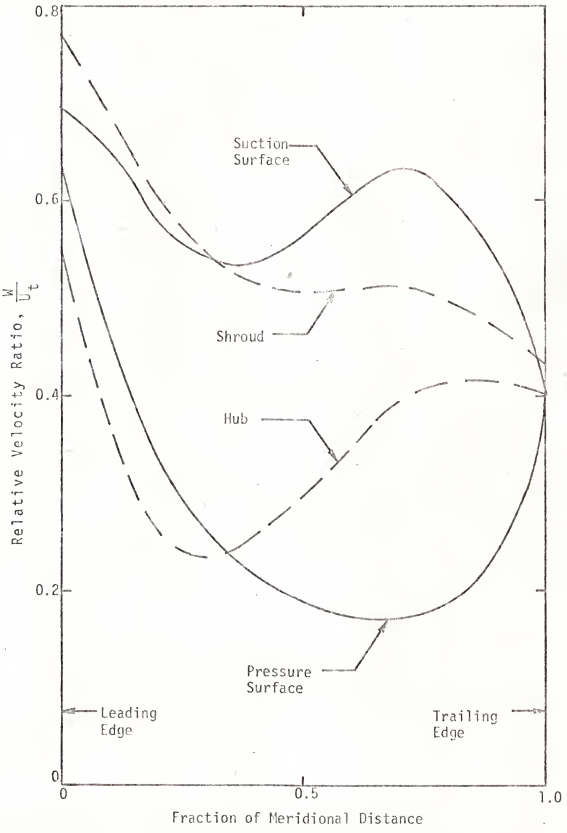

Fig. 6.2. Predicted Inviscid Flow Velocity Distribution for a Radial-Bladed Centrifugal Compressor Impeller

Table I. Predicted Relative Velocity Distribution at a Passage Cross-Section for a Radial-Bladed Centrifugal Compressor.

S1 Stream Surfaces (j) \ S2 Stream Surfaces (k)	1	2	3	4	5	6	7
7	282*	378	451	517	578	640	727
6	256	341	414	479	541	606	671
5	238	314	378	436	492	549	604
4	218	284	339	391	441	491	539
3	197	254	301	346	389	434	474
2	173	223	264	303	340	377	410
1	145	183	223	257	290	323	334

* Velocities are in ft/sec

Comparison with Measured Data

In this section, the combined viscous/inviscid flow analysis is applied to the rotating diffuser flow investigated experimentally by Moore [46], and also the radial impeller with swept-back blades studied by Lennemann [38]. Although it would be desirable to investigate the validity of the present analysis for other more complex impeller flows, the detailed experimental data required are either unavailable, of doubtful accuracy, or there are insufficient information about the test configuration. Nevertheless, the two comparisons presented herein should provide a fairly conclusive test of the method, since the only missing effect which could possibly be significant is the hub-to-shroud pressure gradient.

Rotating Rectangular Diffuser

The test section employed by Moore [46] (see also reference [47]) consisted of a 24-inch-long diffusing channel with a constant height (measured parallel to the axis of rotation) of 3 inches. The side walls, which were radii, had an included angle of 15 degrees and an inlet width of 3 inches.

Only the two largest of the three flow conditions investigated in reference [46] will be analyzed here, since a turbulent eddy was observed on the pressure side at the low

flow rate. Also, it was not possible to obtain accurate skin friction measurements at this flow condition.

Figure 6.3 shows the measured and predicted boundary layer development for the pressure and suction sides of the channel at the medium flow. The boundary layer calculations used measured initial values for momentum thickness, with no correction for rotational effects on turbulent shear stress. Separation (i.e., wake formation) of the suction surface boundary layer is indicated when the skin friction parameter (A) becomes zero. Note that the momentum thickness predictions for both the pressure and suction surface are quite good, while the agreement for shape factor and skin friction is only fair. This may be ascribed to the effects of Coriolis forces on the turbulence structure, as discussed in Chapter IV.

In Fig. 6.4, the same experimental results are shown for the medium flow, but the predicted boundary layer development includes the effects of rotation through the use of the Richardson number correlation for mixing length given by equation (4.60). Since the value of the coefficient k in this equation has not been firmly established (in fact, k probably depends on Reynolds number and some form of rotation number (see Chapter IV) according to Johnston [53]), the calculations were carried out for k=2 and k=4 (Fig. 6.3 corresponds to k=0). It can be seen from the figure that

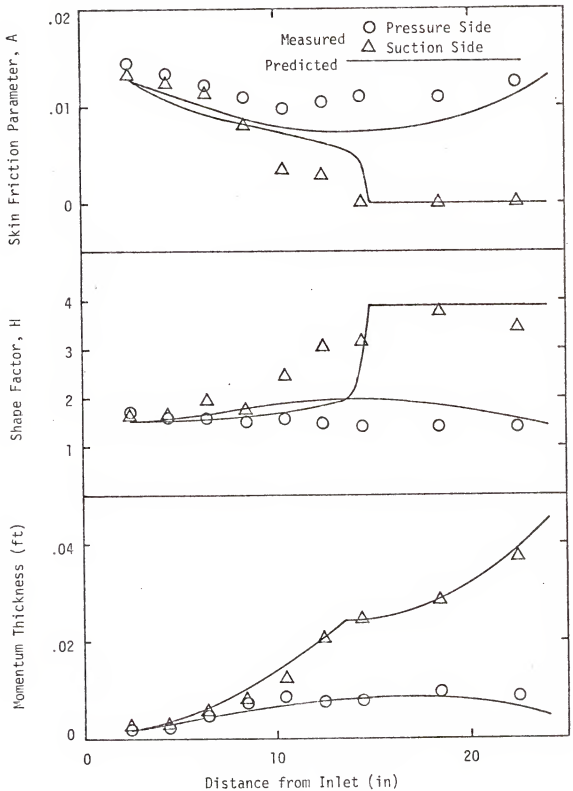

Fig. 6.3. Comparison of Measured and Predicted Boundary Layer Development for Rotating Diffuser (Medium Flow, k = 0)

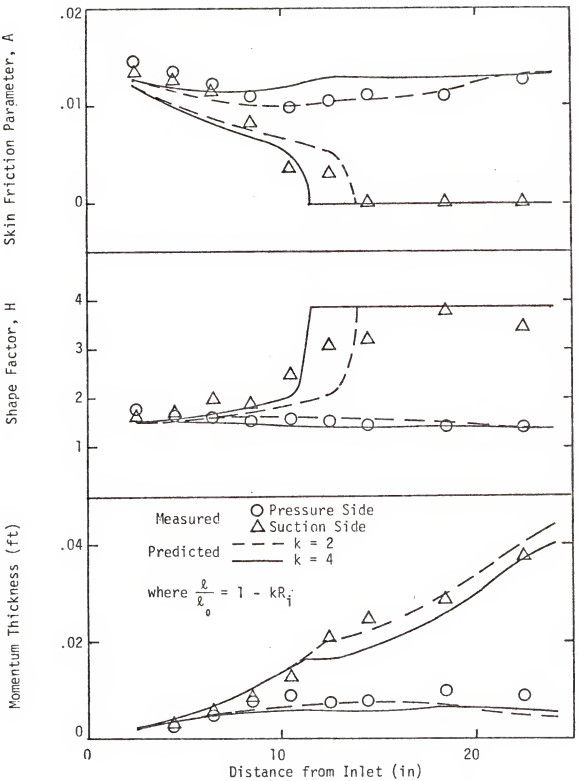

Fig. 6.4. Comparison of Measured and Predicted Boundary Layer Development for Rotating Diffuser (Medium Flow, $k \neq 0$)

this correction has a significant effect on wall shear stress, and therefore strongly influences the location of the separation point on the suction surface.

Similar results are presented in Fig. 6.5 and Fig. 6.6 for the large flow rate. As expected, a better overall fit of either set of data is obtained by using the mixing length correction, but no optimum choice for the parameter k is evident.

Figure 6.7 gives a comparison of the measured and predicted blade-to-blade velocity profiles at mid-height near the channel exit for both flow conditions. Good agreement is obtained for the two cases with k=2. The predicted hub-to-shroud velocity profiles for the mean S2 stream surface are also shown, but no data are available for comparison.

Radial-Flow Impeller with Swept-Back Blades

The impeller investigated by Lennemann [38] was 18 inches in diameter, it had 14 circular arc blades, and a constant blade height of 1 inch. The blade leading edge radius was 4.875 inches, and the inlet and discharge flow angles were -60.7 degrees and -63.7 degrees, respectively. Experimental data were obtained for a design speed of 140 rpm and a flow coefficient $\phi_t (\equiv \bar{W}_{m_t}/U_t) = 0.113$, as well as three other conditions.

Although the experimental investigation was not concerned with the details of the boundary layers within

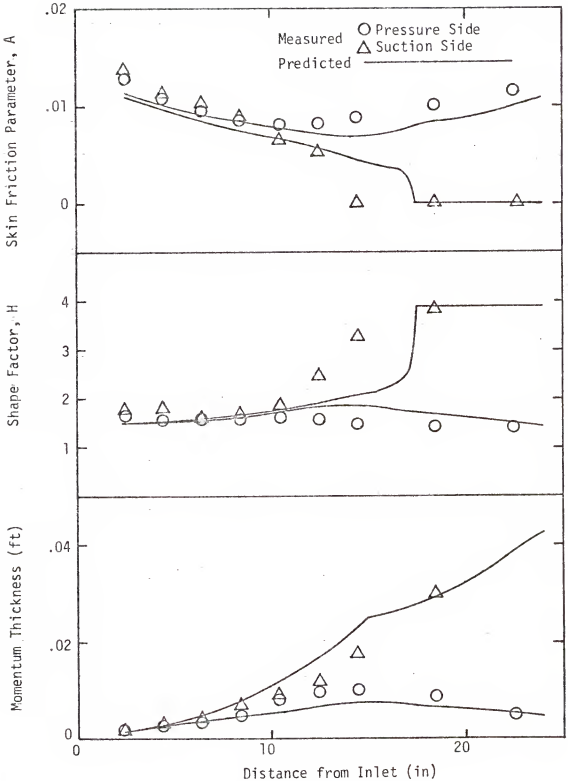

Fig. 6.5. Comparison of Measured and Predicted Boundary Layer Development for Rotating Diffuser (Large Flow, k = 0)

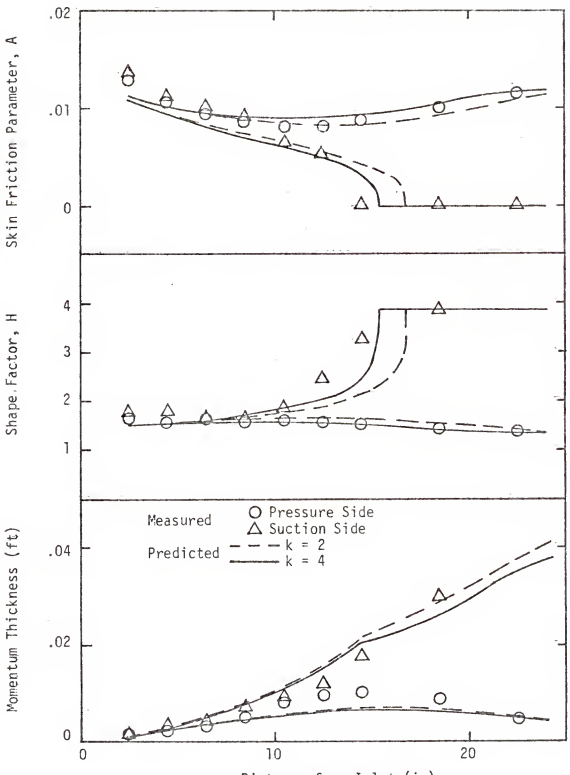

Fig. 6.6. Comparison of Measured and Predicted Boundary Layer Development for a Rotating Diffuser (Large Flow, $k \neq 0$)

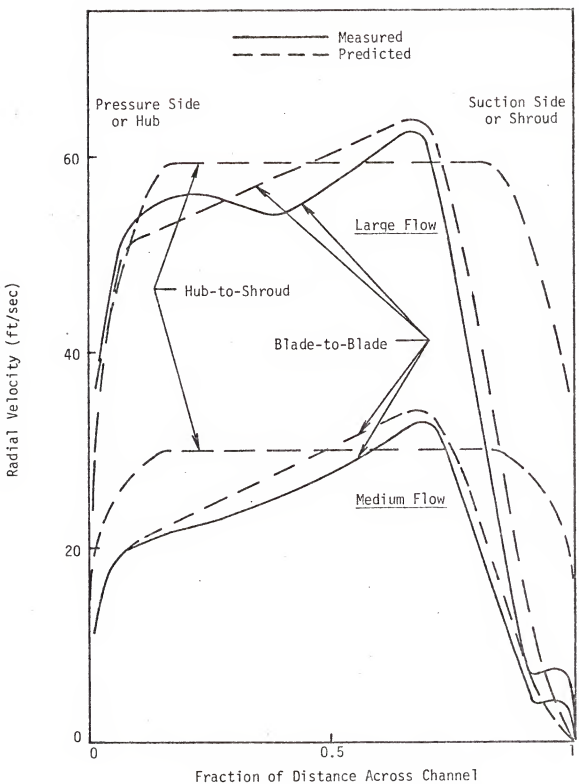

Fig. 6.7. Comparison of Measured and Predicted Velocity Profiles Near the Exit of the Rotating Diffuser

the impeller, a complete enough mapping of the velocity field was obtained to allow comparison with the present method.

Figure 6.8 shows the predicted boundary layer displacement thicknesses along the hub (or shroud), and along the suction surface. The pressure surface boundary layer remains thin all along the length of the blade, with a displacement thickness distribution which is almost identical to that shown for the hub. As explained in Chapter V, an optional laminar flow calculation is provided for the blade surface boundary layers. Because the velocities in this impeller are quite low (less than 6 ft/sec), there is a significant portion ($\approx$ 20%) of the suction surface boundary layer which is laminar, as shown by the prediction. The hub and shroud boundary layers originate upstream of the impeller, and are assumed to be fully turbulent. Agreement between the experimental and predicted suction surface boundary layer development is good, based on comparison with the measured velocity profiles near the exit (see Fig. 6.9). It should be noted that the suction surface boundary layer is not separated ($H \approx 1.8$), but it is quite thick due to the accumulation of low energy fluid transported by secondary flow. The calculations shown here, and all subsequent calculations presented in this chapter, are based on a value of k equal to 2 in the mixing length correction for rotation and curvature effects.

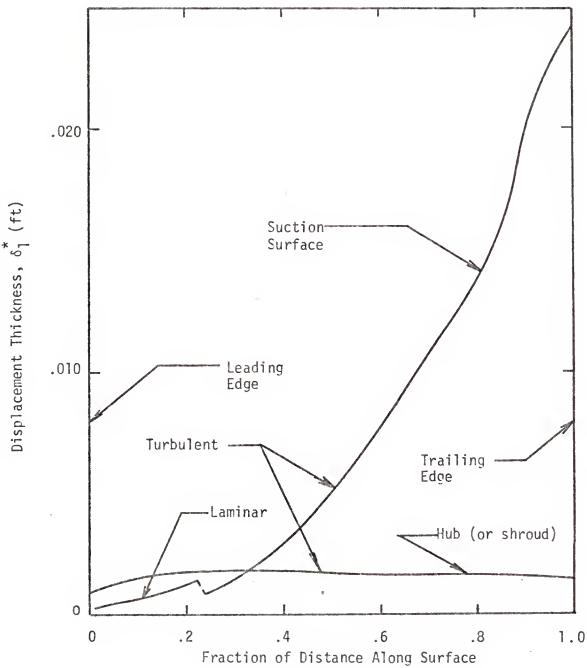

Fig. 6.8. Predicted Boundary Layer Development for Radial-Flow Impeller with Swept-Back Blades.

The measured and predicted exit velocity profiles at mid-blade height are compared in Fig. 6.9. In addition to the measured values given in reference [38], velocities which have been mass-averaged in the hub-to-shroud direction [39] are also shown. The effect of variations in the specified value (this is an input parameter) of the impeller work coefficient $\mu = V_{\theta_t}/U_t$ (see Chapters III and V) is also shown. Agreement is reasonable near the pressure surface for $\mu = 0.5$ and $\mu = 0.6$, and is good for all three values near the suction surface.

A similar comparison is presented in Fig. 6.10 for the deviation angle $(\beta_b - \beta)_t$. The differences between the mass-averaged values and those measured at mid-blade height are probably due to reduced deviation in the hub and shroud boundary layers.

Analysis of a Radial-Bladed Centrifugal Pump Impeller

In this section, the combined viscous/inviscid flow analysis is used to predict the internal flow characteristics of a shrouded centrifugal pump impeller with radial blades. Unfortunately, the performance data obtained for this design were measured downstream of the impeller exit, after the mixing of the core flow and the boundary layer flow (blade wakes) had taken place. Thus a direct comparison of measured data with predicted results is not possible.

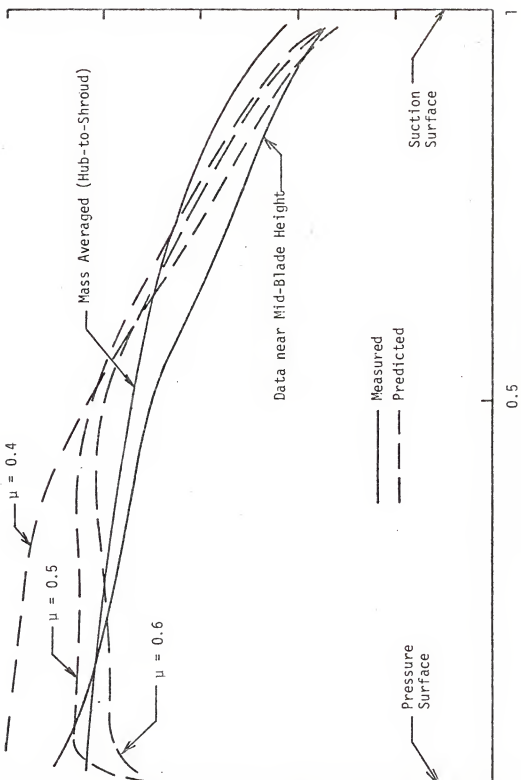

Fig. 6.9. Comparison of Measured and Predicted Exit Velocity Profiles for Radial Impeller with Backward-Swept Blades

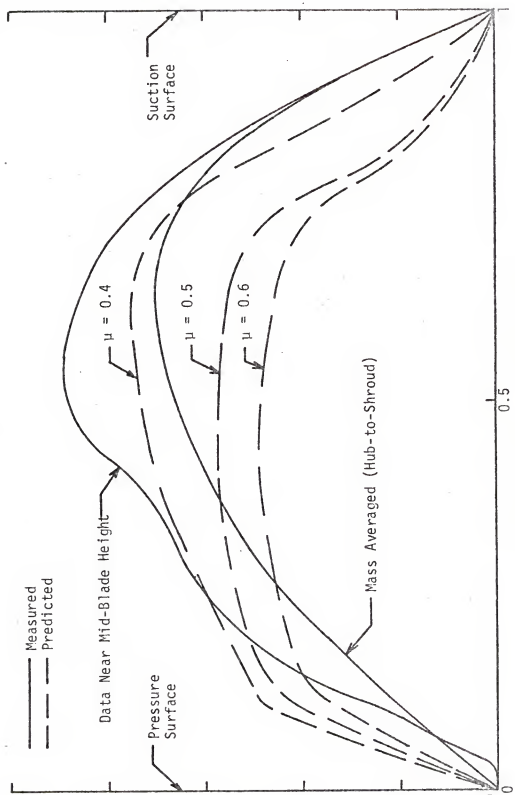

Fig. 6.10. Comparison of Measured and Predicted Deviation Angle for Radial Impeller with Backward-Swept Blades

The design specifications for this impeller were obtained from reference [73], and are given in Table II.

Table II. Design Specifications for Radial-Bladed Pump Impeller.

Rotational Speed	3000 rpm
Number of Blades	28*
Blade Thickness	0.062 in.
Design Mass Flow	70 lb_m/sec
Design Efficiency	0.80
Incidence Angle	2 deg.
Inlet Tip Radius	2.112 in.
Inlet Radius Ratio	0.65
Discharge Radius	3.718 in.
Discharge Depth	0.191 in.
Axial Length	1.1 in.

*includes splitter blades

Figure 6.11 shows a meridional plane view of the impeller, and also gives the streamwise calculation stations used in the analysis. Besides the seven stations within the impeller passages, four more were required in the region shown upstream of the leading edge, and four were located

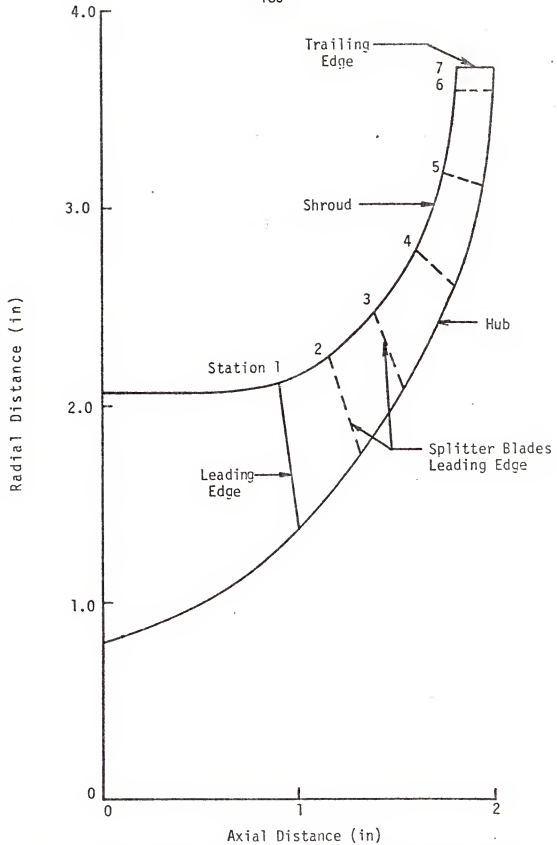

Fig. 6.11. Meridional Plane View of Radial-Bladed Pump Impeller Showing Calculation Station Locations

downstream of the trailing edge in the vaneless diffuser. The actual impeller described in reference [73] employed two sets of splitter blades (blades which do not extend over the complete passage length) which started at stations 2 and 3 of Fig. 6.11. Since the present analysis is not equipped to handle this situation, the impeller is considered as having 28 full blades. But to ensure the same blade blockage upstream of the splitter leading edges, the splitter blade thicknesses are set equal to zero at these locations.

Figure 6.12 shows the influence of viscous effects on blade surface velocities at design speed and a flow rate which is about 4% greater than design. The velocities presented for the combined flow analysis represent the inviscid core flow velocities at the outer edge of the boundary layer. As one would expect, the core is accelerated continuously from the inlet to the discharge as a result of the boundary layer displacement effect.

The boundary layer development for these same operating conditions is shown in Fig. 6.13. Note that the principal contribution to the acceleration of the core flow comes from the suction surface boundary layer growth in the radial part of the impeller, i.e., downstream of station 4 in Fig. 6.11. The blade surface boundary layers were computed assuming fully turbulent flow. The pressure surface

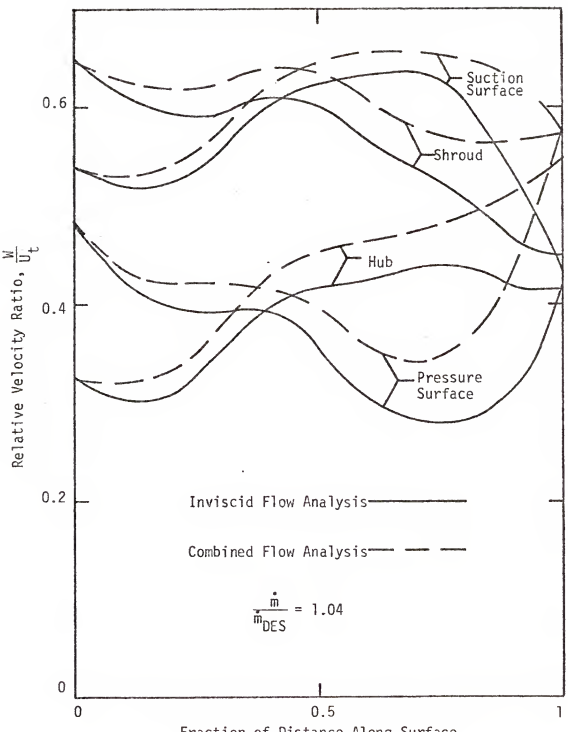

Fig. 6.12. Predicted Blade Surface Velocities for Radial-Bladed Pump Impeller

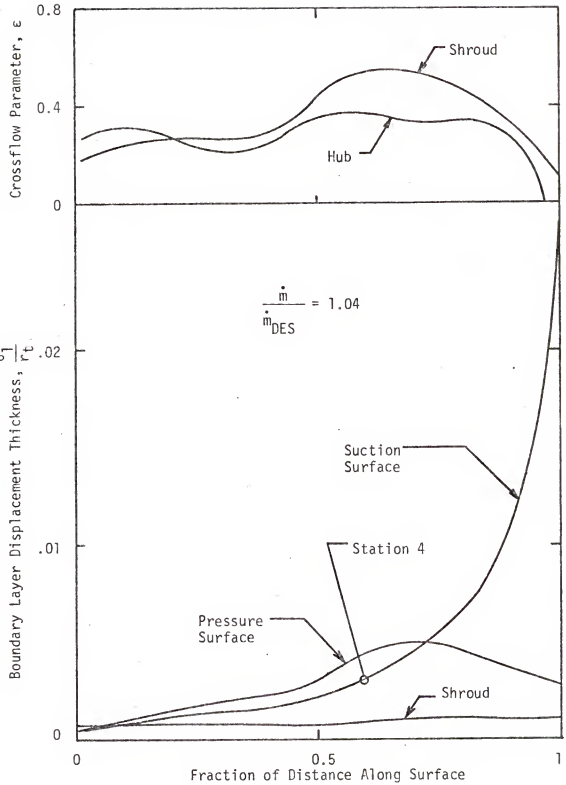

Fig. 6.13. Predicted Boundary Layer Development for Radial-Bladed Pump Impeller

boundary layer grows more rapidly than the suction surface layer in the primarily axial portion of the impeller for two reasons. First, there is a larger adverse pressure gradient on the pressure side of the passage (see Fig. 6.12), and second, because secondary flows resulting from the action of Coriolis forces are not strong enough to retard the boundary layer development until the radial portion of the impeller. Note that beyond station 4 the pressure surface boundary layer begins to decrease in thickness.

The hub and shroud boundary layer calculations were started at the inlet station upstream of the impeller using the procedures described in Chapter V. Because of the converging passage shape in the inlet region, the flow was accelerated as it approached the impeller blades. This resulted in very thin hub and shroud boundary layers at station 1. Calculations within the impeller passage showed that the shroud boundary layer thickness was essentially constant throughout. This is reasonable since the streamwise pressure gradient was mild, and secondary flow acts to inhibit its growth. The predicted hub boundary layer, which is not shown, was even thinner than the shroud boundary layer due to a favorable streamwise pressure gradient and the effects of crossflow.

The distribution of the crossflow parameter ε (tangent of the limiting wall streamline angle) is also shown

in Fig. 6.13. The values presented were calculated for conditions along the hub and shroud streamlines outside the boundary layer and nearest to the suction surface corners. Note that the crossflow parameter is largest in the radial portion of the impeller, but diminishes rapidly near the exit as the flow begins to deviate from the blade direction.

Finally, Fig. 6.14 shows the mean blade-to-blade and hub-to-shroud velocity profiles computed for the radial-bladed impeller at two different flows. The hub-to-shroud velocity profiles are nearly flat except for the boundary layers. This agrees qualitatively with the data reported in reference [73], where circumferentially averaged measurements were taken in the vaneless diffuser (1/2 inch from the impeller tip) at these same flow rates.

In summary, the combined viscous/inviscid flow model provides a reasonable approximation to the actual flow in a centrifugal impeller. The predictions presented in this chapter show clearly the influence of viscosity on the passage velocity distributions. Agreement between predicted and measured flow is encouraging; however further verification is needed for more complex geometries.

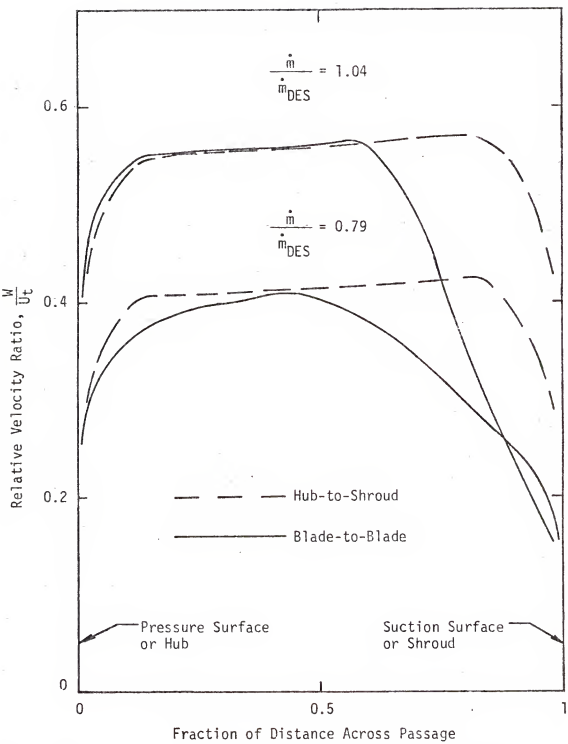

Fig. 6.14. Predicted Exit Velocity Profiles for Radial-Bladed Pump Impeller

CHAPTER VII
CONCLUSIONS

A method of analysis has been developed for three-dimensional viscous flow in centrifugal impellers. Predicted flow characteristics show reasonable agreement with experimental data for a rotating rectangular diffuser and a radial-flow impeller with swept-back blades. Also, predicted discharge velocity profiles for a three-dimensional radial-bladed centrifugal pump are similar to experimentally observed profiles, i.e., a large region of low energy fluid adjacent to the suction surface. On the whole, the results presented here for the combined viscous/inviscid flow analysis offer encouragement for further applications of three-dimensional boundary layer theory to predict the real flow in centrifugal impellers.

APPENDICES

APPENDIX A

CUBIC SPLINE CURVES

In the streamline curvature method of analysis, it is necessary to compute accurate first and second derivatives from function values at a set of discrete points which are generally not equally spaced. There are several possible approaches to fitting a curve through these points, e.g., an n^{th} degree polynomial through n+1 points, or a least squares approximation. However, the polynomial fit often results in an oscillatory behavior while the least squares fit does not pass through all of the points. An effective means of generating a smooth curve passing through each point is the cubic spline fit, a name derived from its analogy with the draftsman's spline (a thin strip of flexible material used to draw a smooth curve through a collection of points). The spline fit employs a different cubic between each pair of adjacent points with matching first and second derivatives at the junctions.

A complete discussion of spline theory and a simple algorithm for applying it are given in the book by Ahlberg et al. [56]. Briefly, for n+1 points (x_j, y_j) there are

n-1 linear equations in the n+1 unknowns $y''(x_j)$. A complete set of n+1 simultaneous equations is obtained by specifying end conditions such as slopes; or, if the slopes can not be estimated accurately, a relation between the second derivatives at the end point and the adjacent point of the form

$$y''(x_n) = k\, y''(x_{n-1}) \quad (0 \leq k \leq 1) .$$

In matrix notation, the defining equations may be written as

$$\begin{bmatrix} 2 & \lambda_0 & 0 & \cdots & 0 & 0 & 0 \\ \mu_1 & 2 & \lambda_1 & \cdots & 0 & 0 & 0 \\ 0 & \mu_2 & 2 & \cdots & 0 & 0 & 0 \\ \vdots & \vdots & \vdots & \cdots & \vdots & \vdots & \vdots \\ 0 & 0 & 0 & \cdots & 2 & \lambda_{n-2} & 0 \\ 0 & 0 & 0 & \cdots & \mu_{n-1} & 2 & \lambda_{n-1} \\ 0 & 0 & 0 & \cdots & 0 & \mu_n & 2 \end{bmatrix} \begin{bmatrix} y''_0 \\ y''_1 \\ y''_2 \\ \vdots \\ y''_{n-2} \\ y''_{n-1} \\ y''_n \end{bmatrix} = \begin{bmatrix} d_0 \\ d_1 \\ d_2 \\ \vdots \\ d_{n-2} \\ d_{n-1} \\ d_n \end{bmatrix} \qquad (A.1)$$

where for $(j = 1,2,\ldots n-1)$ we have $\mu_j = (x_j - x_{j-1})/(x_{j+1} - x_{j-1})$, $\lambda_j = 1 - \mu_j$, and

$$d_j = 6\left\{\frac{[(y_{j+1}-y_j)/(x_{j+1}-x_j)] - [(y_j-y_{j-1})/(x_j-x_{j-1})]}{x_{j+1} - x_{j-1}}\right\}$$

Values of μ, λ, and d at the end points (j=0,n) are determined by the choice of end conditions. The coefficient matrix of (A.1) is tridiagonal, hence it is easily solved by Gauss elimination. Moreover, because it has a dominant main diagonal for the end conditions of interest, this matrix is always nonsingular with a unique solution.

Once the second derivatives are determined at each x_j, it is a simple matter to perform interpolation, numerical differentiation, or integration. As pointed out in reference [56], the method is particularly suited to applications where first derivatives are required. Provided the data points are not scattered, very smooth slopes are obtained because of the minimum curvature property of spline curves. This property results from a minimizing of the integral

$$\int_{x_0}^{x_n} |y''(x)|^2 dx$$

which is a good approximation to the square of the curvature of y(x) when the slope is not too large. Good approximations for second derivatives are obtained when the function is first spline-fit to determine the slopes, then a second

curve is fit through the slopes to find the second derivatives. This technique is used to compute meridional streamline curvature $\frac{D\alpha}{Dm}$, where α is the streamline slope in the r-z plane.

APPENDIX B

THE MOSES METHOD FOR TWO-DIMENSIONAL TURBULENT BOUNDARY LAYERS

A two-dimensional incompressible turbulent boundary layer prediction technique developed by Moses [63] was used as the basic building block in the formulation and numerical solution of the streamwise momentum integral equations for the impeller hub, shroud, and blade surfaces. This method was rated among the best at the 1968 Stanford Conference on Turbulent Boundary Layers [74]. Equally important, it requires considerably less computation time than the more sophisticated differential methods with only a slight sacrifice in accuracy.

The method employs a two-parameter family of velocity profiles in terms of the dependent variables R_δ and A, where R_δ is the boundary layer thickness Reynolds number and A is a wall shear stress parameter defined by

$$A = \frac{1}{0.41} \sqrt{\frac{C_f}{2}}$$

Using the logarithmic wall law combined with a polynomial approximation to the wake function [75], and an empirical

relation for the sublayer, Moses integrates the boundary layer equations normal to the wall out to some fraction of the boundary layer thickness $\eta_1 = y_1/\delta$ to yield

$$\frac{u}{U}\frac{d}{dx}\left(R_\delta \int_0^{\eta_1} \frac{u}{U} d\eta\right) - \frac{1}{U}\frac{d}{dx}\left(UR_\delta \int_0^{\eta_1} \frac{u^2}{U^2} d\eta\right) = \frac{\tau(0)-\tau(\eta_1)}{\mu U} - \frac{\eta_1 R_\delta}{U}\frac{dU}{dx} \tag{B.1}$$

With values $\eta_1 = 0.3, 1.0$, two separate equations are obtained.

The turbulent shear stress at $\eta_1 = 0.3$ is approximated using an eddy viscosity hypothesis based on constant pressure data, or

$$(\tau)_{\eta=0.3} = \rho U\theta\left(0.0225 + \frac{125}{R_\delta}\right)\frac{\partial u}{\partial y} . \tag{B.2}$$

Then, the velocity profile relations and equation (B.2) (for $\eta_1 = 0.3$) are introduced into equation (B.1) which is evaluated for each boundary layer strip. The result is a pair of ordinary differential equations of the form

$$F_{i1}\frac{dA}{dx} + F_{i2}\frac{dR_\delta}{dx} = G_i , \quad i = 1,2 . \tag{B.3}$$

Given initial values of A and R_δ and the freestream velocity distribution U(x), the two simultaneous equations

may be solved by numerical integration. The boundary layer thickness parameters δ^* and Θ are given in terms of A and R_δ, and may be computed at each step of the calculation.

APPENDIX C

GEODESIC CURVATURES FOR A SURFACE OF REVOLUTION

The geodesic curvature K_{21} describes the convergence or divergence of adjacent streamlines on the surface $x_3=0$ for orthogonal streamline coordinates with x_1 as the streamwise direction. From equation (4.8), we have

$$K_{21} = -\frac{1}{h_1 h_2}\frac{\partial h_2}{\partial x_1} = -\frac{1}{h_2}\frac{\partial h_2}{\partial s} \qquad (C.1)$$

where h_1 and h_2 are the metric coefficients which are functions of the coordinates (x_1, x_2, x_3) and s is the actual distance measured along a streamline. In the analysis which follows, an explicit relation is derived for K_{21} in terms of the impeller hub or shroud surface geometry and the inviscid flow field.

Since the hub and shroud are surfaces of revolution, and the inviscid flow is determined using cylindrical coordinates, the most suitable system for expressing K_{21} is meridional coordinates: m, θ and y. Here m is measured along the surface in the r-z plane, θ is the circumferential

angle, and y is normal to the surface. The surface projections of the inviscid streamlines may be considered as functions of m and x_2: $\theta = \theta(m,x_2)$, where x_2 is constant for a particular streamline. If we require that θ have continuous first and second derivatives on the surface, then

$$\frac{\partial^2\theta}{\partial m \partial x_2} = \frac{\partial^2\theta}{\partial x_2 \partial m} \quad . \tag{C.2}$$

Denoting the first derivatives by

$$M = \left(\frac{\partial\theta}{\partial m}\right)_{x_2} \qquad \text{and} \qquad N = \left(\frac{\partial\theta}{\partial x_2}\right)_m \tag{C.3}$$

where the subscripts indicate the variable held constant, equation (C.2) may be written as

$$\left(\frac{\partial M}{\partial x_2}\right)_m = \left(\frac{\partial N}{\partial m}\right)_{x_2} \quad . \tag{C.4}$$

The inviscid flow is known as a function of m and θ, thus it is desirable to express $\left(\frac{\partial M}{\partial x_2}\right)_m$ in terms of these variables. Using the chain rule we obtain

$$\left(\frac{\partial M}{\partial x_2}\right)_m = \left(\frac{\partial M}{\partial \theta}\right)_m \left(\frac{\partial \theta}{\partial x_2}\right)_m \quad . \tag{C.5}$$

Then equation (C.4) becomes

$$\left(\frac{\partial N}{\partial m}\right)_{x_2} = \left(\frac{\partial M}{\partial \theta}\right)_m \left(\frac{\partial \theta}{\partial x_2}\right)_m = N\left(\frac{\partial M}{\partial \theta}\right)_m \quad . \tag{C.6}$$

Next, we must determine M and N for an arbitrary three-dimensional flow over a surface of revolution.

The vector differential distance between any two points on the surface is given by

$$d\vec{R} = \hat{e}_m dm + \hat{e}_\theta r d\theta \tag{C.7}$$

in terms of meridional coordinates, and also by

$$d\vec{R} = \hat{e}_1 h_1 dx_1 + \hat{e}_2 h_2 dx_2 \tag{C.8}$$

for streamline coordinates. The scalar product of $\hat{e}_\theta$ with equations (C.7) and (C.8) yields

$$r d\theta = (\hat{e}_\theta \cdot \hat{e}_1) h_1 dx_1 + (\hat{e}_\theta \cdot \hat{e}_2) r d\theta$$

and the scalar product of $\hat{e}_1$ with equations (C.7) and (C.8) results in

$$h_1 dx_1 = (\hat{e}_1 \cdot \hat{e}_m) dm + (\hat{e}_1 \cdot \hat{e}_\theta) r d\theta \quad .$$

Eliminating $h_1 dx_1$ between the equations we obtain

$$d\theta = \frac{(\hat{e}_\theta \cdot \hat{e}_1)(\hat{e}_1 \cdot \hat{e}_m)dm + (\hat{e}_\theta \cdot \hat{e}_2)h_2 dx}{r[1 - (\hat{e}_\theta \cdot \hat{e}_1)^2]} \quad . \tag{C.9}$$

But, since $\theta = \theta(m, x_2)$ we may write

$$d\theta = \left(\frac{\partial \theta}{\partial m}\right)_{x_2} dm + \left(\frac{\partial \theta}{\partial x_2}\right)_m dx_2$$

which when compared with equation (C.9) yields

$$M = \left(\frac{\partial \theta}{\partial m}\right)_{x_2} = \frac{(\hat{e}_\theta \cdot \hat{e}_1)(\hat{e}_1 \cdot \hat{e}_m)}{r[1 - (\hat{e}_\theta \cdot e_1)^2]} \tag{C.10}$$

and

$$N = \left(\frac{\partial \theta}{\partial x_2}\right)_m = \frac{(\hat{e}_\theta \cdot \hat{e}_2)h_2}{r[1-(\hat{e}_\theta \cdot \hat{e}_1)^2]} \quad . \tag{C.11}$$

The unit vectors are related to the relative flow angle β as follows:

$$\hat{e}_1 = \hat{e}_m \cos\beta + \hat{e}_\theta \sin\beta$$

and

$$\hat{e}_2 = -\hat{e}_m \sin\beta + \hat{e}_\theta \cos\beta \quad .$$

Substituting these relations into equations (C.10) and (C.11), we obtain

$$M = \frac{\tan\beta}{r} \tag{C.12}$$

and

$$N = \frac{h_2}{r\cos\beta} \quad . \tag{C.13}$$

The partial derivatives in equation (C.6) become

$$\left(\frac{\partial N}{\partial m}\right)_{x_2} = \frac{1}{r\cos\beta}\left[\frac{\partial h_2}{\partial m} - \frac{h_2}{r}\frac{\partial r}{\partial m} + h_2\tan\beta\frac{\partial\beta}{\partial m}\right]$$

and

$$\left(\frac{\partial\theta}{\partial M}\right)_{x_2} = \frac{1}{r\cos^2\beta}\left(\frac{\partial\beta}{\partial\theta}\right)_m - \frac{\tan\beta}{r^2}\left(\frac{\partial r}{\partial\theta}\right)_m \quad .$$

But, since the surface is axisymmetric, $\left(\frac{\partial r}{\partial\theta}\right)_m = 0$. Then, using the above results, equation (C.6) may be written as

$$\frac{1}{h_2}\left(\frac{\partial h_2}{\partial m}\right)_{x_2} = \frac{1}{r}\left(\frac{\partial r}{\partial m}\right)_{x_2} - \tan\beta\left(\frac{\partial\beta}{\partial m}\right)_{x_2} + \frac{1}{r\cos^2\beta}\left(\frac{\partial\beta}{\partial\theta}\right)_m \quad .$$

Noting that along a streamline (x_2=constant)

$$\frac{\partial(\ )}{\partial s} = \frac{\partial(\ )}{\partial m}\cos\beta \quad \text{and} \quad \frac{\partial(\ )}{\partial s} = \frac{1}{h_1}\frac{\partial(\ )}{\partial x_1} \ ,$$

we obtain the following expression for the streamline divergence or convergence:

$$K_{21} = -\frac{1}{h_1 h_2}\frac{\partial h_2}{\partial x_1} = -\frac{1}{r}\frac{\partial r}{\partial s} + \tan\beta\frac{\partial \beta}{\partial s} - \frac{1}{r\cos\beta}\frac{\partial \beta}{\partial \theta} \qquad (C.14)$$

Equation (C.14) may be evaluated at any point on the impeller hub or shroud using the local inviscid streamline geometry. For the case of radially outward flow ($s=r$, $\beta=0$) this reduces to the familiar expression for streamline divergence, $K_{21} = -\frac{1}{r}$ with $h_2 = r$.

A similar procedure is employed to derive an expression for streamline curvature, i.e.,

$$K_{12} = -\frac{1}{h_1 h_2}\frac{\partial h_1}{\partial x_2} = -\frac{1}{h_1}\frac{\partial h_1}{\partial n} \qquad (C.15)$$

Briefly, the approach is the same except that $\theta = \theta(m, x_1)$ is the defining relation for the streamline orthogonals along which x_1=constant. This leads to the following definitions:

$$M = \left(\frac{\partial \theta}{\partial m}\right)_{x_1} \qquad \text{and} \qquad N = \left(\frac{\partial \theta}{\partial x_1}\right)_m \qquad (C.16)$$

where

$$\left(\frac{\partial N}{\partial m}\right)_{x_1} = N\left(\frac{\partial M}{\partial \theta}\right)_m \qquad (C.17)$$

After some manipulation we obtain

$$M = \frac{-1}{r\tan\beta} \qquad \text{and} \qquad N = \frac{h_1}{r\sin\beta} \quad . \tag{C.18}$$

Substituting equations (C.18) into equation (C.17) yields

$$\frac{\sin\beta}{h_1}\left(\frac{\partial h_1}{\partial m}\right)_{x_1} - \cos\beta\left(\frac{\partial\beta}{\partial m}\right)_{x_1} - \frac{\sin\beta}{r}\left(\frac{\partial r}{\partial m}\right)_{x_1} = \frac{1}{r\sin\beta}\left(\frac{\partial\beta}{\partial\theta}\right)_m \quad .$$

Noting that

$$\left(\frac{\partial(\ )}{\partial n}\right)_{x_1} = \left(\frac{\partial(\ )}{\partial m}\right)_{x_1}\left(\frac{\partial m}{\partial n}\right)_{x_1} = -\left(\frac{\partial(\ )}{\partial m}\right)_{x_1}\sin\beta$$

and

$$\frac{\partial(\ )}{\partial s} = \frac{1}{r\sin\beta}\frac{\partial(\ )}{\partial\theta} - \frac{1}{\tan\beta}\frac{\partial(\ )}{\partial n}$$

we may write the final expression for streamline curvature in the form

$$K_{12} = -\frac{1}{h_1 h_2}\frac{\partial h_1}{\partial x_2} = \frac{\partial\beta}{\partial s} + \frac{\tan\beta}{r}\frac{\partial r}{\partial s} \quad . \tag{C.19}$$

BIBLIOGRAPHY

1. Wu, C.H., "A General Theory of Three-Dimensional Flow in Subsonic and Supersonic Turbomachines of Axial, Radial, and Mixed Flow Type," NACA TN 2604, 1952.

2. Hamrick J.T., Ginsburg, A., and Osborn, W.M., "Method of Analysis for Compressible Flow Through Mixed-Flow Centrifugal Impellers of Arbitrary Design," NACA Report 1082, 1952.

3. Smith, L.H., "The Radial Equilibrium Equation of Turbomachinery," Trans. ASME, Journal of Engineering for Power, Vol. 88, No. 1, Jan. 1966, pp. 1-12.

4. Novak, R.A., "Streamline Curvature Computing Procedures for Fluid Flow Problems," Trans. ASME, Journal of Engineering for Power, Vol. 89, No. 4, Oct. 1967, pp. 478-490.

5. Stockman, N.O., and Kramer, J.L., "Method for Design of Pump Impellers Using a High-Speed Digital Computer," NASA TN D-1562, 1963.

6. Wood, M.D., and Marlow, A.V., "The Use of Numerical Methods for the Investigation of Flow in Water Pump Impellers," Proc. Instn. Mech. Engrs., Vol. 181 (Pt. 1), 1966-67, p. 725.

7. Katsanis, T., "Use of Arbitrary Quasi-Orthogonals for Calculating Flow Distribution in the Meridional Plane of a Turbomachine," NASA TN D-2546, 1964.

8. Vanco, M.R., "Fortran Program for Calculating Velocities in the Meridional Plane of a Turbomachine 1: Centrifugal Compressor," NASA-TN-D-6701, 1972.

9. Marsh, H., "Digital Computer Program for the Through-Flow Fluid Mechanics in an Arbitrary Turbomachine Using a Matrix Method," ARC R&M No. 3509, 1968.

10. Kramer, J.J., "Analysis of Incompressible, Nonviscous Blade-to-Blade Flow in Rotating Blade Rows," Trans. ASME, Vol. 80, No. 1, Jan. 1958, pp. 263-275.

11. Katsanis, T., "Use of Arbitrary Quasi-Orthogonals for Calculating Flow Distribution on a Blade-to-Blade Surface in a Turbomachine," NASA TN D-2809, 1965.

12. Katsanis, T., "Quasi-Three-Dimensional Calculation of Velocities in Turbomachine Blade Rows," NASA TM-X-67959, 1972.

13. Senoo, Y., and Nakase, Y., "An Analysis of Flow Through a Mixed Flow Impeller," Journal of Engineering for Power, Trans. ASME, Vol. 94, No. 1, Jan. 1972, pp. 43-50.

14. Senoo, Y, and Nakase, Y., "A Blade Theory of an Impeller with an Arbitrary Surface of Revolution," Trans. ASME, Journal of Engineering for Power, Vol. 93, No. 4, Oct. 1971, pp. 454-460.

15. Nash, J., "The Calculation of Three-Dimensional Turbulent Boundary Layers in Incompressible Flow," Journal of Fluid Mechanics, Vol. 37, 1969, pp. 625-642.

16. Bradshaw, P., "Calculation of Three-Dimensional Turbulent Boundary Layers," Journal of Fluid Mechanics, Vol. 46, 1971, pp. 417-445.

17. Cooke, J.C., and Hall, M.G., "Boundary Layers in Three Dimensions," Progress in the Aeronautical Sciences, Vol. 2, Pergamon Press, 1962.

18. Mager, A., "Generalization of Boundary Layer Momentum Integral Equations to Three-Dimensional Flow Including Those of Rotating Systems," NACA Report 1067, 1952.

19. Cumpsty, N.A., and Head, M.R., "The Calculation of Three-Dimensional Turbulent Boundary Layers Part I: Flow over the Rear of an Infinite Swept Wing," The Aeronautical Quarterly, Vol. 18, Feb. 1967, pp. 55-84.

20. Cham, T-S, and Head, M.R., "The Turbulent Boundary Layer on a Rotating Nose-Body," The Aeronautical Quarterly, Vol. 22, Nov. 1971, pp. 389-402.

21. Horlock, J.H., "Boundary Layer Problems in Axial Turbomachines," Flow Research in Blading, Dzung, L.S., ed., Elsevier Publishing Company, Amsterdam, 1970, pp. 322-357.

22. Dring, R.P., "A Momentum Integral Analysis of the Three Dimensional Turbine End Wall Boundary Layer," Trans. ASME, Journal of Engineering for Power, Vol. 93, No. 4, Oct. 1971, pp. 386-396.

23. Lakshminarayana, B., Jabbari, A., and Yamaoka, H., "Turbulent Boundary Layer on a Rotating Helical Blade," Journal of Fluid Mechanics, Vol. 51, 1972, pp. 545-569.

24. Johnston, J.P., "On the Three-Dimensional Turbulent Boundary Layer Generated by Secondary Flow," Trans. ASME, Journal of Basic Engineering, Vol. 82, No. 3, Sept. 1960, pp. 233-246.

25. Shanebrook, J.R., and Hatch, D.E., "A Family of Hodograph Models for the Cross Flow Velocity Component of Three-Dimensional Turbulent Boundary Layers," Trans. ASME, Journal of Basic Engineering, Vol. 94, No. 3, June 1972, pp. 321-332.

26. Stahler, Alfred E., "The Slip Factor of a Radial Bladed Centrifugal Compressor," Trans. ASME, Journal of Engineering for Power, Vol. 87, No. 2, Apr. 1965, pp. 181-192.

27. Wiesner, F.J., "A Review of Slip Factors for Centrifugal Impellers," Trans. ASME, Journal of Engineering for Power, Vol. 89, No. 4, Oct. 1967, pp. 558-566.

28. Dean, R.C., "On the Unresolved Fluid Dynamics of the Centrifugal Compressor," Advanced Centrifugal Compressors, ASME, New York, 1971.

29. Johnsen, I.A., and Ginsburg, A., "Some NACA Research on Centrifugal Compressors," Trans. ASME, Vol. 75, July 1953, pp. 805-817.

30. Hamrick, J.R., Mizisin, J., and Michel, D.J., "Study of the Three-Dimensional Internal Flow Distribution Based on Measurements in a 48-Inch Radial-Inlet Centrifugal Impeller," NACA TN 3101, Feb. 1954.

31. Acosta, A.J., and Bowerman, R.D., "An Experimental Study of Centrifugal Pump Impellers," Trans. ASME, Vol. 79, No. 8, 1957, pp. 1821-1839.

32. Ash, J.E., "Measurements of Relative Flow Distributions in Mixed Flow Impellers," ASME Paper No. 56-A-205, Nov. 1956.

33. Fujie, K., "Three-Dimensional Investigation of Flow in Centrifugal Impeller with Straight-Radial Blades," Bulletin of JSME, Vol. 1, No. 1, 1958, pp. 42-49.

34. Fujie, K., "Study of Three-Dimensional Internal Flow in Impellers of Centrifugal Blowers with Straight-Radial Blades and Logarithmic-Spiral Blades in Radial Part Only," Bulletin of JSME, Vol. 1, No. 3, 1958, pp. 275-282.

35. Fujie, K., "A Study on the Flow in a Centrifugal Impeller with Passages of Circular-Arc in Meridional Plane," Bulletin of JSME, Vol. 4, No. 13, 1961, pp. 94-101.

36. Lohmann, R.P., "An Investigation of the Influence of Boundary Layers on the Performance of Centrifugal Compressor Impellers," Trans. ASME, Journal of Basic Engineering, Vol. 88, No. 1, Mar. 1966, pp. 71-81.

37. Senoo, Y., Yamaguchi, M., and Nishi, M., "A Photographic Study of the Three-Dimensional Flow in a Radial Compressor," Trans. ASME, Journal of Engineering for Power, Vol. 90, No. 3, July 1968, pp. 237-244.

38. Lennemann, E., "Secondary Flows in Rotating Passages," Ph.D. Thesis, University of Waterloo, Aug. 1969.

39. Howard, J.G.H., and Lennemann, E., "Measured and Predicted Secondary Flows in a Centrifugal Impeller," Trans. ASME, Journal of Engineering for Power, Vol. 93, No. 1, Jan. 1971, pp. 126-132.

40. Lennemann, E., and Howard, J.H.G., "Unsteady Flow Phenomena in Rotating Centrifugal Impeller Passages," Trans. ASME, Journal of Engineering for Power, Vol. 92, No. 1, Jan. 1970, pp. 65-72.

41. McDonald, G.B., Lennemann, E., and Howard, J.G.H., "Measured and Predicted Flow Near the Exit of a Radial Flow Impeller," Trans. ASME, Journal of Engineering for Power, Vol. 93, No. 4, Oct. 1971, pp. 441-446.

42. Senoo, Y., Maruyama, S., Koizumi, T., and Nakase, Y., "Viscous Effects on Slip Factors of Centrifugal Blowers," ASME Paper 73-GT-56, 1973.

43. Hill, P.G., and Moon, I.M., "Effects of Coriolis on the Turbulent Boundary Layer in Rotating Fluid Machines," Gas Turbine Laboratory Report No. 69, M.I.T., June 1962.

44. Moon, I.M., "Effects of Coriolis Force on the Turbulent Boundary Layers in Rotating Fluid Machines," Gas Turbine Laboratory Report No. 74, M.I.T., June 1964.

45. Moore, J., "Effects of Coriolis on Turbulent Flow in Rotating Rectangular Channels," Gas Turbine Laboratory Report No. 89, M.I.T., Jan. 1967.

46. Moore, J., "The Development of Turbulent Boundary Layers in Centrifugal Machines," Gas Turbine Laboratory Report No. 99, M.I.T., June 1969.

47. Moore, J., "A Wake and an Eddy in a Rotating, Radial-Flow Passage, Part 1: Experimental Observations," Trans. ASME, Journal of Engineering for Power, Vol. 95, No. 3, July 1973, pp. 205-212.

48. Moore, J., "A Wake and an Eddy in a Rotating, Radial-Flow Passage, Part 2: Flow Model," Trans. ASME, Journal of Engineering for Power, Vol. 95, No. 3, July 1973, pp. 213-219.

49. Wagner, R.E., and Velkoff, H.R., "Measurements of Secondary Flows in a Rotating Duct," Trans. ASME, Journal of Engineering for Power, Vol. 94, No. 4, Oct. 1972, pp. 261-270.

50. Fowler, H.S., "The Distribution and Stability of Flow in a Rotating Channel," Trans. ASME, Journal of Engineering for Power, Vol. 90, No. 3, July 1968, pp. 229-236.

51. Litvai, E., "Prediction of Velocity Profiles for Turbulent Boundary Layers on the Blading of Radial Impellers," Proceedings, Conf. on Fluid Machinery, 4th, Budapest, Hungary, Sept. 1972, pp. 771-782.

52. Johnston, J.P., "The Effects of Rotation on Boundary Layers in Turbomachine Rotors," Stanford Univ., Mech. Eng. Dept., Report MD-24, 1970.

53. Johnston, J.P., "The Suppression of Shear Layer Turbulence in Rotating Systems," Trans. ASME, Journal of Fluids Engineering, Vol. 95, No. 3, June 1973, pp. 229-236.

54. Bradshaw, P., "Effects of Streamline Curvature on Turbulent Flow," AGARD-AG-169, NATO, Aug. 1973.

55. Vavra, M.H., Aerothermodynamics and Flow in Turbomachines, Wiley and Sons, New York, 1960.

56. Ahlberg, J.H., Nilson, E.N., and Walsh, J.H., The Theory of Splines and Their Application, Academic Press, New York, 1967.

57. Rouse, H., ed., Advanced Mechanics of Fluids, Wiley & Sons, New York, 1959, pp. 411-412.

58. Mager, A., "Three Dimensional Laminar Boundary Layers," Theory of Laminar Flows, Moore, F.K., ed., High Speed Aerodynamics and Jet Propulsion, Vol. IV, Princeton Univ. Press, 1964, p. 286.

59. Halleen, R.M., Johnston, J.P., and Reynolds, W.C., "The Laminar Boundary Layer on a Rotating Circular Arc Blade," Trans. ASME, Journal of Basic Engineering, Vol. 88, No. 2, Mar. 1966, p. 111.

60. Cham, T-S, and Head, M.R., "Turbulent Boundary-Layer Flow on a Rotating Disc," Journal of Fluid Mechanics, Vol. 37, 1969, p. 129.

61. Cumpsty, N., "A Critical Examination of the Use of a Two-Dimensional Turbulent Profile Family to Represent Three-Dimensional Boundary Layers," ARC Current Paper No. 1068, 1970.

62. Prahlad, T.S., "Mean Velocity Profiles in Three-Dimensional Incompressible Turbulent Boundary Layers," AIAA Journal, Vol. 11, No. 3, Mar. 1973, pp. 359-365.

63. Moses, H.L., "A Strip-Integral Method for Predicting the Behavior of Turbulent Boundary Layers," Symposium on Turbulent Boundary Layers, Stanford Univ., Aug. 1968.

64. Balje, I.O., "Loss and Flow Path Studies on Centrifugal Compressors," ASME Paper 70-GT-12-a, May 1970.

65. Selezney, K.P., and Shkarbul, S.N., "Study of a Viscous Flow in Rotating Centrifugal Impellers," Proceedings, Conf. on Fluid Machinery, 4th, Budapest, Hungary, Sept. 1972, pp. 1215-1227.

66. Parsons, D.J., and Hill, P.G., "Effects of Curvature on Two-Dimensional Diffuser Flow," Trans. ASME, Journal of Fluids Engineering, Vol. 95, No. 4, Sept. 1973, pp. 349-360.

67. Thwaites, B., "Approximate Calculation of the Laminar Boundary Layer," Aeronautical Quarterly, Vol. 1, 1948, pp. 245-280.

68. Smith, A.M.O., "Transition, Pressure Gradient, and Stability Theory," Proceedings of the 9th Intern. Congress of Applied Mechanics, Brussels, Vol. 7, 1957, pp. 234-244.

69. Coles, D.E., "Measurements of the Boundary Layer on a Smooth Flat Plate in Supersonic Flow," Jet Propulsion Laboratory Report No. 20-69, 1953.

70. Dean, R.C., and Senoo, Y., "Rotating Wakes in Vaneless Diffusers," Trans. ASME, Journal of Basic Engineering, Vol. 82, No. 3, Sept. 1960, pp. 563-574.

71. Johnston, J.P., and Dean, R.C., "Losses in Vaneless Diffusers of Centrifugal Compressors and Pumps," Trans. ASME, Journal of Engineering for Power, Vol. 88, No. 1, Jan. 1966, pp. 49-62.

72. Mellor, G.L., and Wood, G.M., "An Axial Compressor End-Wall Boundary-Layer Theory," Trans. ASME, Journal of Basic Engineering, Vol. 93, No. 3, June 1971, pp. 300-316.

73. Miller, M.J., and Soltis, R.F., "Detailed Performance of a Radial-Bladed Centrifugal Pump Impeller in Water," NASA TN D-4613, July 1968.

74. Kline, S.J., Sovran, G., Morkovin, M.V., and Cockrell, D.J. (editors), "Computation of Turbulent Boundary Layers-1968," Stanford Conference Proceedings, Vol. I, Thermoscience Division, Dept. of Mech. Eng., Stanford Univ., Aug. 1968.

75. Coles, D.E., "The Law of the Wake in the Turbulent Boundary Layer," Journal of Fluid Mechanics, Vol. 1, 1956, pp. 191-226.

BIOGRAPHICAL SKETCH

Frank Warren Lincoln was born March 23, 1943 in Willimantic, Connecticut. He is married to the former Ann Joyce Casey, and has two children, Lori and Eric.

I certify that I have read this study and that in my opinion it conforms to acceptable standards of scholarly presentation and is fully adquate, in scope and quality, as a dissertation for the degree of Doctor of Philosophy.

R.B. Gaither, Chairman
Professor of Mechanical
Engineering

I certify that I have read this study and that in my opinion it conforms to acceptable standards of scholarly presentation and is fully adequate, in scope and quality, as a dissertation for the degree of Doctor of Philosophy.

V.P. Roan, Co-Chairman
Professor of Mechanical
Engineering

I certify that I have read this study and that in my opinion it conforms to acceptable standards of scholarly presentation and is fully adequate, in scope and quality, as a dissertation for the degree of Doctor of Philosophy.

C.C. Oliver
Professor of Mechanical
Engineering

I certify that I have read this study and that in my opinion it conforms to acceptable standards of scholarly presentation and is fully adequate, in scope and quality, as a dissertation for the degree of Doctor of Philosophy.

C.K. Hsieh
Associate Professor of
Mechanical Engineering

I certify that I have read this study and that in my opinion it conforms to acceptable standards of scholarly presentation and is fully adequate, in scope and quality, as a dissertation for the degree of Doctor of Philosophy.

J.F. Mahoney
Associate Professor of
Industrial and Systems
Engineering

This dissertation was submitted to the Dean of the College of Engineering and to the Graduate Council, and was accepted as a partial fulfillment of the requirements for the degree of Doctor of Philosophy.

June, 1975

Dean, College of Engineering

Dean, Graduate School